Nanofinishing of Freeform Surface using Magnetic Field Assisted Finishing (MFAF) Process

A thesis submitted
in partial fulfillment of the requirements
for the degree of

Doctor of Philosophy

By

Anwesa Barman
Roll No.-126103024

Department of Mechanical Engineering

Indian Institute of Technology Guwahati

Guwahati, India

May 2018

Department of Mechanical Engineering
Indian Institute of Technology Guwahati
Guwahati-781039
INDIA

CERTIFICATE

It is certified that the work contained in the thesis entitled "**Nanofinishing of Freeform Surface using Magnetic Field Assisted Finishing (MFAF) Process**", submitted by **Anwesa Barman**, Roll No. 126103024 to the Indian Institute of Technology Guwahati for the degree of Doctor of Philosophy has been carried out under my supervision in the Department of Mechanical Engineering, Indian Institute of Technology Guwahati. This work has not been submitted elsewhere for the award of any other degree or diploma.

Dr. Manas Das

Date: Department of Mechanical Engineering

Indian Institute of Technology Guwahati

Guwahati-781039, Assam, India

Declaration

I declare that this written submission represents my ideas in my own words and where others' ideas or words have been included, I have adequately cited and referenced the original sources. I also declare that I have adhered to all principles of academic honesty and integrity and have not misrepresented or fabricated or falsified any idea/data/fact/source in my submission. I understand that any violation of the above will be cause for disciplinary action by the Institute and can also evoke penal action from the sources which have thus not been properly cited or from whom proper permission has not been taken when needed.

Date:

Anwesa Barman
Roll No. 126103024

Dedicated to

My family

ACKNOWLEDGEMENT

I would like to take this opportunity to pay my deep sense of respect and sincere gratitude to my Supervisor, Dr. Manas Das, Department of Mechanical Engineering of Indian Institute of Technology Guwahati, Assam-781039 for his invaluable advice, resourceful guidance, inspiring instructions, active supervision and constant encouragement without which it would not have been possible for me to reach to this point.

I also wish to thank to all my DC committee members, Dr. S. Senthilvelan, Dr. S. N. Joshi and Dr. T. Banerjee for their guidance, moral support and encouragement for my ideas in the subject as well as other areas of innovations. I must not miss the opportunity to thank all the Professors of Mechanical Engineering Department, Indian Institute of Technology Guwahati, whose motivation and timely help molded me in all possible forms.

I would also like to thank Mr. Jiten Basumatary for his support in carrying out my work in advanced manufacturing lab. I am very much thankful to workshop superintendent Mr. N. K. Das and workshop technicians Mr. Mrinal Sarma, Mr. Dipak Kr. Deka, Mr. Upen Gohain and Mr. Dhaneswar Khaklary for their help to fabricate my experimental setup and workpiece. I would like to acknowledge Central instrument facility (CIF) of IIT Guwahati for kind assistance to carry out my research work.

I thankfully acknowledge Department of Science and Technology (DST), New Delhi, India for their financial support for project No. SB/EMEQ-165/2013 entitled “Nanofinishing of Freeform Surfaces using Magnetorheological Fluid based Finishing (MRFF) process”.

Last, but not least, I am deeply indebted to my parents for the sacrifices they have borne to ensure the fulfillment of my dreams. I would like to thank my family for their support and motivation during my PhD.

The time I spent with all my friends at IIT Guwahati, Chandan Kumar, Anupam Alok, Kelli Durgaprasad, who made my life enjoyable and memorable on the campus. I would also like to thank Hrishikesh, Chunaram, Aman, Shashi, Pritam, Amit and Shafique for their involvement in my work.

ANWESA BARMAN

Abstract

Now-a-days freeform surfaces are frequently used in different industries due to its usefullness. Finishing of freeform surface is a challenging and a complex task. In medical industry, surface of femoral component of a knee joint implant is fabricated freeform shape to increase the resemblence between actual human knee movement and the artificial one. Magntic field assisted finishing (MFAF) process is used to counteract the problems faced during finishing of femoral knee implant and to provide required uniform surface roughness and charaterstics. A novel MFAF polishing tool is designed and developed. As the polishing tool is newly developed, hence its capability to finish Ti alloy for biomedical application is explored in the present study. Also, the competency of the developed tool to finish freeform surface is investigated. This process uses magnetorheological (MR) polishing fluid whose rheological behaviour is controllable by external magnetic field. Two type of MR fluid is synthesized to generate required surface for biomedical application on Ti alloy. The obtained surface roughness after finishing with MR fluid of Type – I is 10 nm and with MR fluid of Type – II is 70 nm. From wettability study, it is found that the surface finished with MR fluid of Type – I is hydrophilic in nature while with MR fluid of Type – II is hydrophobic. The surface characteristics obtained from MR fluid of Type – I is better suited for semi-permanent type of implants or implants which partake in relative motion like femoral part of knee joint and hip joint. From experimental studies, it is found that in MFAF process parallel toolpath performs better than spiral toolpath while finishing Ti alloy at the nanometer level. 3D surface roughness parameter (*Sa* (arithmetic mean of absolute height), *Spk* (reduced peak height), *Sk* (core roughness depth) and *Svk* (reduced valley depth)) values of the finished surface provide an understanding of the surface characteristics. The optimum values of *Sa*, *Spk*, *Sk* (core roughness depth) and *Svk* are observed with 901 rpm of the tool, 0.60 mm working gap and 4.30 hrs. of finishing time. MFAF process provides nanometer level surface finish along with necessary surface topography for better wear properties to achieve better performance and longer femoral knee implant life. From experimental investigation, it is concluded that at high working gap, the finishing capability of abrasive particles reduces due to insufficient magnetic field in the finishing zone. Furthermore, after 6 hrs. of finishing time, the surface roughness of the workpiece increases again due to the ploughing effect by the abrasive particles on the already finished workpiece surface. The analysis of finishing forces involved in the present MFAF process is carried out for better understanding and precise control of the process.

Simulation study of MFAF process concerning finishing forces is carried out in two FEA based software. Validation experiments are conducted to substantiate the simulation study. A material removal model for a single abrasive particle is also simulated. A statistical DOE analysis is also conducted to evaluate the significance of each process parameter. After analysis of experimental results, it shows that F_n acting on the abrasive particles increases with increased CIP concentration. Although, the increase in abrasive concentration in the MR fluid, working gap and tool rpm results in a reduction in F_n. F_{tan} increases continuously with the increase in tool rpm, CIP concentration, abrasive concentration and decreases with working gap. MFAF tool has the ability to finish freeform surface of femoral knee implant almost uniformly along the surface curvature with necessary requirement of surface properties with minimum surface roughness (*Sa*) of 23.21 nm. Tribological study is carried out to analyse the performance of the MFAF polished surface compared to manually hand polished (HP) surface on ultra-high molecular weight polyethylene (UHMWPE) material of ASTMF648 standard used in tibial bearing surface. The volume loss analysis proves that the femoral knee implant polished using MFAF process will have fewer problems related to wear debris. The wear analysis shows that the wear of UHMWPE bearing surface will be less with MFAF polished femoral component. The wear of UHMWPE bearing surface will be less with MFAF polished femoral component as presumed from surface roughness analysis. The wear test analysis demonstrates that MFAF polished femoral surface will provide higher performance with a long implant life than hand polished surface.

TABLE OF CONTENTS

LIST OF FIGURES

LIST OF TABLES

NOMENCLATURES

N	Tool rotational speed
G	Working gap
T	Finishing time
Sa	Arithmetic mean of absolute height
Spk	Reduced peak height
Sk	Core roughness depth
Svk	Reduced valley depth
F_n	Normal force
F_m	Magnetic force
m_{CIPs}	Mass of magnetic particles (CIPs)
M	Magnetization
B	Magnetic flux density
μ_0	Relative permeability
H	Magnetic field strength
$\rho_{MRfluid}$	Density of MR fluid
M_m	Mass magnetization
$F_{\tan}$	Tangential force
F_{cfg}	Centrifugal force
F_s	Shear force
m	Mass of an abrasive particle
r	Distance of an abrasive particle from the tool central axis
τ_y	Yield stress
ϕ	Volume fraction of the CIP
A_p	Projected finishing spot area
J_e	Current density
A	Magnetic vector potential
σ	Stress
F_v	Force per unit volume

F_A	Total force on the boundary
C	CIP concentration
A	Abrasive concentration
D	Wear track diameter
N_d	UHMWPE disc speed
T_w	Wear test duration

Acronym

FTS	Fast tool servo
MFAF	Magnetic field assisted finishing process
GC	Grinding center
SAG	Shape adaptive grinding
MAF	Magnetic abrasive finishing
2D VAMAF	Two-dimensional vibration-assisted MAF
MRF	Magnetorheological finishing
MR fluid	Magnetorheological fluid
MRJF	Magnetorheological jet finishing
MRAFF	Magnetorheological abrasive flow finishing
R-MRAFF	Rotational magnetorheological abrasive flow finishing
MRFF	Magnetorheological fluid based finishing
CIPs	Carbonyl iron particles
CeO_2	Cerium oxide
SiC	Silicon carbide
Al_2O_3	Aluminium oxide
Ti	Titanium
CMP	Chemical mechanical polishing
H_2SO_4	Sulfuric acid
HF	Hydrofluoric acid
HNO_3	Nitric acid
H_2O_2	Hydrogen peroxide
FEA	Finite element analysis
DP	Diamond powder
DI	Deionized water

DOE	Design of experiment
RSM	Response surface methodology
CCRD	Central composite rotatable design
ANOVA	Analysis of variance
AFM	Atomic force microscope
FESEM	Field emission scanning electron microscope
TKA	Total knee arthroplasty
TKR	Total knee replacement
UHMWPE	Ultra-high molecular weight polyethylene

Chapter 1 Introduction and Literature survey

1.1 Introduction

Surface roughness defines the texture of the component surface. It helps to speculate component performance in real environment. For different purposes different surface roughness values are required. Wear and friction happen more in case of rough surface rather than smooth surface. Also, components with rough surfaces suffer more from corrosion and component failure. Surface roughness affects the operational efficiency of any component.

Freeform surfaces are generally characterized with the help of parametric and/or tessellated models. It contains one or more non-planar non-quadratic surfaces. Regular surfaces like planes, conic, cylinders etc. are different than freeform surfaces. It does not have any rigid dimension. This type of surfaces consists of non-planar surfaces. In product design, not only functionality but the aesthetics is also considered. Hence, the use of freeform surface is increasing in many industrial applications. Many freeform surface components are widely used in aerospace, automobile, consumer products, die & mold industries, medicine industries. Three main aspects of freeform machining are tool path generation, tool orientation and identification and tool geometry selection. Hence, for components having freeform surfaces, machining and finishing tool development is a very critical task. The most common method for freeform surface machining is ball end milling cutter or grinding wheel attached with a 3 or 5 axis CNC machining center. Recently, freeform components are also produced through injection molding and pressing. Also, diamond turning with Fast Tool Servo (FTS) systems, raster milling or grinding is used to machine freeform components. The next step is the finishing of freeform surfaces. To reduce scratches, deformation and produce smooth and mirror like surface finish, finishing processes are used. Smoothly polished equipment is a necessity in most of the industries especially in case of highly precise and sophisticated operations. Previously, for freeform surfaces especially with negligible tolerance, manual finishing was the only option. However, manual finishing is time consuming, labor intensive, error prone and costly. Hence, to achieve precise nanometer range surface finish and also deterministic finishing many researchers are developing new automated finishing technology. However, all automated technologies do not solve the problem of sub-surface damage at the workpiece surface and require longer time for high level finishing. Hence, to overcome the above mentioned

shortcomings of previous finishing processes, researchers are trying to develop newer polishing methods utilizing newer technologies. Magnetic Field Assisted Finishing (MFAF) process is one of the newly developed finishing process utilizing right composition of polishing fluid. This process generates very less sub-surface damage and can produce very good surface finish. Various freeform surface finishing processes available in the literature are discussed in the following section.

1.2 Freeform Surface Finishing Processes

Different freeform surface machining processes are described in this section.

1.2.1 Grinding

Grinding, an abrasive machining process is widely used as a finishing process. In this process, grinding wheel laced with the abrasive particle is used to finish the surface of the workpiece. Mizugaki et al. [1] attached an elastic grinding wheel with felt buff to the end effector of an industrial robot. It can easily follow the profile path of the freeform surface due to its higher degree of freedom incorporated with the industrial robot. Weulu and Timmermann [2] attached grinding paper of different grain size to a six-axis robot to finish the freeform surfaces like dies and molds. Huang et al. [3] reported about the finishing of turbine-vane overhaul using sand belt wheel as grinding as well as polishing media. Shiou et al. [4] used spherical grinding tool to finish freeform surface of a plastic injection mold steel on a CNC machining center. The spherical grinding tool and its alignment components are developed by them. Wu et al. [5] used an elastic ball type wheel with GC (grinding center) to polish the freeform surfaces of die and mold. Only cusp height is removed in this process to keep the form accuracy generated in cutting process. Beaucamp et al. [6] proposed shape adaptive grinding (SAG) to nano-finish freeform surface made of Ti6Al4V alloy. In SAG an inflated and tilted spherical rubber bonnet is covered with nickel or resin bonded diamond pellets. This process introduces benefits of both grinding and polishing techniques. Schematic diagram of the SAG is shown in Fig. 1.1(a).

1.2.2 Honing

Honing is performed by a honing tool or honing stone which is actually an abrasive stick or abrasive stone. After applying pressure, the honing tool abrades the workpiece surface along a predefined path. Weulu and Timmermann [2] used honing stone to finish the freeform surface of dies and molds. The honing stone is attached with the six-axis robot for better flexibility. Nowicki and Szafarczyk [7] attached abrasive sticks having two or four degrees of freedom with the machining head of a NC milling machine. The abrasive sticks rotate with the machine head and feed is given to the workpiece in X, Y and Z directions. Dynarowski and Nowicki [8] also used non-conventional honing to achieve low surface roughness on freeform surfaces made of alloy steel. Figure 1.1(b) shows the schematic diagram of the non-conventional honing experimental set-up to polish freeform surface.

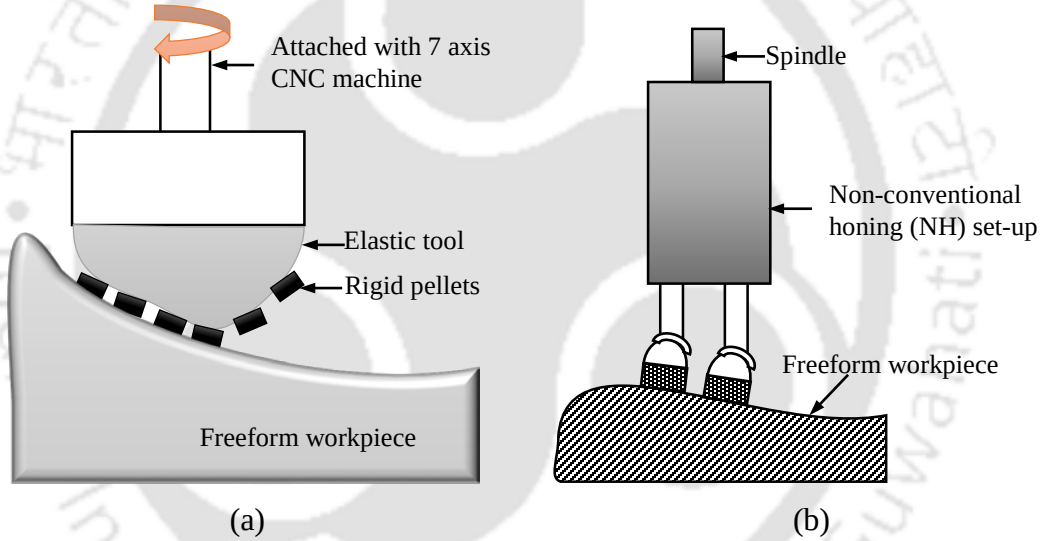

Fig. 1.1 Schematic diagram of (a) shape adaptive grinding (SAG) and (b) non-conventional honing of free-form surfaces

1.2.3 Abrasive Polishing Process

In this sub-section, the main consideration is the soft, flexible abrasive polishing process. For finishing of freeform surface this type of abrasive polishing process is more suitable. This type of polishing tool also helps to keep the form accuracy intact. Tam et al. [9] used a robot to finish freeform surface using loose abrasive. They explored the scanning path of workpiece surface for the movement of the robotic arm to enhance the evenness of a free-form surface. Cho et al. [10] developed a flexible abrasive tool attached with a 3-axes machining center to automatically finish the curved surface. The tool is made of thermosetting polyurethane elastomer with aluminum oxide

abrasive coating. Walker et al. [11] used a commercial machine 'Precessions' from Zeeko Ltd. for finishing freeform surfaces using polishing slurry. Their polishing tool is attached with a 7-axes CNC machine. The polishing tool is semi spherical in shape and it consists of an inflated, bulged rubber membrane of spherical form covered with a non-pitch flexible polishing surface. Brinksmeier et al. [12] improved the surface roughness of structured molds by abrasive polishing using pin type and wheel type polishing tool made of polyamide which is retrofitted with a commercial polishing machine. The schematic diagram of curved surface finishing using soft abrasive tool is represented in Fig. 1.2.

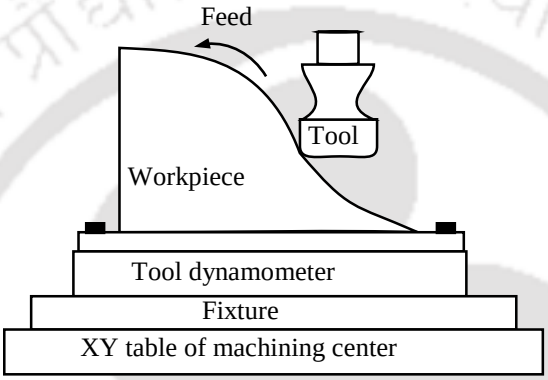

Fig. 1.2 Schematic diagram of curved surface finishing using soft abrasive tool

1.2.4 Electrochemical Finishing Process

Electrochemical finishing is one of the nonconventional finishing process. Both the workpiece and the tool are immersed in the electrolyte. In this process, the workpiece acts as anode (connected to the positive terminal of a power supply) and the negative terminal is attached to the cathode. The tool and workpiece are connected to a DC power supply. Metal from the surface of the anode is oxidized and dissolved in the electrolyte and at the cathode reduction reaction occurs. Any complicated shapes like freeform surfaces can be easily finished with this process. Pa [13] developed magnetic assistance electrochemical finishing process to finish freeform surface. The magnetic assistance helps to remove the dregs from the inter electrode gap generated during finishing. He concluded that due to magnetic assistance better finish, reduced finishing time is achieved. Pa [14] also used ultrasonic assistance along with magnetic assistance to improve finishing performance. Experimental setup of magnetic assistance electrochemical finishing is shown in Fig. 1.3.

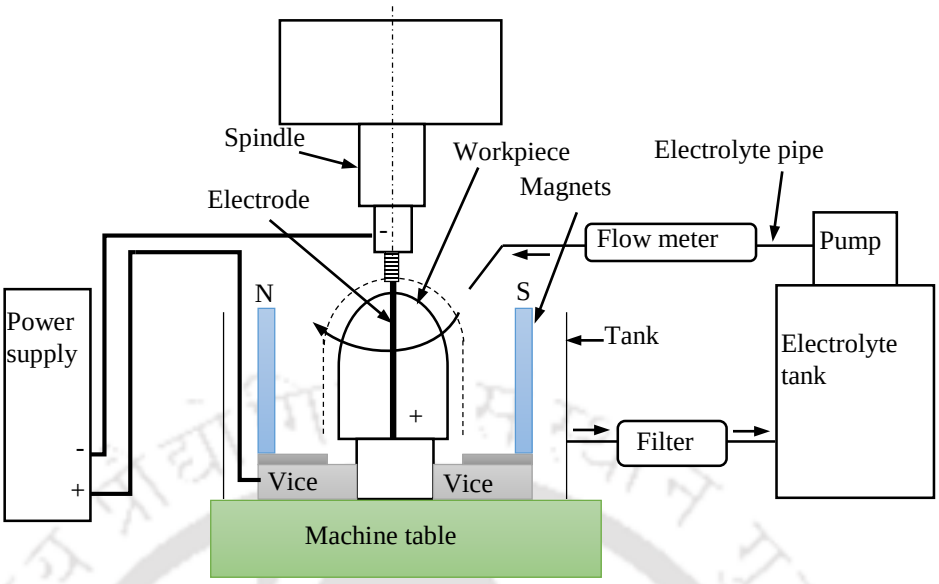

Fig. 1.3 Experimental setup of magnetic assistance electrochemical finishing

1.2.5 Ball Burnishing Process

Ball burnishing process used to finish the workpiece using a ball. The ball impacts on the workpiece and peening over the peaks of the surface profile. The undulations rolled or pounded over by the ball as there are no abrasive involved. This process also hardens the workpiece and improve the corrosion resistance of the workpiece due to the 'peening effect'. Shiou and Chen [15] modified a ball burnishing tool attached with CNC milling machine to finish plastic injection mold. The optimal burnishing process parameters also determined using different statistical techniques. Pa [16] incorporated burnishing process along with electrochemical process to finish freeform surfaces. The ball burnishing tool is attached to the electrode of an electrochemical process. This hybrid process requires shorter finishing time with improved finishing effect. Schematic diagram of the ball burnishing process is shown in Fig. 1.4.

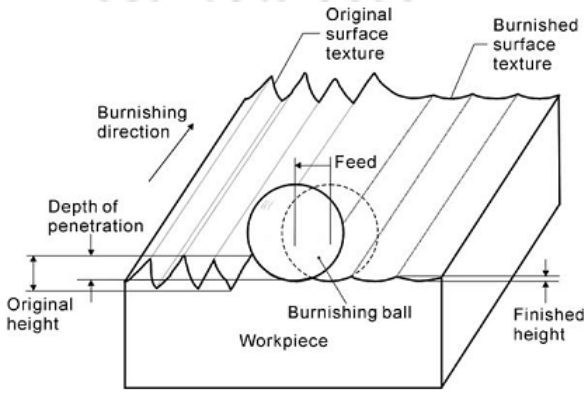

Fig. 1.4 Schematic diagram of ball burnishing process [16]

1.2.6 Magnetic Field Assisted Finishing (MFAF) Process

Magnetic Field assisted finishing (MFAF) process uses external magnetic field for better control of the finishing forces. This process can easily produce mirror like surface finish. Different types of MFAF processes are discussed as follows:

1.2.6.1 Magnetic Abrasive Finishing (MAF)

MAF produces high quality mirror like surface with the help of external magnetic field. In this process, magnetic abrasive particles (MAPs) are used as polishing medium. The working gap between magnet and workpiece is filled with magnetic abrasive particles which create a flexible magnetic abrasive brush. This brush acts as a cutting tool under external magnetic field. The material removal rate in this process is very low due to the small indentation of abrasive particles. In this process, either permanent magnet or electromagnet can be used depending on the process requirement. MAF process can be used for finishing both internal as well as external surfaces. The schematic diagram of MAF is shown in Fig. 1.5. The important process parameters of MAF process are as follows:

- Magnetic field intensity
- Working gap between magnetic pole face and the work piece surface
- Work piece material, shape, and size
- Pole shape and size
- Composition of magnetic abrasive particles

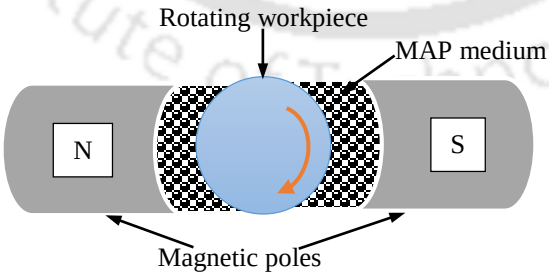

Fig. 1.5 Finishing of cylindrical workpiece using MAF

Shinmura et al. [17] developed a new finishing process where magnetic abrasive particles are used for finishing purpose. The required finishing pressure is generated by magnetic field.

They studied different finishing characteristics specially the effect of magnetic abrasive particle size on material removal rate and surface finish for cylindrical workpiece.

Kim et al. [18] developed magnetic abrasive jet machining to precisely finish circular tubes. Their working fluid is mixed with magnetic abrasive particles and it is delivered into the internal surface of the tube as magnetic abrasive jet. The magnetic poles are fixed at the external surface of the tube. They did simulation study to predict optimum machining conditions and to analyze few characteristics of the finishing process.

Yamaguchi and Shinmura [19] developed an internal magnetic abrasive finishing process using a pole rotation system to produce highly finished inner surface of workpiece used in critical applications. Their study characterizes the abrasive behavior against the surface during finishing process and predicts the effect of the abrasives on finishing characteristics.

Jain et al. [20] proposed a MAF setup for finishing of cylindrical workpiece mounted on a lathe machine using loosely bonded magnetic abrasive particles mixed with lubricant. Their workpiece is kept between two opposite magnetic pole. The working gap and magnetic field between the two magnets control the force required for finishing. Experiments are conducted to explore the effect of various process parameters on change in surface roughness of workpiece.

Chang et al. [21] explained the working principle and the finishing characteristics of unbonded magnetic abrasive particles during finishing of cylindrical workpiece. The magnetic abrasives used in their study consists of abrasive particles and ferromagnetic particles mixed with lubricant. Different types of ferromagnetic particles are used and a comparative study is carried out.

Mori et al. [22] reported about MAF process mechanism considering magnetic field and finishing forces within the process. Yamaguchi and Shinmura [23] developed a new MAF setup for finishing inner surface of alumina ceramic components with a mixture of conventional abrasive and ferrous particles. The experiments are conducted on alumina ceramic tubes to examine the effect of various process parameters on finishing performance. Their study also reports on the mechanism of smoothing inner surface of alumina ceramic tube and form accuracy improvement.

Yin and Shinmura [24] proposed a vertical type vibration-assisted magnetic abrasive finishing process to finish and deburr complicated micro-curved and edge surfaces of magnesium alloy. They reported that efficient finishing of magnesium alloy is possible by their process.

Yamaguchi et al. [25] explored the conditions required for uniform internal finishing of SUS304 stainless steel bent tube by a MAF process. The factors affecting the finishing condition are investigated in their study.

Yamaguchi et al. [26] developed a magnetic abrasive finishing setup for internal finishing of SUS304 austenitic stainless steel capillary tubes.

Yamaguchi and Hanada [27] developed a spherical iron-based magnetic abrasive particles by plasma spray which carries electrolytic iron particles and aluminium oxide (Al_2O_3) as abrasive grains. The performance of their developed magnetic abrasive particles is compared with the existing magnetic abrasive particles. The developed magnetic abrasive particles are used for internal finishing of capillary tubes and achieved improved finishing performance.

Kang et al. [28] developed a method for finishing capillary tube in high speed MAF technique. In their experimental setup, a high-speed multiple pole-tip finishing equipment is used. They described the effect of tube rotational speed on abrasive motion during finishing experiments.

Lee et al. [29] proposed to increase MAF process efficiency by introducing vibration to the platform. The process is termed as two-dimensional vibration-assisted MAF (2D-VAMAF) process. They found that 2D-VAMAF can improve surface quality in lesser time using lesser quantity of abrasive particles which reduces polishing cost.

1.2.6.2 Magnetorheological Finishing (MRF)

MRF process uses magnetorheological (MR) fluid with an external magnetic field to finish workpiece surface at the nanometer level without sub surface damage. This process is primarily used to finish optical materials with different shapes such as flat, spherical, concave and convex. This process is developed in Center for optics manufacturing (COM) in Rochester, New York [30]. MRF process is fully commercialized by QED technologies in 1999. Figure 1.6 shows the schematic diagram of MRF process.

There are many newly developed magnetic field assisted finishing processes which use MR fluid as a polishing medium. Few of these processes are Magnetorheological jet finishing (MRJF), Magnetorheological abrasive flow finishing (MRAFF), Rotational magnetorheological abrasive flow finishing (R-MRAFF) and Ball end magnetorheological finishing (BEMRF) process etc.

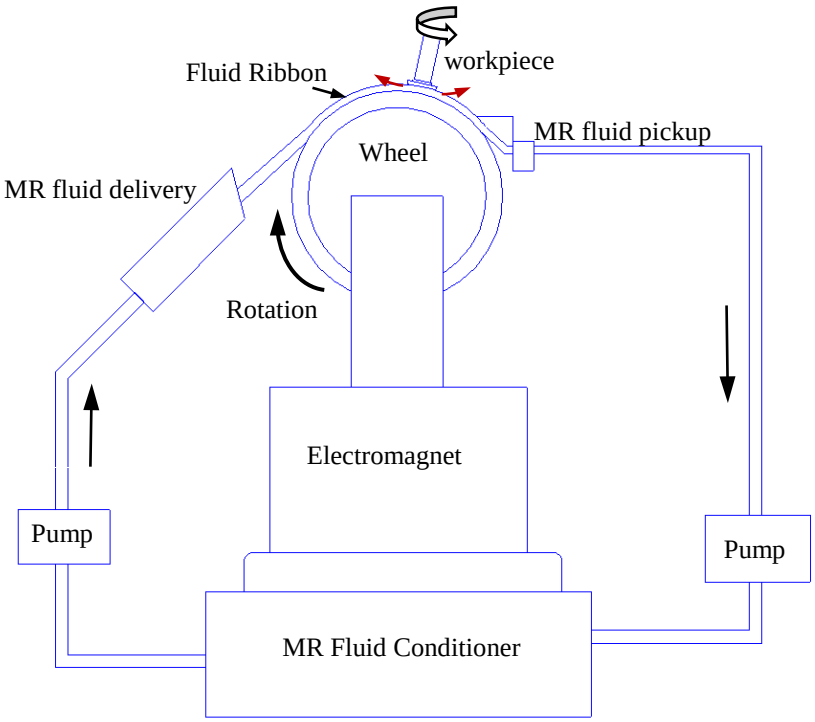

Fig. 1.6 Schematic diagram of MRF process

In MRF process a rotating wheel is used to transport the fluid in the finishing zone. MR fluid is delivered on the rim of the wheel by a nozzle. The fluid acts as a moving ribbon on the wheel and it gets stiffen with the application of the external magnetic field. The MR fluid is circulated continuously during the process and it sticks to the wheel due to applied magnetic field. The stiffened MR fluid ribbon generates a unique pressure distribution in the gap between the workpiece and the wheel (Fig. 1.7).

High shear stress is generated in the contact zone due to the quasi-solid moving boundary formed very close to the surface of the workpiece. The high shear stress helps in material removal from a particular area of workpiece surface. That area is called as polishing spot. The MR fluid contains abrasive particles to carry out finishing operation. Due to the nonmagnetic nature, the abrasive particles are forced towards the workpiece surface due to magnetic field gradient. The

shear stress of the flowing ribbon of MR fluid mixed with abrasives generates a drag force which helps in material removal [30,31].

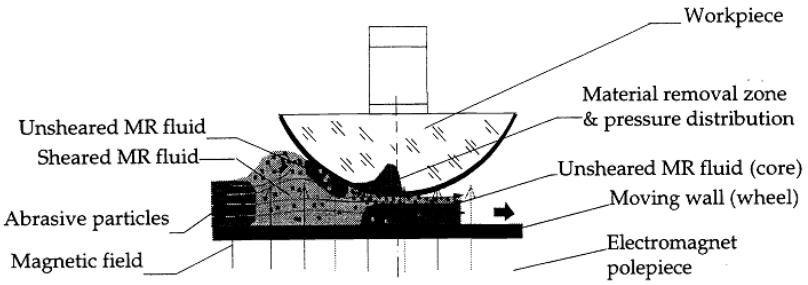

Fig. 1.7 Mechanism of MRF process [30]

The yield stress and viscosity of MR fluid are controlled by externally applied magnetic field which in turn is controlled by the magnetizing current in the electromagnet coils. The MR polishing fluid consists of magnetic carbonyl iron particles (CIPs), nonmagnetic abrasive particles dispersed in the carrier fluid. The application of external magnetic field affects the rheological properties of the fluid. With the application of the magnetic field, CIPs aggregate into chain like structure along the magnetic field direction embedding the abrasive particles in between the chains. Several researchers have developed different types of wheels and also used permanent magnets instead of electromagnets.

Cheng et al. [32] developed a two axis wheel shaped tool supporting double magnetic fields. They carried out experiments using this type of wheel to polish K9 mirror with MR fluid composition of 33.84% CIP, 57.34% silicone oil, 2.82% stabilizing agent and 6% Cerium Oxide (CeO_2). Later, Cheng et al. [33] conducted an experimental study on reaction bonded silicon carbide (SiC) components using MRF process with MR fluid composition of 36% CIP, 6% abrasive particles (CeO_2, Al_2O_3 and diamond), 3% stabilizer (silicon oil) and 55% carrier fluid (water). They reported that diamond particles give higher material removal rate compared to other abrasive particles.

Sidpara and Jain [34] used MRF process to finish single crystal silicon wafer. They conducted experiments to study the effect of different process parameters on surface finish and material removal rate with best achieved surface roughness as 8 nm.

Experimental study on silicon wafer and conductor surface, fabricated by electroplating process on a CMOS grade silicon substrate with a polyimide interface layer, have been reported by several researchers by using different polishing tool using MRF technique [35,36].

1.2.6.3 Magnetorheological Jet Finishing

Kordonski et al. [37] and Tricard et al. [38] developed MR jet finishing technology to finish conformal or freeform and steep concave optics. This type of optics is difficult to finish using conventional methods due to mechanical interference and steep local slopes. It has been found that magnetically stabilized round jet of MR polishing fluid removes material at a distance of several tens of centimeters from the nozzle. Figure 1.8 shows MR jet images with and without application of magnetic field having velocity of 30 m/s and nozzle diameter of 2 mm.

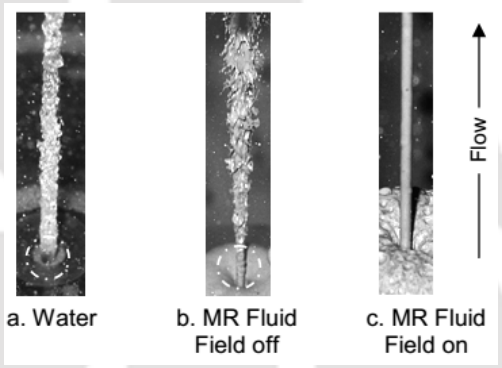

Fig. 1.8 Images of MR Jet [38]

1.2.6.4 Magnetorheological Abrasive Flow Finishing (MRAFF) Process

Jha and Jain [39] developed MRAFF process. In this process, extrusion of a magnetically stiffened MR polishing fluid move to and fro through the passage formed by workpiece and workpiece fixture assembly and finishes the workpiece surface. In this process, two cores of an electromagnet which are placed opposite to each other outside workpiece fixture is used to generate magnetic field. The finishing mechanism of MRAFF process is shown in Fig. 1.9.

The CIP particles embed the abrasive particles and form a chain like structure. Applied extrusion pressure on the polishing fluid helps in finishing the workpiece. Jha and Jain [40] reported that MRAFF process can super finish hard materials like silicon nitride using boron carbide, silicon carbide and diamond abrasives.

Jha et al. [41] carried out experimental investigation to study the effect of different process parameters on the change in surface roughness. To enhance the process performance of MRAFF process, Das et al. [42] modified the existing MRAFF process by imparting a rotating motion to the polishing medium by an external rotating-magnetic field. The schematic diagram of MRAFF & rotational motion imparted by the rotating magnetic field are shown in the Figs. 1.10(a) and (b), respectively.

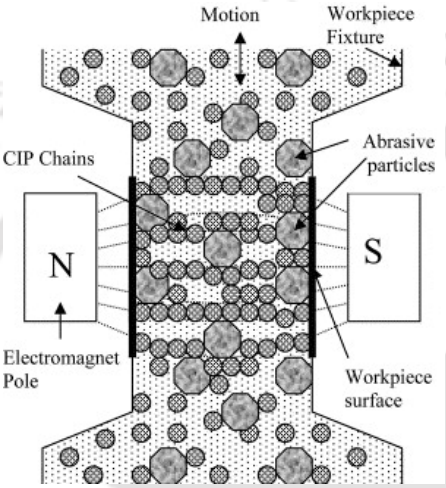

Fig. 1.9 Mechanism of finishing in MRAFF process [39]

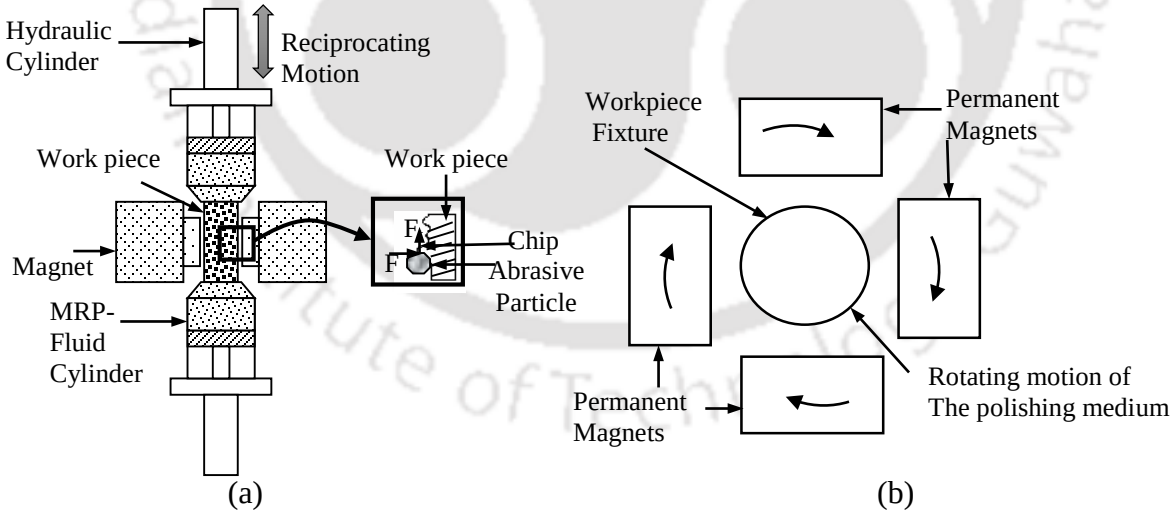

Fig. 1.10 (a) Schematic diagram of MRAFF process [40] and (b) rotational motion imparted to the permanent magnets in R-MRAFF process [43]

1.2.6.5 Ball End Magnetorheological Finishing (BEMRF) Process

To finish 3D complex shapes, Singh et al. [44] developed a new precision finishing process named as ball end MR finishing process as shown in Fig. 1.11. In this process, pressurized MR

polishing fluid enters from the top end of the central rotating core. As soon as it reaches to the tip of the tool surface, the MR fluid stiffens due to the application of the applied magnetic field in that zone. A semi solid structure of ball end shape of the finishing spot is formed at the tip of the rotating core. The tool is rotated like in conventional ball end milling process and the feed is provided to the workpiece which is attached to an X-Y table.

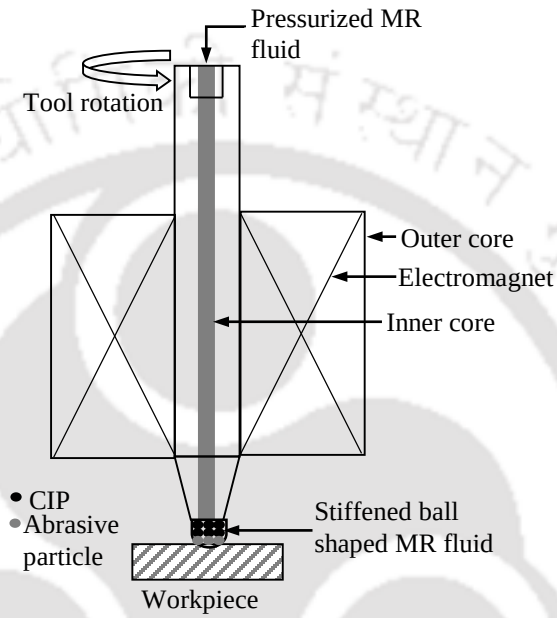

Fig. 1.11 Schematic diagram of ball end MRF process

1.3 Literature Survey

MFAF processes are precise finishing process where magnetic field is used to control the forces involved during finishing. Using these processes deterministic finishing can be easily achieved. The following subsections describe the work reported in the area of MFAF processes. In subsection 1.3.1 literature review about MR fluid is presented, in subsection 1.3.2 relevant literature survey on workpiece material for the present work is discussed, in subsection 1.3.3 literature survey on experimental investigations of MFAF process is described, and in subsection 1.3.4 theoretical investigation into MFAF process i.e. mathematical modelling and force and stress analysis is presented.

1.3.1 Magnetorheological (MR) Fluid

The finishing performance of magnetorheological (MR) fluid based finishing process depends upon the composition of MR fluid. The change in rheological property of MR fluid due to the applied magnetic field affects finishing performance of MFAF process. The rheological property of MR fluid depends upon composition and concentration of different elements in MR fluid. So, composition of the MR fluid is a very critical part of the finishing process. Rabinow first developed Magnetorheological fluid as a smart fluid in 1948. He reported about the change in rheological property of MR fluid after applying the magnetic field [45]. MR fluid consists of magnetic particles in a viscoplastic base medium such as water, glycerol, silicone oil, paraffin oil with some additives. Non-magnetic abrasive particles are mixed with the MR fluid for material removal. The fluid acts as a Newtonian fluid when there is no magnetic field and it acts as non-Newtonian fluid under magnetic field. This fluid becomes stiff under magnetic field. Hence, for the flow of MR fluid some external pressure is required.

There are two types of MR fluid i.e. water based and oil based. It has been found that finishing of metals are mostly carried out using oil based MR fluid. So there is less corrosion due to oxidation of metallic parts of experimental set up in case of oil based MR fluid. Oil based MR fluid generally consists of CIPs, abrasive particles and paraffin oil as base medium. Water based MR fluid is primarily used for finishing of silicon wafer, optical materials. The water in MR fluid chemically reacts with the silicon and optical materials i.e. glass etc. Water based MR fluid consists of CIPs, abrasive particles, deionized water as base medium and glycerol as additive [34,39,42,46].

In MR fluid, magnetic particles agglomerates and develops stiff sediments due to their remnant magnetization and these agglomerated particles are very difficult to break-up. To reduce particle agglomeration and settling different methods proposed by several researchers are as follows:

- Adding thixotropic agents like carbon fibers, nanoparticles of silica etc. to MR fluid [47,48]
- Adding surfactants like Oleic acid or stearic acid etc. to MR fluid [49]
- Using viscoplastic base medium as a continuous phase [50]
- Water in oil emulsions as carrier liquid [51]
- Adding magnetic nanoparticles to MR fluid [52,53]

Glycerol and surfactants are used in water based fluid as stabilizers. Ginder et al. [54] proposed both numerical and analytical models of MR fluid that account explicitly magnetic

nonlinearity and saturation. Jolly et al. [55] developed a quasi-static, one-dimensional model that examines the mechanical and magnetic properties of magnetorheological materials. Their model attempts to account for magnetic non-linearities and saturation by establishing a mechanism by which magnetic flux density is distributed within the composite material. Few researchers reported about the characterization of MR polishing fluid.

Jha and Jain [56] used hydraulically driven capillary rheometer for rheological characterization of MR polishing fluid and discussed three different fluid models (Bingham plastic, Herschel Bulkley and Casson fluid) to characterize its behavior. Sidpara et al. [46] did rheological characterization of MR polishing fluid using parallel plate magnetorheometer for water based MR polishing fluid. Their findings also show that MR polishing fluid follows shear thinning behavior (fluid viscosity decreases with increasing shear rate). They also reported that Herschel-Bulkley model best fitted their MR polishing fluid.

1.3.2 Workpiece Material

In the present work, titanium (Ti) alloy of grade 5 is used as the workpiece material. It is used largely in the medical industry due to its corrosion resistance and inertness towards the bodily fluids. It is also used to fabricate different types of implants [57]. The density of Ti alloy (grade 5) is 4.5 g/cm^3 and its chemical composition is provided in Table 1.1 according to American society for testing and materials [58]. The specific strength of the Ti alloy is also higher than the other implant materials [59].

Table 1.1 Chemical composition of Ti alloy (grade 5)

Main Elements	Wt.%
Titanium	89.5
Aluminum	6
Vanadium	4

Ti alloys have relatively low modulus than some of the implant materials making it a very good choice for orthopedic application [60]. Niinomi reported the mechanical properties of Ti alloy used for biomedical applications [61]. The Mechanical properties of annealed Ti alloy (grade 5) for biomedical applications are represented in Table 1.2.

Different finishing processes are employed to modify the titanium and Ti alloy for different biomedical application. Basim et al. proposed chemical mechanical polishing (CMP) to finish Ti

alloy for bio-medical application [62]. They reported that CMP can make titanium surface more biocompatible by forming a protective oxide layer.

Table 1.2 Mechanical properties of Ti alloy (grade 5, annealed) [61]

Mechanical property	**Value**
Tensile strength(UTS)	(895–930) MPa
Yield strength(σ_y)	825–869
Elongation	(6–10)%
Percent reduction in area (RA)	(20–25)%
Modulus	(110–114) GPa
Type of alloy	$\alpha + \beta$

Tamaki et al. [63] reported the polishing of titanium prosthetics inside a chemical polishing bath containing mixture of hydrofluoric acid and nitric acid. They also reported that the prosthetic immersed in the low soluble chemical polishing bath for a long time provides smooth surface along with form accuracy.

Hayes et al. [64] used electropolishing and plate polishing technique to polish titanium screws used for biomedical application. They reported that removal of the finished screws is far easier than the rough screws.

Ban et al. [65] effectively modified the titanium surface for biomedical application by etching it in 48% sulfuric acid (H_2SO_4). They characterized the etching behavior of titanium in concentrated H_2SO_4.

Khanlou et al. [66] changed the surface texture and roughness of titanium biomaterial by employing sandblasted, large-grit, acid-etched (SLA) method. They used alumina abrasive particles for sand blasting. For titanium etching, Kroll's etchant (3 ml hydrofluoric acid, 6 ml nitric acid and 100 ml water) is utilized.

Finke et al. [67] proposed a finishing method for temporary titanium implants. Here, plasma process is used to deposit fluorocarbon polymer films on titanium. This process prevents cell adhesion of osteoblasts which is major concern for temporary implants.

The magnetoelectropolishing process is proposed by Hryniewicz et al. [57] to improve corrosion resistance of titanium implant. In this process, magnetic field is externally applied to achieve required surface characteristics of medical implants.

Okada et al. [68] proposed a large-area electron beam (LAEB) irradiation finishing process for finishing Ti alloy used for biomedical applications. In LAEB, high energy density electron beam is irradiated to melt and evaporate Ti alloy surface.

Okawa and Watanabe [69] used CMP for polishing titanium for biomedical application. A mirror polished surface without reacted or contaminated layer is achieved by using colloidal silica slurry mixed with hydrogen peroxide (H_2O_2). The researchers proposed this method to solve the problems encountered in electrochemical polishing and electropolishing of titanium used in biomedical application.

According to the literature review, titanium and its alloy surfaces are modified for different biomedical application. Two type of implants, permanent and semi-permanent or temporary implants are used in medical industries. These two type of implants require different surface roughness and surface texture. Implant surface is either roughened or superfinished depending upon it's in vivo performance. In some cases, osseointegration i.e. direct contact between bone and an implant without infringing soft tissue is required. Keller et al. [70] reported that osteoblast cell attachment is highest when the implant surface is rough. Other researchers also reported the same findings [71,72]. If an implant is engaged in relative motion in vivo or it is used temporarily then surface roughness should be at the nanometer level. Also, the surface topography of the implant should be such that the in vivo wear of the implant is minimal which restricts the mixing of implant metal debris in the blood flow for reducing implant related pain. The generation of debris during in-vivo performance of an implant introduces a serious problem in patient body. The accumulation of wear debris around the implant prompts to a big cell response. The metallosis of periprosthetic tissue i.e. black stain in periprosthetic tissue is observed in Ti alloy knee implant due to this wear debris as reported by Breen and Stoker [73]. Hence, the performance and life of the implant are largely dependent on the surface roughness and surface topography of the component surface [74,75].

1.3.3 Experimental Investigation

In this sub-section, work done on different type of magnetic field assisted finishing setup is discussed. Suzuki et al. [76] developed a magnetic field assisted polishing process for polishing curved surface made of single crystal of $LiNbO_3$. They achieved 0.01 μm surface roughness using

colloidal silica as polishing abrasive. Ferricolloid W-40 is used as the magnetic fluid. A polishing disk is used to polish the hard and brittle workpieces. Figure 1.12 depicts schematic illustration of their experimental setup.

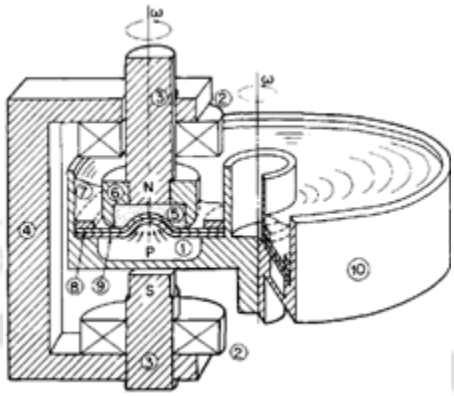

Fig. 1.12 Schematic diagram of polishing setup where, 1-magnetic field, 2- coil, 3- iron pole, 4- iron support, 5- workpiece, 6- jig, 7- polishing abrasive, 8- polisher, 9- rubber sheet, 10- brass disc [76]

Kim et al. [77,78] described a magnetic field assisted polishing technology to finish freeform surface. A flexible magnetic polishing tool and two stage polishing method are employed for 36 minute to obtain mirror like surface finish. At first stage, GC#400 wheel used to decrease the initial surface roughness value to 0.64 µm and in the second stage magnetic abrasive brush is used to further decrease the surface roughness value to 0.09 µm. Figure 1.13 shows the schematic diagram of two types of magnetic polishing tools.

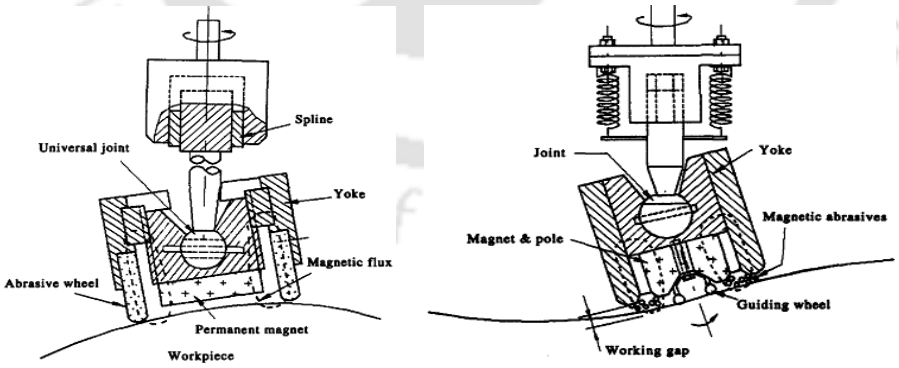

(a) (b)

Fig. 1.13 Schematic diagram of 3D polishing tools (a) Abrasive wheel type and (b) magnetic brush type [78]

Kim et al. [79] proposed a new surface finishing method for finishing three-dimensional silicon microstructure using stiffened MR fluid. For finishing of microchannels, the existing setups are not good enough due to very high hydrodynamic pressure that destroys the channel structure.

To overcome this problem, they developed a setup where the permanent magnet is vertically attached with the magnet holder. A rotational motion is provided to the magnet. Cerium Oxide (CeO_2) is used as abrasive particle in the polishing medium. They reported improved performance of microchannels. Figure 1.14 depicts schematic diagram of experimental set up for finishing silicon microchannel.

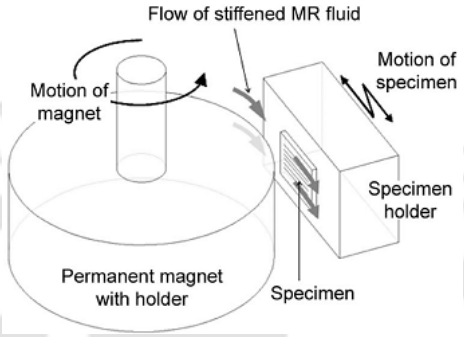

Fig. 1.14 Schematic diagram of experimental set up for microchannels finishing [79]

Tricard et al. [38] reported Magnetorheological Jet finishing technology to finish freeform and steep concave optics. A liquid jet of magnetorheological fluid impinges on the surface of the workpiece. The schematic diagram of the process is given in Fig. 1.15.

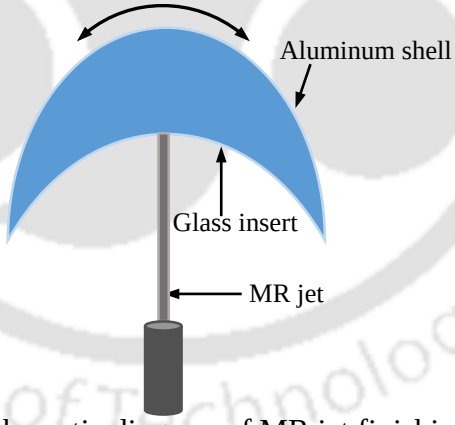

Fig. 1.15 Schematic diagram of MR jet finishing process

The round jet is magnetized by an axial magnetic field when it flows out of nozzle. The main problem of jet polishing is to remain collimated and coherent before impinging on the workpiece surface. Due to the magnetic force the jet overcomes above stated problem. They finished different shaped complex freeform optics by varying process parameters like jet velocities, nozzle diameter and fluid viscosity. This process can produce high precision surface on glass and single crystal components. However, this process may not be good for optical workpiece having high initial surface roughness value.

Seok et al. [80] fabricated a curved surface on silicon based microstructure by using MRF process. Here, MRF process is applied as a shaping process to make a curved surface from a sliced rectangular piece of a silicon wafer by applying edge effect (i.e. rounding off on sharp edges) which is undesirable during normal finishing process. They didn't add abrasive particle to MR fluid. The finishing tool assembly is composed of a cylindrical permanent magnet and an automobile wheel shaped rim. Schematic diagram of the MR finishing tool assembly is shown in Fig. 1.16.

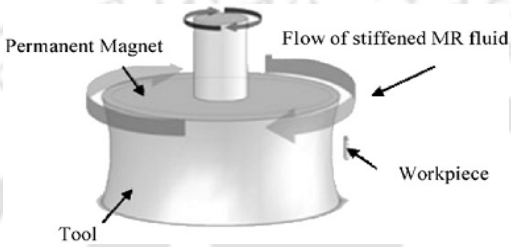

Fig. 1.16 Schematic diagram of MR finishing tool assembly [80]

Lin et al. [81] employed a magnetic abrasive finishing to finish freeform surface of non-ferromagnetic stainless steel SUS304 workpiece. The ball shaped magnetic pole forms a flexible magnetic abrasive brush for finishing process. Figure 1.17 illustrates magnetic abrasive finishing of freeform surface. They found that most significant process parameters are working gap, feed rate and the abrasive concentration following Taguchi method. They obtained final surface roughness of 0.102 μm using two step finishing process.

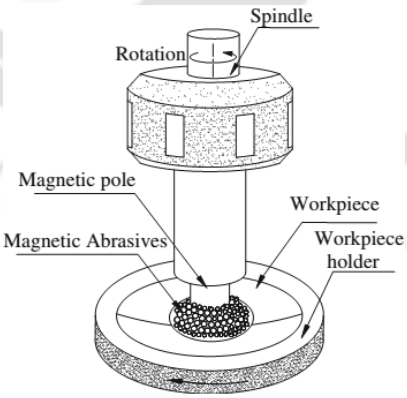

Fig. 1.17 Schematic diagram of freeform magnetic abrasive finishing process [81]

Singh et al. [44] developed a ball end magnetorheological finishing (BEMRF) tool for finishing of 3D copper groove surface. The MR finishing tool is vertically oriented on a Z slide. The tool consists of concentrically inner core, electromagnet coil and an outer core. After application of magnetic field, MR fluid becomes stiff. At the tip of the tool MR fluid comes out in

ball shape. The surface roughness of the groove surface is reduced from 336.8 nm to 102 nm in 60 min finishing time. The same experimental setup with some modification has been used to finish 3D ferromagnetic workpiece at different angles of projection such as 0^0 (flat surface), 30^0, 45^0 and curved surface [82,83]. The workpiece is prepared by milling process. The final surface roughness is obtained as 16.6 nm, 30.4 nm, 71 nm and 123.7 nm on flat, 30^0 and 45^0 and curved surface, respectively. It is also observed that the variation in magnetic field due to the difference in curvature can be minimized by tilting MR finishing tool. They reported that ground surface provides better process performance than milled surface.

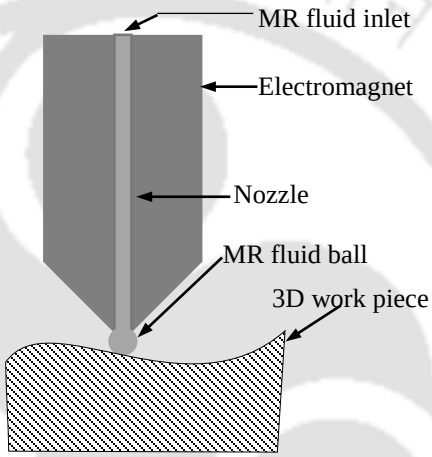

Fig. 1.18 Schematic diagram of Ball End MR finishing process

Sidpara and Jain [84] developed a setup using MR fluid as polishing fluid to finish freeform surfaces of prosthetic knee joint implant made of titanium. They developed a MRFF (Magnetorheological fluid based finishing) tool. The tool encloses a permanent magnet in a fixture of brass material. The experiments are carried out stepwise by changing MR fluid composition to increase the finishing performance. The polishing fluid is supplied in between the tool and workpiece. Water based MR fluid as well as chemical based MR fluid are used and their effects are observed on surface roughness and finishing rate. The best surface finish achieved is 28 nm.

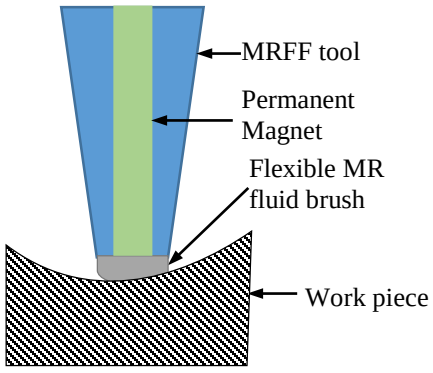

Fig. 1.19 Schematic diagram of MRFF process

Yamaguchi and Graziano [85] also used magnetic abrasive finishing process to finish freeform surface of cobalt-chromium prosthetic knee joint implant. A six axis robot is used to hold the knee joint using a workpiece holder. Magnetic particles mixed with diamond abrasive is used as polishing medium which is supplied at the pole tip (carbon steel) during finishing. They developed a workpiece holder to hold the workpiece during finishing as well as to measure surface roughness at difference places. The average surface roughness achieved is 6.7 nm.

1.3.4 Theoretical Investigation

1.3.4.1 Mathematical Modelling

In MFAF process, the material removal rate is similar to conventional polishing process. So, Preston's equation [86] is considered as the building block to understand and develop mathematical modelling for the process. Preston's equation for material removal rate is given as

$$MRR = C_p PV = C_p \frac{F_n}{A_c} V \tag{1.1}$$

where C_p = Preston's coefficient, P = applied normal pressure, V = relative velocity between tool and workpiece, F_n = normal force, A_c = contact area between tool and workpiece.

Modelling of material removal rate is reported by Tricard et al. [38]. They modified Preston's equation for their analysis. The material removal rate is proportional to the product of local shear stress and local fluid velocity. Their proposed model is simulated using a commercial CFD package and the results are validated with experiment. The parameters used in the calculation are jet radius, mesh area and mesh size. Their proposed model is

$$\dot{R}_r \sim \tau_r V_r \tag{1.2}$$

where R_r = material removal rate, V_r = local fluid velocity, τ_r = local shear stress.

DeGroote et al. [87] also modified Preston's equation for calculating material removal rate of optical glasses finished by MRF process with nanodiamond abrasive particle. They observed

that peak removal rate and drag force did not show same relationship for different glasses due to their different chemical property and composition. Hence, they incorporated mechanical properties of glass surface, drag force (F_d) or shear stress, polishing particle properties, chemical properties of the workpiece and polishing fluid into the modified Preston's equation for better understanding of the process. The theoretical model is validated with experiments for six different types of glass workpieces. The other process parameters i.e. wheel speed, magnetic field, viscosity working gap etc. are kept constant throughout the experiments. Their material removal model is given as

$$MRR_{peak} \propto \left[\frac{E_S}{K_c.H_s^2}\right]\left[\frac{F_d}{A}.v\right]\times\left[B_{nd}\phi_{nd}^{-1/3}.C_{nd}^{1/3}+B_{CI}\phi_{CI}^{4/3}.C_{CI}\right]\times\left[D_s\left(pH_{MRF}\right)^{3/10}\right]\left[e^{-\frac{sbs}{bRT}}\right] \quad (1.3)$$

where E_S = Young's modulus, K_c = fracture toughness of the bulk material, H_s = nanohardness of the near surface layer, A = contact area, v = velocity of the wheel, B_{nd} and B_{CI} = coefficients, ϕ_{nd} and C_{nd} = average particle size and concentration of nanodiamond particles, ϕ_{CI} and C_{CI} = average particle size and concentration of CIP, $D_s\left(pH_{MRF}\right)$ = percent weight loss of the glass in the MR fluid, $e^{-\frac{sbs}{bRT}}$ = glass average single bond strength.

Jung et al. [88] developed a theoretical model to calculate total force exerted on the CIP particles at the workpiece surface. The total force is composed of centrifugal force and magnetic force. Figure 1.20 depicts the forces acting on CIPs in MRF process.

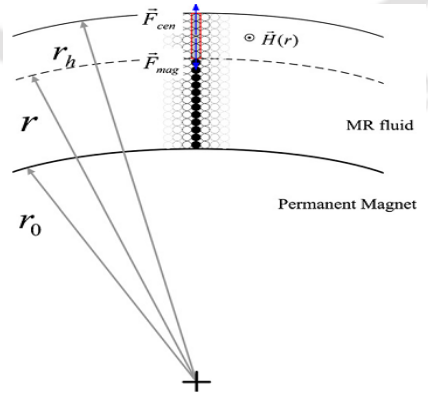

Fig. 1.20 Magnetic and centrifugal force in MRF process [88]

The centrifugal force ($F_{CEN}^{(r)}$) acting on a CIP at a distance r from the center of the tool is calculated as

$$F_{CEN}^{(r)} = (\rho_p(4\pi r_p^3)/3)((r_h - r)/(2r_p))((r_h + r)/2)\omega_T^2 \quad (1.4)$$

where ρ_p and r_p are the mass density and mean radius of the CIPs, respectively. ω_T = rotational speed of the wheel. The simplified form to calculate magnetic attraction force ($F_{MAG}^{(r)}$) between two CIPs is given as

$$F_{MAG}^{(r)} = \frac{3m\left(\left|\vec{H}(r)\right|\right)^2}{4\pi\mu_0\mu_1(2r^p)^4} \quad (1.5)$$

where μ_0 = permeability in free space, μ_1 = relative permeability, $\vec{H}(r)$ = magnetic field intensity, m = magnetic dipole moment.

A material removal model for MRF process is developed by Cheng et al. [32] . The model depends on normal pressure during finishing and carrier wheel velocity. The hydrodynamic pressure is more than magnetic pressure by six orders of magnitude. The material removal model proposed by them is based on Preston hypothesis and it is given as

$$\text{Material removal} = K\int PV\,\text{dt} \quad (1.6)$$

where K is a constant which depends on the workpiece material and the properties of MR fluid etc., P is the normal pressure and V is the velocity of the wheel (tool) with respect to the workpiece surface. However, the validation of their derived model does not match with their experimental results. Further, the results obtained from the Preston equation does not accurately give the output result as the equation only deals with the basic parameters i.e. pressure, velocity and time.

Miao et al. [89] modified Preston's coefficient for MRF process. Important parameters responsible for material removal i.e. hydrodynamic pressure, shear stress and a combination of the material figures of merit (FOM) in finishing process are considered. Experimental results for a

range of optical glasses are used for validation with the calculated model. Their predictive model is

$$MRR_{MRF} = C'_{(p,MRF(\tau,FOM))} E / (K_c H_V^2) \tau V \tag{1.7}$$

where $C'_{(p,MRF(\tau,FOM))}$ = modification of Preston's coefficient in terms of shear stress τ and material FOM, E = Young's modulus, K_c = fracture toughness of bulk material, H_V =Vicker's hardness of workpiece, V = wheel velocity.

Miao et al. [90] modified Eq. (1.7) to incorporate four process parameters i.e. nanodiamond concentration, penetration depth, magnetic field strength and relative velocity due to their removal contribution. The model is developed based on BK7 glass workpiece material although the model can also be applied to other glasses by altering mechanical FOM for that specific material.

Singh et al. [91] developed mathematical model for material removal and surface roughness considering magnetic field induced normal force as the process parameter for Ball end magnetorheological finishing process. The model is used to predict magnetic normal force. The model is validated experimentally at different working gaps. The % error between experimental and theoretical results varies in the range of 11.20% to 2.02%. For material removal they considered two body and three body wear mechanism. The magnetic flux density at different working gap is calculated as

$$B_z = \frac{NI}{(R_1 + R_2 + R_z + R_w + \frac{R_{air}}{2}) A_z} \tag{1.8}$$

where B_z is magnetic flux density, N is number of turns in the electromagnet coil, I = current, R = reluctance for different mean length of equivalent magnetic circuit of BEMRF setup, A_z = cross-sectional area of working gap. Calculation of average normal magnetic force, F_n with respect to variable working gap, is calculated as

$$F_n = P + A_z \tag{1.9}$$

where P = polishing pressure depending on the variation in magnetic flux density, B_z .

1.3.4.2 Force Analysis

The knowledge of finishing forces is necessary for polishing any surface to control the process efficiently. Shorey et al. [31] showed that material removal significantly depends on shear stress rather than hydrodynamic pressure. Also, they associated normal force and drag force with the Preston coefficient. They reported that the nonmagnetic abrasive particles are driven towards the workpiece surface due to magnetic field gradient. They proved this phenomenon by measuring drag force and atomic force microscope scan. The material removal rate increases with the addition of abrasive particles. It is hypothesized that due to the addition of abrasive particles wear mechanism changed to three body wear mechanism from two body wear mechanism. A reduction in total drag force is observed with the increase in abrasive particle concentration.

Kim et al. [79] found that levitation force also contributed to the material removal process by pushing the abrasive particles into the workpiece surface. Magnetic levitation force depends upon the volume of nonmagnetic body, intensity of magnetization and magnetic field gradient.

DeGroote et al. [87] found that with the increase in nanodiamond concentration, the drag force/shear stress increases however with further addition in nanodiamond abrasive particles there is no increase in peak removal rate. It is also reported that with different glass materials the drag force required for material removal changes.

Schinhaerl et al. [92] measured normal force in between workpiece surface and the finishing tool using a three-axis dynamometer for BK7 glass workpiece at different process parameters such as wheel speed, inductor current (magnetic field strength), pump speed (fluid flow rate) and immersion depth. The normal force primarily depends on immersion depth. They measured maximum normal force of 20 N.

Miao et al. [89] measured normal force and drag force simultaneously using dual force sensor. They found that the measured normal force is dependent on material hardness. Their study also demonstrates that shear stress dominates the material removal more than the drag force. It has been also reported that shear stress should be kept above certain critical value to remove material.

Miao et al. [90] reported that shear stress does not depend on the nanodiamond concentration, penetration depth, magnetic field strength and relative velocity between the workpiece and the rotating MR fluid ribbon. Instead, it depends mainly on the mechanical properties of the material. Also, they reported that both drag force and normal force increase with the addition of nanodiamond particles and become steady with higher nanodiamond concentration.

Sidpara and Jain [93] carried out an experimental investigation to measure the normal and tangential forces on the workpiece surface. For this study, four parameters are selected i.e. volume concentrations of CIPs, volume concentration of abrasive particles, working gap and wheel speed. Among all parameters, working gap and volume concentration of CIPs affect most significantly on the forces. Normal and tangential forces decrease with increasing working gap while these forces increase with increasing CIP concentration. Both normal and tangential forces decrease beyond 3.5% abrasive concentration.

Sidpara and Jain [94] conducted a theoretical study on normal, tangential and squeezing force acting on the workpiece surface. They developed a normal squeeze force model. The theoretical models are validated with the experimental results for different working gaps, CIPs and abrasive concentration and wheel speed. It is found that the theoretical normal and tangential force model matches well with the experimental results while considering squeeze force as compared to without squeeze force.

Singh et al. [95] developed a model of finishing force acting on workpiece surface. The finishing force developed due to the bonding strength of MR polishing fluid and rotation of the finishing tool. The finishing force is composed of normal force and shear force.

Sidpara and Jain [96] analyzed forces acting on the freeform surface by experimental as well as theoretical studies. They reported that mainly two type of forces, namely normal force and tangential force are involved during finishing. Normal force is applied on the abrasive particle through surrounding CIPs and this force is responsible for indentation on the workpiece surface. Tangential force generates due to the rotation of the finishing tool which helps in removing tiny chips from the workpiece surface. Components of normal force and tangential forces are taken into consideration in case of freeform surface due to the different angle of curvatures. Normal force includes magnetic levitation force and centrifugal force and on the other hand, tangential force includes shear force and Coriolis force. The process parameters considered in this study are angle

of curvature of the workpiece, tool rotational speed and feed rate. Both the magnitude of normal force and tangential force decrease with increasing angle of curvature however with the increase in tool rotational speed and workpiece feed rate these forces attain a maximum value and then decrease.

1.4 Scope and Objectives of the Present Work

Surface of a component plays important role for its performance and life. The motivation behind the development of magnetic field assisted finishing (MFAF) process is to fabricate a simple polishing set-up for super finishing of flat as well as freeform surfaces by using a rotating MFAF polishing tool to achieve precise automatized finishing at nanometer level. To explore MFAF process with the developed MFAF polishing tool following objectives are considered.

- To design and develop a polishing tool for MFAF process. Simulation study to optimize the dimension and design of the tool. Preliminary experimental study to analyze the capability of the developed tool to finish workpiece surface at nanometer level.
- To generate optimum toolpath for automatic control of MFAF process to finish flat and freeform surfaces.
- To synthesize MR fluid composition to obtain required surface finish and surface topography on the femoral component of knee implant made of Ti alloy.
- Characterization of the finished Ti alloy surface to explore MFAF tool capability to produce implant worthy surface. Optimization of the process parameters to achieve best surface roughness and surface topography required for femoral component of knee implant.
- Simulation and experimental investigation to explore finishing forces in MFAF process. Simulation of MFAF process to calculate the finishing forces. Statistical analysis to optimize process performance by controlling the finishing forces.
- Nanofinishing of femoral knee implant with the developed MFAF polishing tool. The capability of MFAF tool to finish complex freeform surface to be analyzed and explored. The key process parameters of the MFAF process to be optimized to achieve minimum surface roughness.
- The performance of MFAF finished surface to be analyzed with tribological study. A pin-on-disc tribometer is utilized to carry out wear tests.

1.5 Organization of the Thesis

The thesis is organized into seven chapters with references. The introduction to the finishing processes and related literature review is introduced in the **First chapter.** The literature review of different finishing processes for freeform surfaces is mentioned. Also, the advanced finishing processes and magnetic field assisted finishing processes are discussed along with previous studies on the processes reported by different researchers. The literature survey related to MR fluid, workpiece material in the present work, mathematical modelling and force analysis of magnetic field assisted finishing process is presented.

Design and development of MFAF polishing tool are discussed in **Chapter 2**. A simulation study is conducted to optimize the design and dimension of MFAF tool. A preliminary experimental study is also conducted to explore the capability of the MFAF tool to provide nanofinishing on Ti alloy surface.

In **Chapter 3**, composition of MR fluid and toolpath is optimized regarding Ti alloy and its application as femoral knee implant. Different methods are used to analyze surface roughness, surface topography and surface chemistry of the Ti alloy surface before and after finishing with MFAF polishing tool.

Surface characterization of the finished Ti alloy with 3D surface roughness parameters is discussed in **Chapter 4**. Central composite rotatable design (CCRD) of design of experiments (DOE) technique has been used to plan the experiments. Optimization of the process parameters of MFAF process is conducted to achieve necessary surface finish and surface topography for higher performance and longevity of femoral knee joint implant. Also, the effect of each process parameters on output responses are analyzed for better understanding of the finishing process. The finished surfaces are characterized by optical profilometer, field emission scanning electron microscope and atomic force microscope.

In **Chapter 5**, finishing forces involved in MFAF process are discussed. MFAF process is simulated to calculate the finishing forces. The simulation study is then corroborated with the validation experiments. A material removal model is also simulated to predict the material dislodgement in MFAF process. Statistical analysis is carried out to find out the process parameter significance and change in finishing forces due to the difference in process parameters.

In **Chapter 6,** developed MFAF tool is used to finish femoral knee implant. The ability of the MFAF tool to provide uniform finishing along the curvature of freeform surface of a femoral knee implant is analyzed with the help of surface topography and surface roughness. A statistical analysis for better understanding of the process mechanism and to increase the process performance is carried out. An optical profilometer is used to characterize surface roughness and surface topography on the component surface.

In **Chapter 7**, a tribological study is used to evaluate and compare the performance of MFAF finished surface with manually polished surface in respect to their application as femoral knee implant. The experimental results will help to understand in vivo performance of articulating surface of femoral knee implant finished using MFAF process. Pin-on-disc tribometer ascertains UHMWPE disc wear related to MFAF and manually finished Ti alloy grade 5 pin.

Discussion about the conclusions and findings of the present work with future scope is presented in **Chapter 8**. The references are added at the end.

Chapter 2 Design and Fabrication of Novel Polishing Tool

2.1 Introduction

During finishing of freeform surfaces, it is required that the MR fluid at the end of polishing tool should make a point contact with the workpiece surface. However, from literature survey, it is found that the uniform point contact finishing is very hard to achieve due to constraints related to the tool design and tool material while finishing freeform surfaces. To solve this particular problem, simulation and experimental studies are carried out to design and develop a novel polishing tool.

A novel tool is designed and developed for precision MFAF process to finish freeform surfaces. A finite element analysis (FEA) based commercial software package Ansoft Maxwell® is used to determine the optimum tool shape and its dimension. A permanent magnet is used to provide the magnetic field in the finishing zone. The dimension of the permanent magnet is also determined using the same software. Later, an experimental study is carried out to ascertain the capability of the developed tool. The tool is designed to finish freeform surfaces uniformly and precisely over the entire workpiece surface. The tool is attached to a four-axis CNC milling machine to impart a high degree of freedom for better finishing capability.

2.2 Design and Fabrication of Polishing Tool

The polishing tool consists of a permanent magnet and magnet holder. It is necessary to design an optimum tool to avail sufficient magnetic field in the finishing zone. Nd-Fe-B (Neodymium-Iron-Boron) of grade N48, a rare earth permanent magnet is considered. This magnet is selected due to its high magnetic strength. The optimum tool design for the MFAF process is carried out in two steps as discussed in the following subsections. In the 1st step, the dimension of the permanent magnet is determined and in the 2nd step, the dimension and geometry of the magnet fixture are determined.

2.2.1 Dimension of Permanent Magnet

To optimize the dimension of the permanent magnet, FEA simulation of the magnet is carried out. Cylindrical permanent magnet is considered for the current study to provide uniform polishing on the workpiece surface. The following assumptions are considered during FEA simulation:

- The solver computes static magnetic field
- All objects are stationary
- The source of the magnetic field is a permanent magnet

Different combinations of the magnet diameter and the height of the cylindrical magnet are considered during simulation. The simulation set-up for this analysis is shown in Fig. 2.1(a). In this study, the distance between the magnet and the workpiece is kept fixed as 1.5 mm which is filled with MR fluid. A line is drawn along the magnet axis from the magnet tip to the workpiece surface at A. From point A another line is drawn up to point B at the workpiece edge as shown in Fig. 2.1(a). After simulation, the magnetic field distribution is plotted from point B along line BA (Fig. 2.1(a)). The magnetic field distributions are analyzed for all the probable designs which makes the basis for choosing optimum dimension of the magnet.

A parametric study is carried out to optimize the dimension of the permanent magnet during simulation. The two main features of the magnet dimensions, i.e. diameter and height of the magnet are considered. During simulation one parameter is kept constant while the other one is varied. Range of the diameter and height of the cylindrical magnet are varied between 5 to 20 mm and 50 to 100 mm, respectively.

While determining the magnet height, diameter of the magnet is kept constant at 10 mm. The simulated results of distribution of magnetic flux density from point B along line BA (Fig. 2.1(a)) are shown in Fig. 2.1(b) for different magnet heights. From Fig. 2.1(b), it is observed that magnet height of different dimensions has an insignificant effect on magnetic flux density on the workpiece surface. Hence, the height of the magnet is chosen randomly as 70 mm.

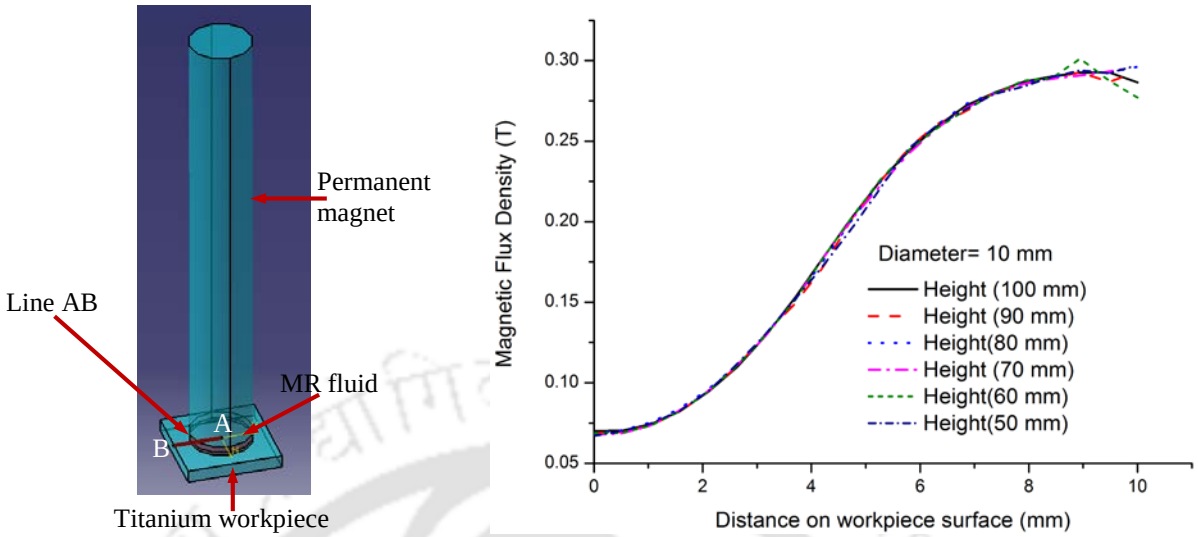

(a) (b)

Fig. 2.1 (a) Schematic diagram of the computational domain during magnetic field simulation of the polishing tool and (b) distribution of magnetic flux density on workpiece surface along line BA for different magnet heights

After that, the diameter of magnet is determined by keeping magnet height fixed at 70 mm. Further, magnetic field distribution is simulated at different magnet diameter from 5 to 20 mm and is plotted in Fig. 2.2 from point A along line AB. From the magnetic field distribution shown in Fig. 2.2, it is observed that the magnetic flux density generated from the 5 mm diameter magnet is non-uniform. Also, 20 mm diameter magnet produces very less magnetic flux density on the workpiece surface unlike other magnets. Hence, magnets with diameters 10 & 15 mm are selected as they produce moderate magnetic flux density on the workpiece surface which is sufficient for the purpose of finishing as per literature [39]. Maximum magnetic flux density is observed at the center of the workpiece at point A and its magnitude decreases towards the farthest corner (point B) due to the edge effect. Magnetic field contour plot for both 10 and 15 mm diameter magnets are plotted in Figs. 2.3(a) & (b), respectively.

2.3 Shape and Dimension of Magnet Holder

Ansoft Maxwell® is used to design the magnet fixture for holding the permanent magnet in its required position. At first, magnetic field distribution of a cylindrical permanent magnet is analyzed as given in Figs. 2.3 (a) & (b). After that, based on the distribution of the magnetic field as shown in Fig. 2.3, various probable configurations of the magnet fixtures are considered. Later, these configurations are simulated using Ansoft Maxwell® software to find out its optimum design

configuration after analyzing their magnetic field contour plots. The main objectives considered during designing of the magnet fixture are as follows:

- The magnet fixture should encompass the permanent magnet firmly.
- It should direct the magnetic flux lines in such a way that it should concentrate in the finishing zone avoiding its diversion away from the finishing zone.
- The fixture should shield the magnetic field from outside environment so that MR fluid as well as any surrounding magnetic materials do not stick to the magnet fixture.

High permeable magnetic materials are generally used for magnetic shielding. The most common material used for magnetic shielding is mu-metal which is a nickel-iron based alloy. In the present study, mu-metal is used as the magnet fixture material.

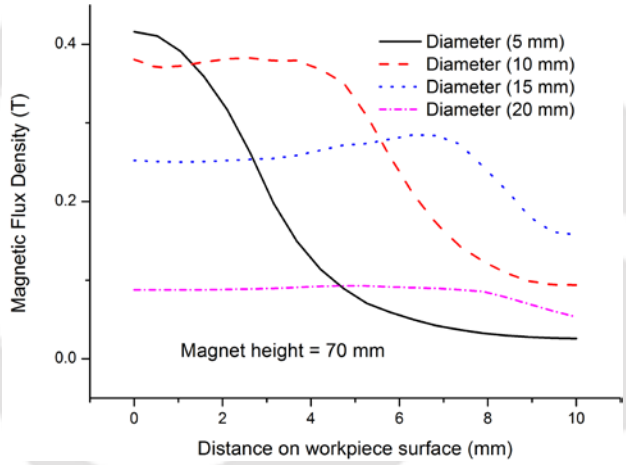

Fig. 2.2 Magnetic flux density plot along the line AB on the workpiece surface for different diameters of the magnet

To determine the maximum diameter and length of the magnet fixture, horizontal lines are drawn at different cross sections in the contour plot as shown in Fig. 2.3. The lines are drawn to find out the substantial amount of magnetic flux density around the magnet. After simulating possible lengths of each line, it is found that at the two pole tips and in the middle of the cross-section of the magnet, the lengths of these lines are 20 mm and 15 mm, respectively for 10 mm diameter magnet. For 15 mm diameter magnet, these values are 25 and 20 mm, respectively. These lengths are considered as the diameter of the magnet fixture in those particular cross-sections which encompasses most of the magnetic field lines.

To design the shape of the magnet fixture enclosing and holding the magnet during finishing, different configurations of the magnet holder are considered. The idea of different shapes is conceived from the contour plot of the magnetic flux distribution of a single cylindrical magnet (Fig. 2.3) so that all the substantial magnetic field lines can be enclosed and manipulated towards a certain direction. The initial dimension of the magnet fixture is taken from the previous simulation study as discussed in the previous paragraph. The objectives of the present study are

- To find out the optimum shape of the magnet fixture which will produce maximum possible magnetic field on the workpiece surface.
- To generate a circular magnetic field distribution for getting spherical / ball shaped MR fluid in the finishing zone so that point contact during finishing can be achieved.

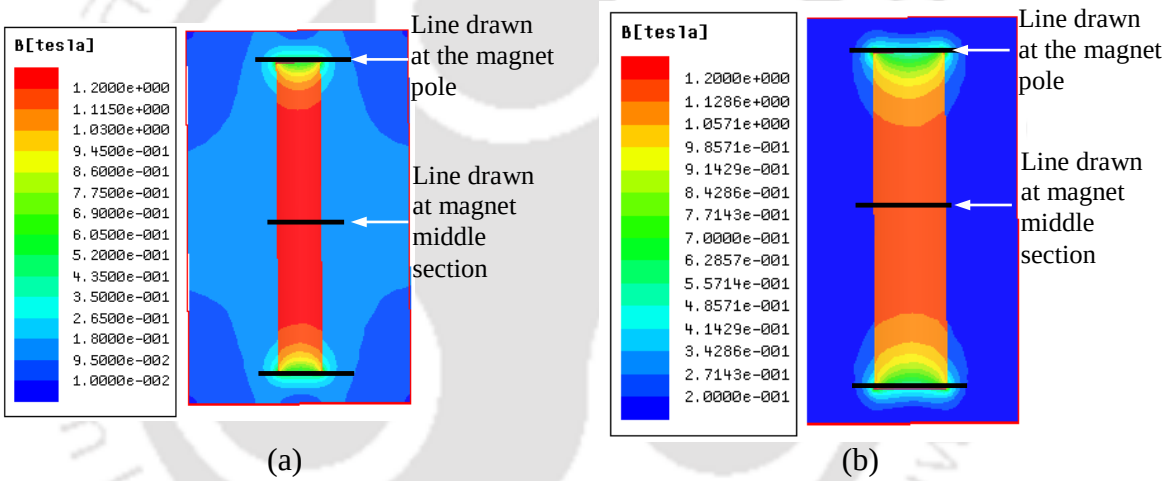

(a) (b)

Fig. 2.3 Magnetic flux density contour plot of a 70 mm height permanent magnet having diameter (a) 10 mm and (b) 15 mm

The magnetic flux density on the workpiece surface and the shape of the magnetic field lines at the bottom of the magnet pole for different configurations of the magnet fixtures are simulated to select its optimum configuration. Ansoft Maxwell® is used to find out the shape of the magnetic flux distribution in the finishing zone so that the shape of MR fluid in the finishing zone can be anticipated since the carbonyl iron particles (CIPs) in MR fluid line up along the magnetic field lines. During simulation, the diameter and height of the permanent magnet are considered as 10 mm and 70 mm, respectively. The working gap between titanium workpiece and permanent magnet is kept as 1.5 mm which is filled with MR fluid.

The design of the 1st configuration of the magnet fixture is shown in Fig. 2.4(a). Figure 2.4(b) shows the contour plot of magnetic flux distribution in the finishing zone which is ellipsoid

in shape instead of required spherical one. The magnetic flux distribution on the workpiece surface from point A along line AB (Fig. 2.1(a)) for the above shape is shown in Fig. 2.5. The magnitude of the simulated magnetic field along line AB on the workpiece surface suggests that finishing is possible [39]. However, this configuration will not serve the required purpose as a polishing tool due to the ellipsoid shape of the magnetic flux distribution at the pole tip. Hence, it is discarded.

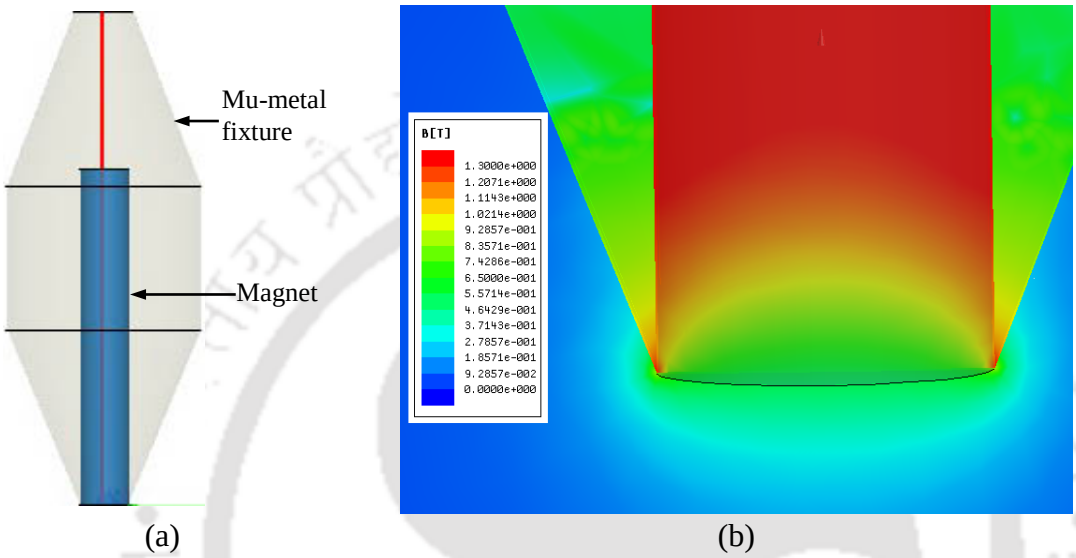

(a) (b)

Fig. 2.4 (a) Shape of the 1st configuration of the magnet fixture and (b) simulated magnetic flux distribution contour plot in the finishing zone

Fig. 2.5 Distribution of magnetic flux density along line AB (Fig. 2.1(a)) for 1st configuration on workpiece surface

The design of the magnet fixture considered for the 2nd configuration is shown in Fig. 2.6(a). Figure 2.6(b) shows the contour plot of magnetic flux distribution which provides a good spherical shape in the finishing zone better than the previous configuration. Figure 2.7 shows the magnetic flux density on the workpiece surface. The magnitude of the simulated magnetic field

from point A along line AB on the workpiece surface suggests that finishing is possible [39]. However, the main drawback of this configuration is that the available magnetic flux density on the workpiece surface is lesser than the previous configuration (Fig. 2.5). Hence, this configuration is also discarded.

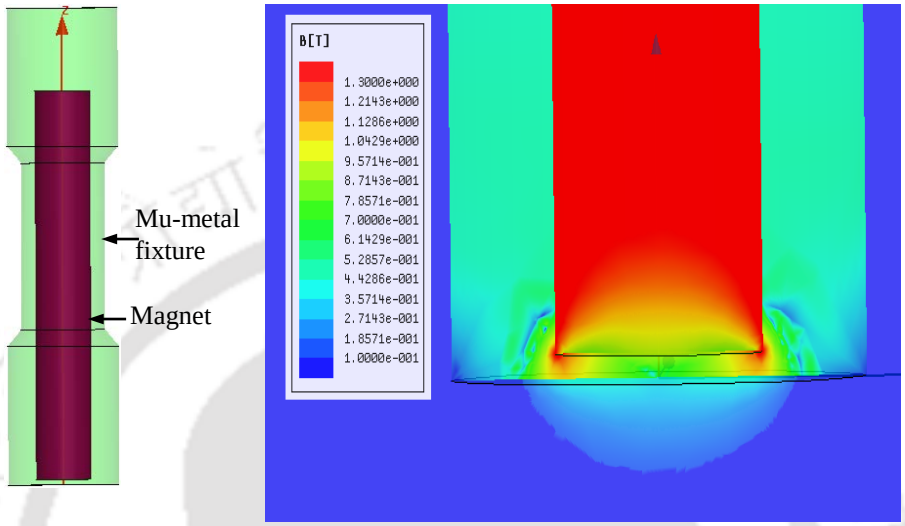

(a) (b)

Fig. 2.6 (a) Shape of the 2nd configuration of the magnet fixture and (b) simulated magnetic flux distribution contour plot in the finishing zone

Fig. 2.7 Distribution of magnetic flux density along line AB for 2nd configuration on workpiece surface

Figure 2.8(a) shows the design of the magnet fixture for 3rd configuration. Figure 2.8(b) shows the contour plot of the magnetic flux distribution. A good spherical shape is formed in the finishing zone for this configuration. The magnitude of the simulated magnetic flux density from point A along line AB on the workpiece surface is shown in Fig. 2.9 which is similar to the 1st configuration (Fig. 2.5) and it is sufficient to carry out finishing operation [39]. Hence, this configuration can be considered for polishing tool design.

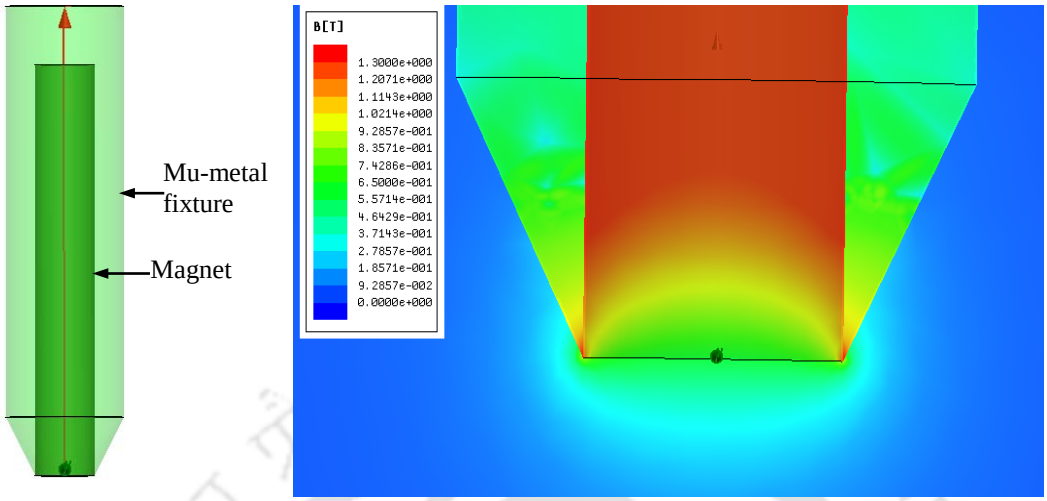

(a) (b)

Fig. 2.8 (a) Shape of the 3rd configuration of the magnet fixture and (b) simulated magnetic flux distribution contour plot in the finishing zone

Fig. 2.9 Distribution of magnetic flux density along line AB (Fig. 2.1(a)) for 3rd configuration on workpiece surface

To explore further, another design (4th configuration) is considered (Fig. 2.10(a)). The difference between 3rd and 4th configurations is the end-shape of the magnet fixture which is spherical in the latter configuration. As shown in Fig. 2.10(b), the contour plot of the magnetic flux distribution in the finishing zone is spherical. The magnitude of the simulated magnetic flux density on the workpiece surface from point A along line AB is shown in Fig. 2.11 and its magnitude is higher than all other previous configurations. Hence, the 4th configuration of the magnet fixture is selected in the present study after exploring all four fixture configurations. The 4th configuration of the magnet fixture can achieve finishing spot at a point on any kind of freeform

surfaces. The maximum available magnetic flux density on the workpiece surface during the simulation study is 0.4 Tesla.

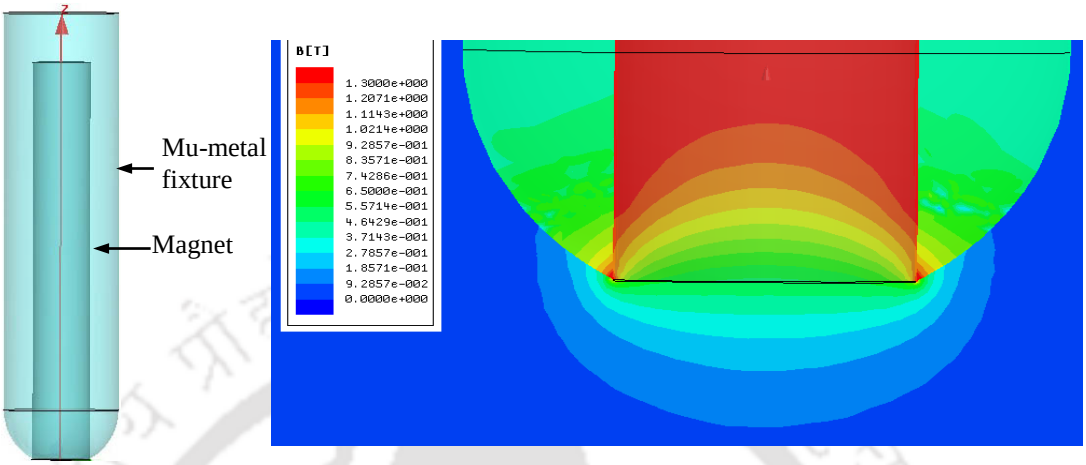

(a) (b)

Fig. 2.10 (a) Shape of the 4th configuration of the magnet fixture and (b) simulated magnetic flux distribution contour plot in the finishing zone

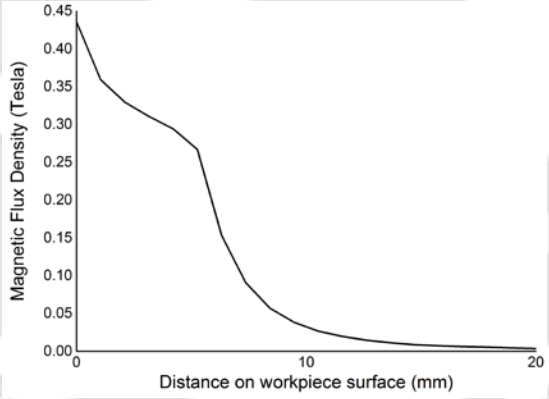

Fig. 2.11 Distribution of magnetic flux density along line AB (Fig. 2.1(a)) for 4th configuration on workpiece surface

2.4 Experimentation

A magnet fixture is fabricated based on optimum design configuration (4th configuration, Fig. 2.10(a)) as shown in Fig. 2.12. The mu-metal magnet holder along with permanent magnet is attached to a milling machine. The working gap between the tool and the workpiece is kept as 1.5 mm. The magnetic field intensity is measured at different points on the workpiece surface (A-at the center of the workpiece along the axis of the magnet fixture, B-below the edge of the magnet fixture on workpiece surface and C-at the workpiece edge as shown in Fig. 2.12) using digital Gaussmeter. Aluminium is considered as workpiece material during magnetic field measurement

and during simulation. The experimentally measured magnetic field at those points are compared with the simulated results.

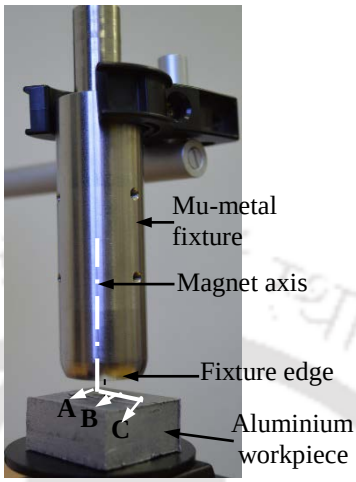

Fig. 2.12 Magnet holder along with aluminium workpiece showing magntic field measurement positions

The experimental setup is shown in Fig. 2.13. The developed novel polishing tool is attached to a 4-axis CNC milling machine head. The mu-metal tool is holding a cylindrical permanent magnet (Nd-Fe-B of grade N48) of dimension 15×70 mm. Coercive force (Hc) and relative permeability of the permanent magnet is 10.5 kOe and 1.33, respectively. A precision vice is used to hold the workpiece during finishing as shown in Fig. 2.13(a).

At first, the magnetorheological (MR) polishing fluid is prepared by mixing 40 Vol.% of carbonyl iron particles (CIPs) of EN grade from BASF, Germany and 3.5 Vol.% of diamond abrasive particles (diameter 6 μm) in a base medium (56.5 Vol.%) of hydrofluoric acid (HF), nitric acid (HNO_3) and distilled water [97]. To make the finishing process automated, a CNC tool path is generated to guide the tool during finishing. The experimental conditions during finishing are provided in Table 2.1. The surface roughness of the workpiece is measured with the help of a non-contact type optical profilometer (Taylor Hobson Talysurf) before and after experiments. Also, the surface topography of the workpiece surface before and after experiment is inspected using profilometer and atomic force microscope (AFM).

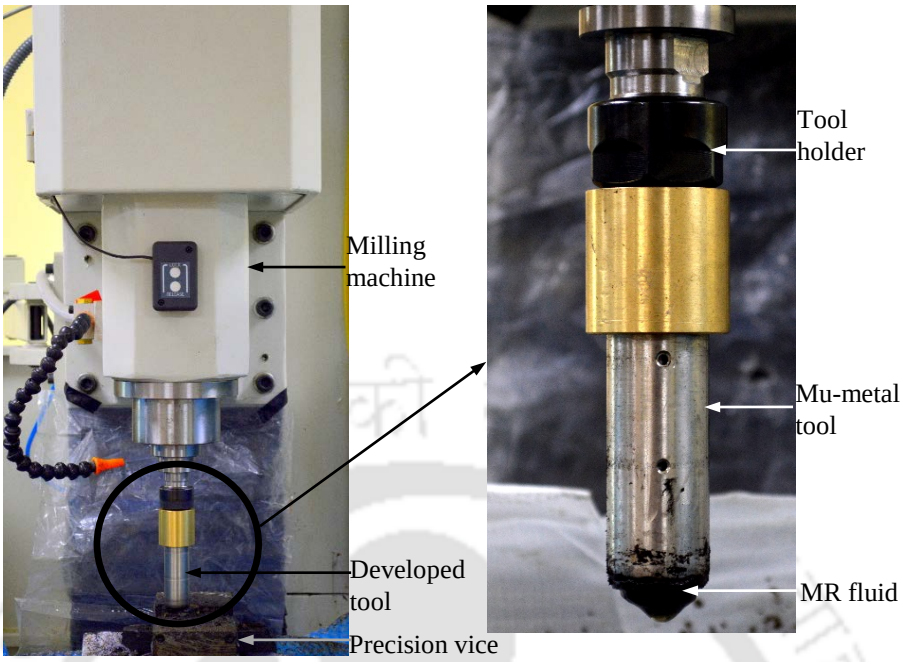

Fig. 2.13 (a) MFAF experimental setup and (b) developed novel polishing tool

Table 2.1 Experimental conditions during MFAF

Parameter	**Conditions**
Rotational speed of the tool	1200 rpm
Working gap between tool and workpiece	0.8 mm
Finishing time	6 hrs. 30 min

2.5 Results and Discussion

Table 2.2 shows the experimentally measured and simulated magnetic flux density at different points on the workpiece surface which shows a close agreement between these values. Hence, the simulated results can be utilized to design polishing tool for this particular setup. The small difference between the simulated and experimental results may be due to the effect of surrounding environment. During simulation, the surrounding environment is considered as vacuum, however, during experiment the polishing tool is surrounded by magnetic materials in the milling machine which may affect the measured magnetic field.

Table 2.2 Measured and simulated magnetic flux density at points A, B and C (Fig. 2.12)

Measured points	Magnetic Flux Density (T)	
	From simulation	Experimentally measured
A	0.10	0.10
B	0.40	0.30
C	0.04	0.01

The initial surface roughness of the titanium workpiece is 180 nm. After finishing using the polishing tool the measured surface roughness of the titanium workpiece surface is 10 nm. The percentage change in surface roughness (%Δ Ra) is 94.44%. Figure 2.14(a) shows the initial surface roughness profile and Fig. 2.14(b) shows the initial surface topography of the titanium workpiece which shows that there are deep scratch marks. Figure 2.16(a) shows the initial AFM surface topography of the titanium workpiece which shows surface undulations on the workpiece surface. The peak to valley heights are high in the initial surface roughness profile (Fig. 2.14(a)). Also, in the AFM figure, deep valleys are visible (Fig. 2.16(a)). Figure 2.15(a) shows the final surface roughness profile and Fig. 2.15(b) shows the final surface topography of the polished titanium workpiece surface. Figure 2.16(b) shows the final AFM surface topography of the polished titanium workpiece surface. After finishing by MFAF process, very smooth mirror like surface is achieved as shown in Fig. 2.15(b) and Fig. 2.16(b) where the peak to valley heights are reduced extensively. Figure 2.15(b) shows small peaks and valleys in the final surface instead of the scratch marks on the initial surface (Fig. 2.14(b)). Also, in the final AFM surface topography (Fig. 2.16(b)), the deep valleys are reduced.

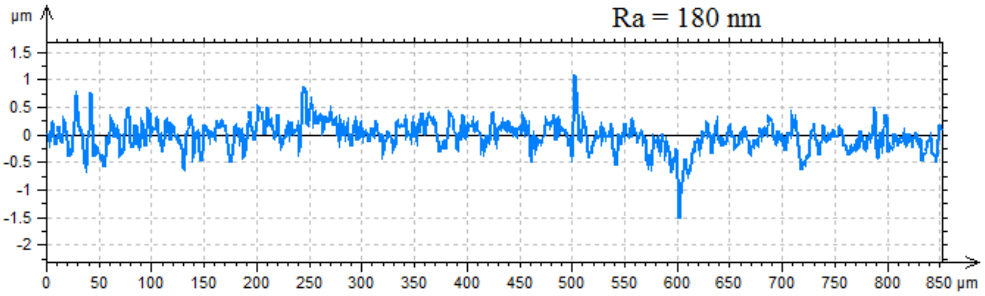

(a)

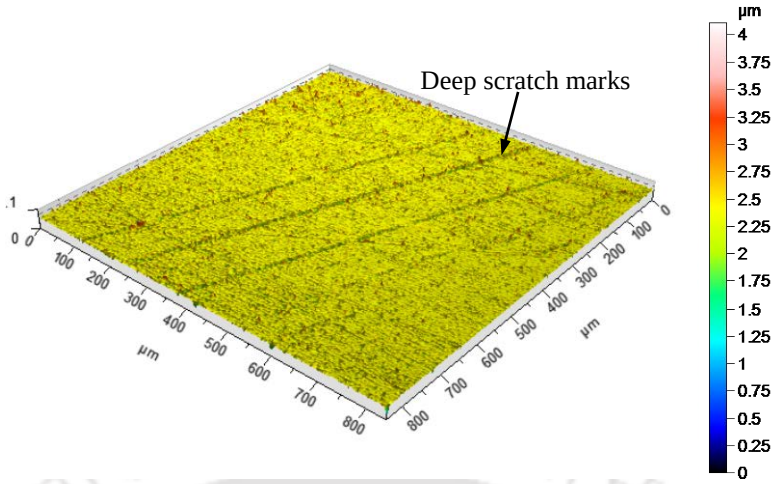

(b)

Fig. 2.14 Initial (a) surface roughness profile and (b) surface topography of titanium workpiece from optical profilometer

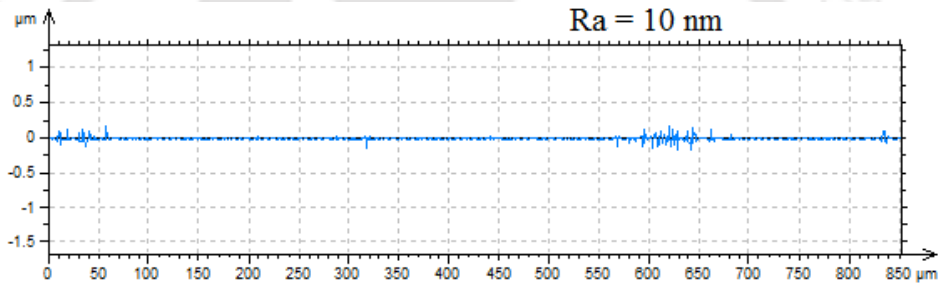

(a)

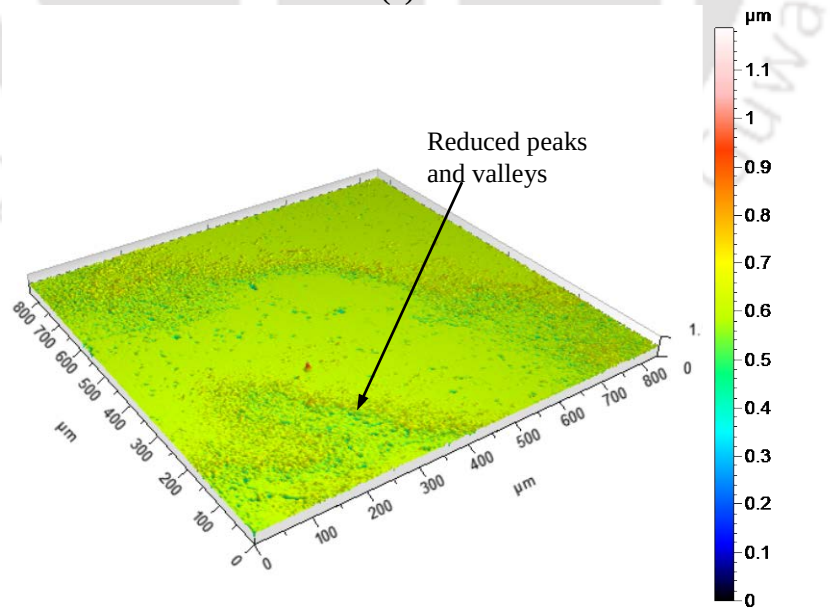

(b)

Fig. 2.15 Final (a) surface roughness profile and (b) surface topography of titanium workpiece from optical profilometer

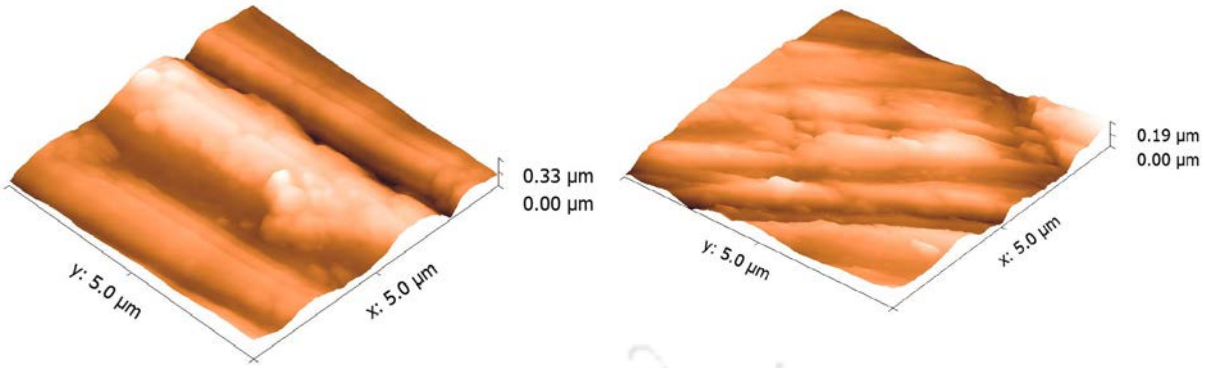

(a) (b)

Fig. 2.16 (a) Initial and (b) final surface topography of titanium workpiece after MFAF from atomic force microscope

2.6 Summary

A polishing tool is designed and developed in the current study to finish freeform surfaces. The tool consists of a permanent magnet and a magnet holder. Finite element analysis, using commercial software package, Ansoft Maxwell® is used for the simulation study to find out the optimum design configuration and dimension of the tool for achieving better finishing characteristics. Mu-metal is chosen as a material for magnet holder due to its excellent magnetic field shielding property. The maximum achieved magnetic flux density on the workpiece surface is 0.4 Tesla which is sufficient enough to carry out the finishing process. Hence, the developed novel tool can be used as a polishing tool for MFAF process. Finishing experiments are carried out to find out the capability of the developed tool for MFAF process. The final surface roughness value obtained after finishing a titanium workpiece is 10 nm from its initial surface roughness value of 180 nm and the percentage change in surface roughness is very impressive (94.44%). The finishing results are very satisfactory and the developed MFAF process will be utilized to finish freeform biomedical components.

Chapter 3 MR fluid synthesis and toolpath generation

3.1 Introduction

In medical industry, commercially pure titanium and titanium alloys are used to make surgical implants due to its bio-compatibility. Titanium (Ti) alloys are generally referred to as bio-titanium alloy in many literatures due to its application in bio-medical industries and it is extensively used to make artificial knee joint, artificial hip joint, dental implants, bone plates etc. The performance of the implant largely depends upon its surface morphology. Two types of implant i.e. permanent and semi-permanent are largely used in human body. Also, there are some implants in which relative motion between two components occurs. Hip and knee implants are such type of implants where femoral component experiences relative motion due to the joint motion. Now depending upon different applications of the implant, the requirement for surface roughness and surface texture are also different. The attachment of the implant with the biological tissue and bone deeply depends on the surface roughness of the implant [98]. The surface of the permanent implant should be rougher than the surface of the semi-permanent implant and also than other implants such as femoral components of knee and hip implants etc. Also, the micro pits and scratch marks on the surface of the permanent implants promotes osseointegration i.e. interaction between bone and implant. Hence, in case of permanent implants, the required surface roughness is higher than the other type of implants.

Surface wettability is another important criterion for implant performance. The biological response around the implant is not only affected by surface roughness and surface texture but also wettability of surface plays an important role [99]. Depending upon the implant application, requirement of surface wettability changes. Contact angle between liquid and solid surface is usually measured to study surface wettability. Small contact angle ($< 90^{o}$) means hydrophilic surface (high wettability) and large contact angle ($> 90^{o}$) implies hydrophobic surface (low wettability) [100]. Figure 3.1 shows the schematic diagram of contact angle between solid and liquid. Hydrophilic implant surfaces are prone to increased cell attachment than the hydrophobic

implant [101]. Hence, the surface of the permanent implants should be hydrophobic and the surface of the semi-permanent and other implants like femoral components of knee and hip implant should be hydrophilic in nature. Another important criterion of implant surface is its capability to enhance bio-activity. The formation of oxide layer on the implant surface has an important application. The oxide layer formation helps to limit the bacteria growth on the implant surface [98]. Also, it promotes bio-activity of the implant [62].

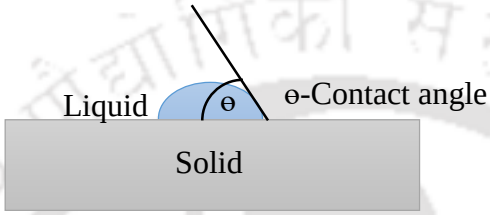

Fig. 3.1 Schematic diagram of contact angle between solid and liquid droplet

Different MR fluids are synthesized by changing MR fluid compositions for generating different surface morphology on the components surface while polishing of Ti alloy. The generated surface after finishing with different MR fluids are analyzed with different techniques to characterize surface morphology on the components surface. The surface roughness, surface topography, surface wettability and formation of oxide layer before and after finishing are studied.

Two different toolpaths are also generated to finish Ti alloy surface to select the optimum toolpath. The selection of optimum toolpath is based on the comparative study of the generated surface roughness and surface topography after finishing with both the toolpaths.

3.2 Experimental Investigation

Schematic diagram of MFAF tool is shown in Fig. 3.2(a). EN grade CIPs with mean diameter of 8 µm from BASF, Germany and diamond abrasive powder of size 6 µm is used to make the MR polishing fluid. Figures 3.2(b) and (c) show the field emission scanning electron microscope (FESEM) image of the CIPs (spherical shape) and diamond abrasive particles (random shape).

From preliminary experiments, it is found that only abrasive particle is not sufficient to finish titanium alloy. Hence, CIPs and diamond abrasive powder are dispersed in an acidic base medium. Specific composition of various acidic base medium is very important to generate

different surface morphology on the workpiece required in implants as discussed earlier. Hence, to efficiently finish the Ti alloy at the nanometer level, two types of acidic base medium are prepared.

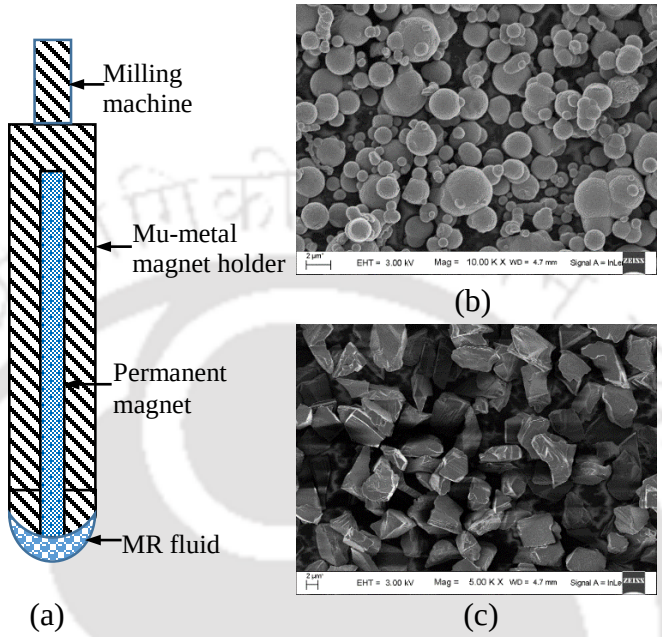

Fig. 3.2 (a) Schematic diagram of MFAF tool with attached MR fluid, (b) carbonyl iron particles of EN grade (BASF, Germany) at 1 kX magnification and (c) diamond abrasive particle of 6 µm size at 5 kX magnification

The first acid base medium comprises of hydrofluoric acid (HF), nitric acid (HNO_3) and deionized water. HF helps in softening the surface while HNO_3 helps to brighten the surface. The chemical reaction between titanium and acid base medium is shown in Eq. (3.1).

$$Ti+6HF+4HNO_3 \rightarrow H_2TiF_6+4NO_2+4H_2O \quad (3.1)$$

The chemical reaction generates hexafluorotitanic acid, nitrogen oxide and water. Hence, HF becomes stable during finishing. Hydrogen (H_2) embrittlement of the workpiece is eliminated during finishing due to no generation of H_2 gas. The second acid base medium comprises of hydrogen peroxide (H_2O_2) in deionized water. H_2O_2 helps the abrasive particles during finishing by dissolving the metallic surface of the workpiece. The respective chemical reaction is shown in Eq. (3.2).

$$Ti+2H_2O_2 \rightarrow TiO_2+2H_2O \quad (3.2)$$

The chemical reaction generates titanium dioxide which helps in promoting oxide layer during finishing. Glycerol is added to both of the fluids to increase MR fluid viscosity. It acts as a stabilizer which helps to disperse CIPs uniformly avoiding agglomeration. It also helps to prevent sedimentation. Deionized water is used instead of distilled water to prevent corrosion in the MR polishing fluid. A laboratory stirrer is used to prepare MR fluid by mixing CIPs and diamond abrasive particles in the base medium. MR fluid of Type – I is prepared with CIPs and abrasive particles in base medium of HF, HNO_3 and deionized water. MR fluid of Type – II is prepared with CIPs and abrasive particles in base medium of H_2O_2 and deionized water. The concentration of each constituent in MR fluid is given in Table 3.1 for both the fluid.

Table 3.1 Composition of MR fluid of Type - I & Type – II

Constituents of MR fluid	**Vol. concentration (%)**	
	Type - I	**Type - II**
CIP	40	40
Diamond abrasive	7.1	7.1
Glycerol	8	8
Hydrofluoric acid (HF)	1.17	----
Nitric acid (HNO_3)	2.33	----
Hydrogen peroxide (H_2O_2)	----	1.3
Deionized water	41.1	43.6

The experimental conditions such as tool rpm, polishing load, finishing time and working gap are provided in Table 3.2 and are kept same for all the experiments. The polishing load is measured using piezoelectric based dynamometer during finishing and is discussed in details in Chapter 5. The rpm of the tool is set using CNC milling machine.

Table 3.2 Experimental process parameters and their values

Process parameters (unit)	**Value**
Rotational speed of the tool (rpm)	1200
Working gap between tool and workpiece (mm)	1
Finishing time (hours)	6 hrs. 30 min
Polishing load (N)	1.02

To find optimum toolpath, MR fluid of Type-I is used as the polishing medium. The model of the titanium alloy workpiece is first generated in a CAD software. After that, the CAD model

is imported in a CAM based sprutcam® software where different types of toolpaths are generated according to the requirement. Two toolpaths i.e. spiral and parallel toolpath are considered to find out their effect on final surface roughness and surface texture.

Figure 3.3(a) shows the generated spiral toolpath. The MFAF tool follows the spiral toolpath and also rotates around its axis during finishing. Hence, the tool experiences only rotational motion during finishing process as shown in Fig. 3.3(b). Figure 3.4(a) shows the MFAF toolpath along with abrasive track. Figure 3.4(b) shows the abrasive particle motion due to the rotational motion of the tool along its axis for spiral toolpath. In this case, the abrasive particles experience centrifugal force (F_{cfg}) and also tangential force (F_t) as shown in Fig. 3.4(b).

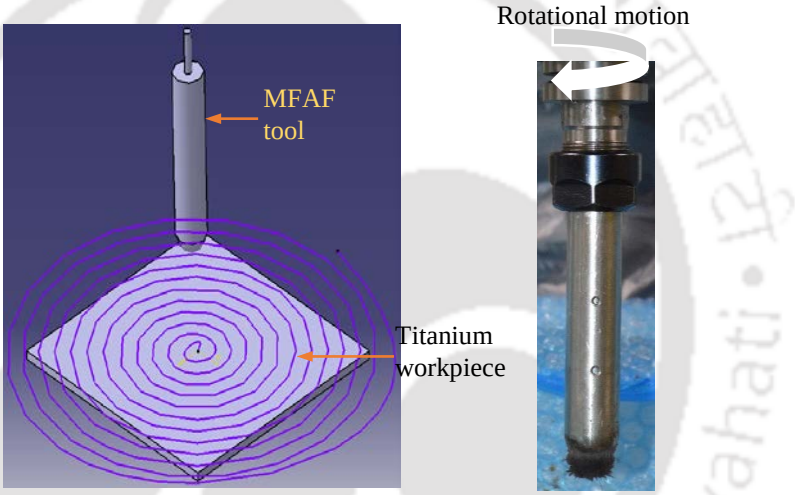

(a) (b)

Fig. 3.3 (a) Generated spiral toolpath and (b) tool motion during finishing process with spiral toolpath

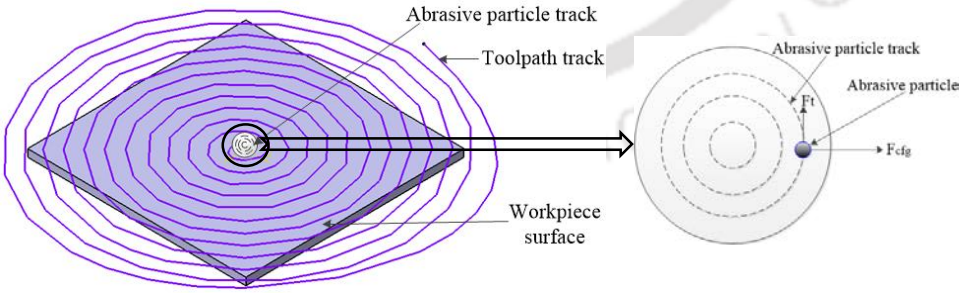

(a) (b)

Fig. 3.4 Pictorial depiction of (a) MFAF tool motion and (b) abrasive particle motion due to rotational motion of the tool along its axis on a spiral toolpath

Figure 3.5(a) shows the generated parallel toolpath along with the MFAF tool. The MFAF tool follows the parallel toolpath during finishing process. MFAF tool also rotates around its axis during finishing. Hence, the tool experiences both rotational motion and translational motion

during finishing as shown in Fig. 3.5(b). Figure 3.6(a) shows the MFAF toolpath along with abrasive track. Figure 3.6(b) shows the abrasive particle motion due to both rotational and translational motion of the tool during parallel toolpath. In parallel toolpath, abrasive particles experience feed force (F_f), centrifugal force (F_{cfg}) and tangential force (F_t) as shown in Fig. 3.6(b). A preliminary experimental study is carried out to explore the process and to identify the key process variables and the range of process variables.

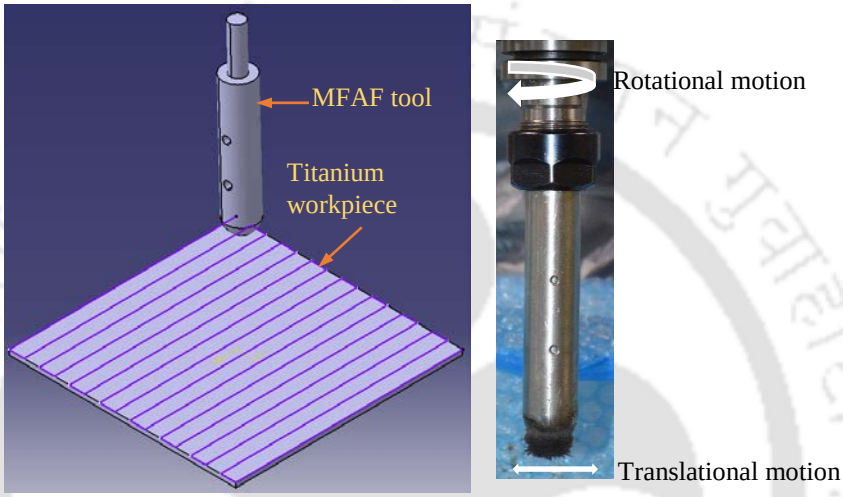

(a) (b)

Fig. 3.5 (a) Generated parallel toolpath and (b) tool motion during finishing process with parallel toolpath

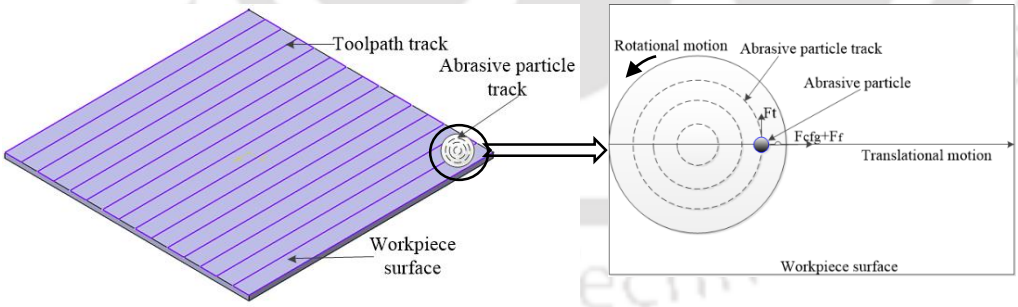

(a) (b)

Fig. 3.6 Pictorial depiction of (a) MFAF tool motion and (b) abrasive particle motion due to rotational motion of the tool along its axis and also translational motion of the tool for parallel toolpath

3.3 Results and Discussion

The effect of different MR fluid on surface roughness, surface topography and wettability is discussed and explored in this section. The formation of oxide layer during finishing is analyzed

using EDX. Also, to explore the effect of different toolpath the initial and finished surface roughness and surface topography of the Ti alloy is inspected. The wettability of the surface is inspected using sessile method of contact angle measurement using goniometer.

3.3.1 Effect of Different MR Fluid on Surface Roughness and Surface Topography

Both surface roughness and surface topography are very important parameters in case of implant materials. Implant performance and life mostly depend upon the implant surface morphology. Now, after finishing titanium with two types of MR fluid different surface roughness and surface topography are achieved. As stated earlier, permanent and semi-permanent implants require different type of surface finish as well as surface topography. Also, if implant performance includes relative motion such as femoral knee implant the requirement of surface roughness and surface topography is same as semi-permanent implant. The effect of both type of MR fluid on surface roughness and surface topography is discussed below.

3.3.1.1 MR Fluid of Type - I

Figures 3.7(a) and (b) show surface topography of titanium workpiece before and after finishing with MR fluid of Type – I. As shown in Fig. 3.7(a), the initial surface shows deep valleys, pits along with scratch marks. In the final surface topography (Fig. 3.7(b)), the surface becomes smoother and fewer deep valleys are present than the initial surface.

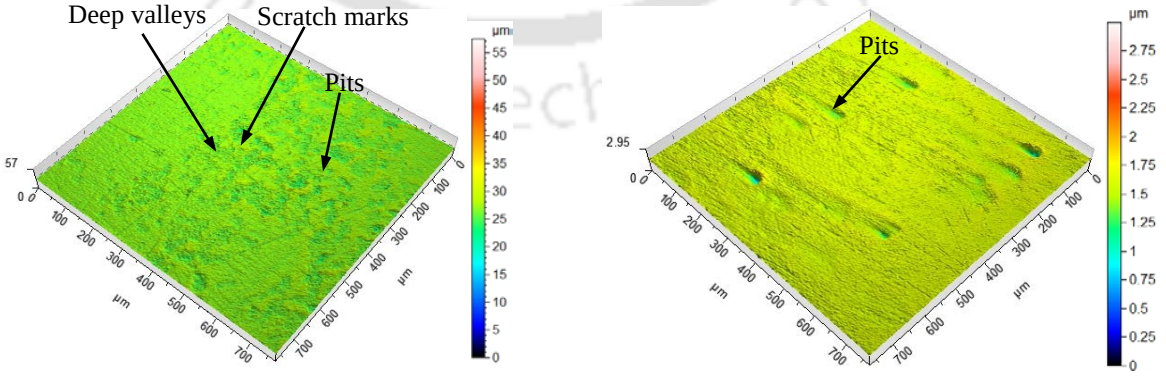

(a) (b)

Fig. 3.7 3D surface topography of Ti alloy workpiece surface (a) before and (b) after polishing with MR fluid of type – I

Figures 3.8(a) and (b) show the surface roughness profiles before and after finishing, respectively. The final surface roughness is reduced to 10 nm from its initial value of 560 nm having very high percentage improvement in the surface roughness of 98.21%. The percentage change in surface roughness is calculated as %ΔRa = (initial Ra – final Ra) ×100 / initial Ra. Figures 3.9(a) and (b) show the FESEM images of initial and final surfaces of the workpiece at 1000X magnification. Figure 3.9(a) shows that the initial surface is riddled with scratch marks. However, the final surface (Fig. 3.9(b)) shows a smoother surface with very less amount of remaining scratch marks. The obtained surface roughness (10 nm) is very impressive and it is as par requirement of the implant surface roughness of semi-permanent implant material according to ISO 7207-2:2011 [102]. The surface roughness of the finished component is very low (10 nm) and mirror finished surface is achieved with a lower number of micro-pits than the initial surface. According to the literature survey, these type of surface is not good for osseointegration. As osseointegration is a very important in vivo criteria for the permanent implants in human body [104]. Hence, MR fluid of Type – I is not a proper combination of acidic polishing medium with regards to osseointegration for permanent implants. It is better suited for finishing semi-permanent implant and femoral components of knee and hip prosthetics.

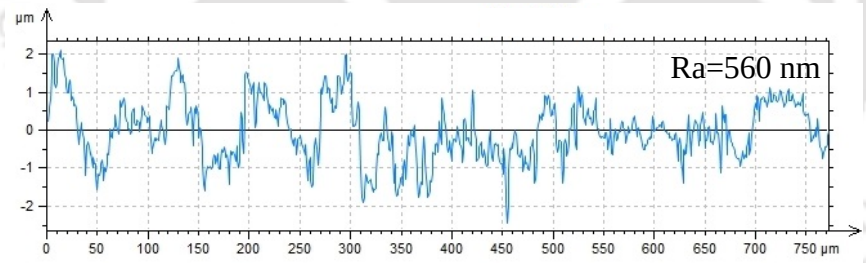

(a)

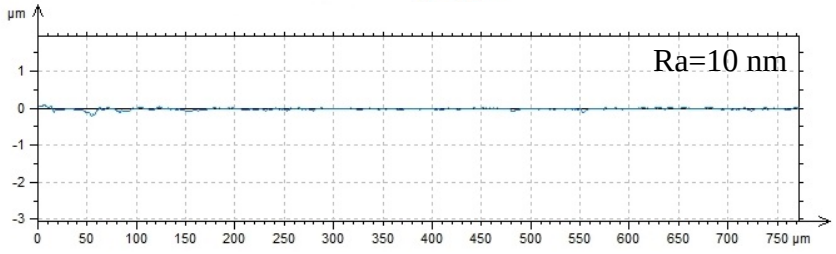

(b)

Fig. 3.8 2D surface roughness profile of Ti alloy workpiece surface (a) before and (b) after polishing with MR fluid of type – I

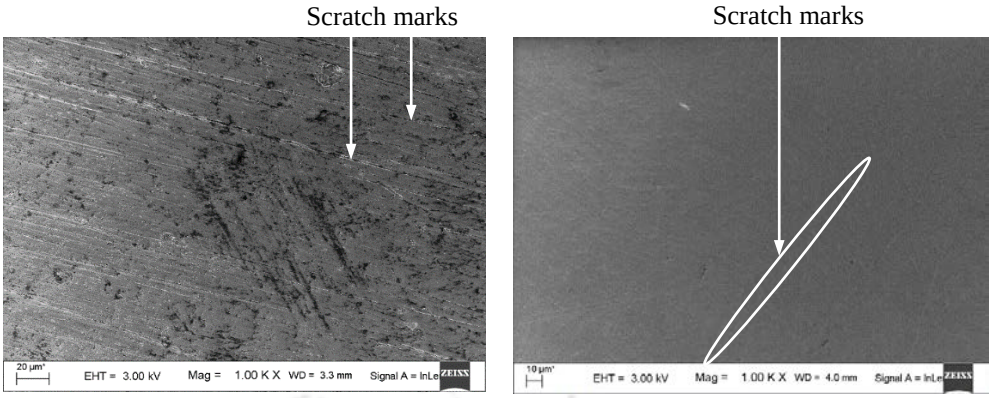

(a) (b)

Fig. 3.9 FESEM images of Ti alloy workpiece surface (a) before and (b) after polishing with MR fluid of type – I

3.3.1.2 MR Fluid of Type - II

Figures 3.10(a) and (b) show the workpiece surface topography before and after finishing, respectively with MR fluid of Type – II. As shown in Fig. 3.10(a), the initial surface shows deep valleys and deep scratch marks. In the final surface topography (Fig. 3.10(b)) scratch marks and the presence of deep valleys are reduced. Figures 3.11(a) and (b) show the surface roughness profile of initial and final surfaces, respectively. The initial surface roughness of 640 nm is reduced to 70 nm in the finished workpiece having percentage improvement in surface roughness of 89.06%. Figures 3.12(a) and (b) shows the FESEM images of initial and final surfaces, respectively at 1000X magnification. The initial surface is riddled with scratch marks as shown in Fig. 3.12(a). Final surface (Fig. 3.12(b)) has some scratch marks although it is reduced than the initial surface. The obtained surface roughness (70 nm) is good however it is higher than the Ti alloy workpiece finished with MR fluid Type – I. In case of permanent implants, the required surface roughness is higher than the other type of implants. Hence, the higher surface roughness is better in this particular case. The achieved surface topography with micro-pits and matte finish is good for osseointegration according to the literature [104]. Hence, MR fluid of Type – II is better suited to finish permanent implants.

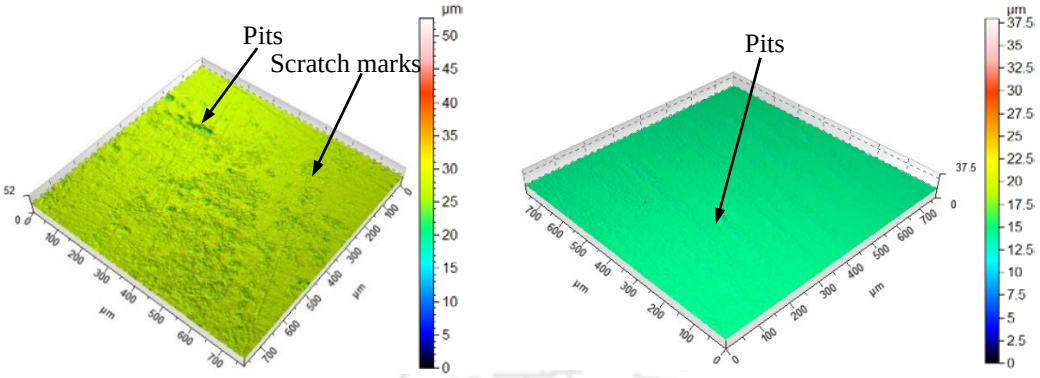

(a) (b)

Fig. 3.10 3D surface topography of Ti alloy workpiece surface (a) before and (b) after polishing with MR fluid of type – II

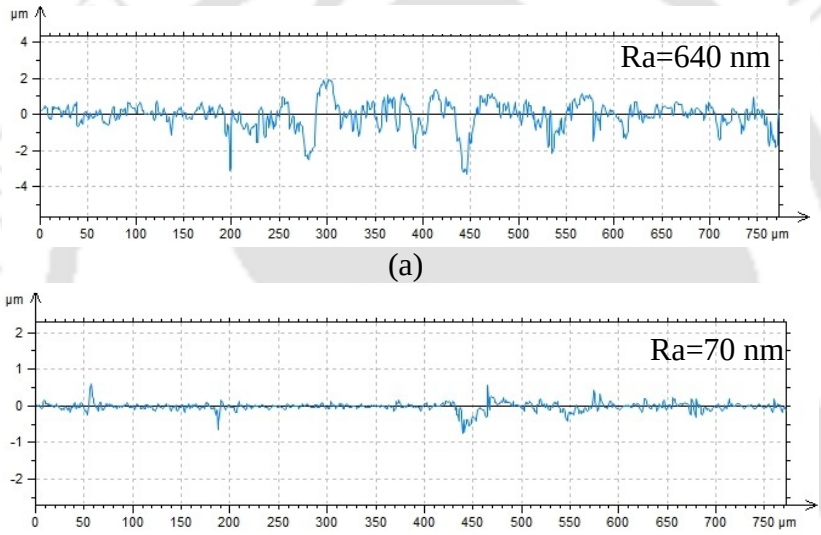

(a)

(b)

Fig. 3.11 2D surface roughness profile of Ti alloy workpiece surface (a) before and (b) after polishing with MR fluid of type – II

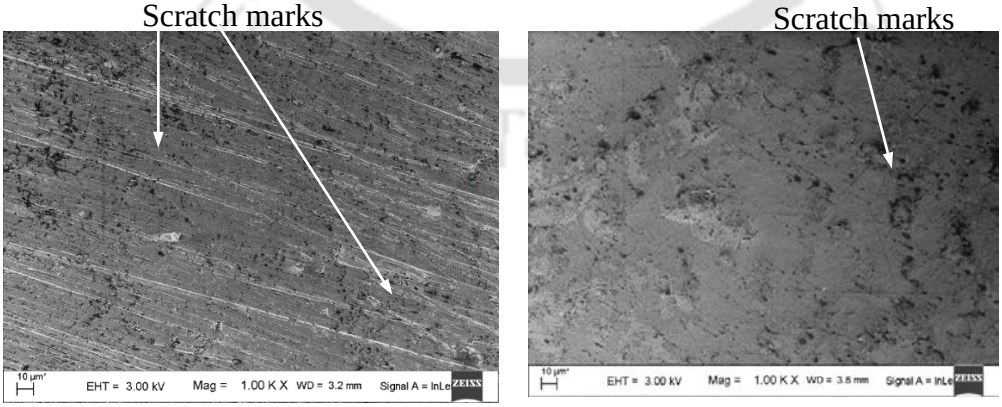

(a) (b)

Fig. 3.12 FESEM images of Ti alloy workpiece surface (a) before and (b) after polishing with MR fluid of type – II

3.3.2 Effect of Different MR Fluid on Wettability of Workpiece

Contact angle measurement is carried out to find out the wettability of finished surface. Figure 3.13(a) shows the contact angle measurement on the initial surface. As shown in the Fig. 3.13(a), the measured contact angle is 85.7° which is less than 90°. Hence, the initial surface is hydrophilic in nature. Figure 3.13(b) shows that the contact angle measurement on the final surface after finishing with MR fluid of Type – I. The measured contact angle is 77.5° which is less than 90° and it proves that the surface finished with MR fluid of Type – I is hydrophilic in nature. Figure 3.13(c) shows the measured contact angle on the final surface after finishing with MR fluid of Type – II. The measured contact angle is 98.1° which is more than 90° and it proves that the surface finished using MR fluid of Type – II is hydrophobic in nature.

(a)

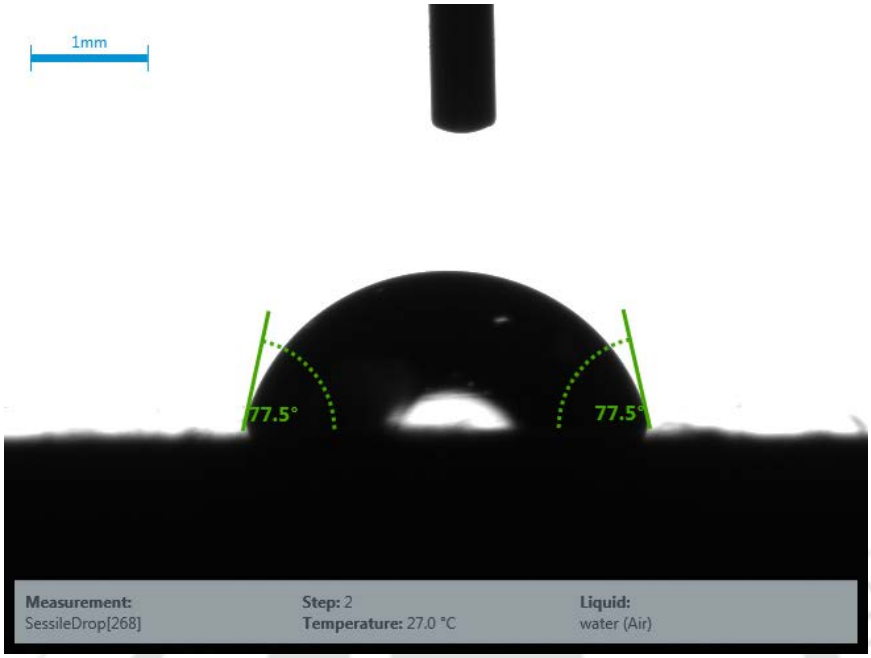

(b)

(c)

Fig. 3.13 Contact angles formed by sessile liquid drop on workpiece surface (a) before finishing; workpiece surface after finishing by MR fluid of (b) Type I and (c) Type II

The contact angle measurement study reveals that after finishing with MR fluid of Type – I the obtained surface is hydrophilic in nature. However, after finishing with MR fluid of Type – II, the obtained surface is hydrophobic in nature. According to literature survey [105], hydrophobic surface is prone to better osseointegration than hydrophilic surface. Hence, from wettability study

it can be concluded that MR fluid of Type – I is better suited to finish semi-permanent implants while for finishing permanent implant MR fluid of Type – II is a better choice.

3.3.3 Formation of Oxide Layer on Workpiece Surface

The composition of the Ti alloy is analyzed using EDX before and after finishing (Fig. 3.14). The weight percentage of titanium in the initial workpiece (Fig. 3.14(a)) is 77.7% making it the primary element. The percentage of oxygen is zero implying that there is no oxide layer on the surface. After finishing with MR fluid of Type – I, the workpiece composition (Fig. 3.14(b)) shows presence of oxygen (12.8 wt%). The composition of finished workpiece using MR fluid of Type – II is shown in Fig. 3.14(c). It also confirms the presence of oxygen (10.9 wt%). The presence of oxygen on the workpiece surface in both cases implies that the formation of oxide layer during finishing. Hence, in MFAF process, oxide layer forms on the finished surface which is important for the implant's performance as it promotes bio-activity and also restricts the bacterial growth on the implant surface.

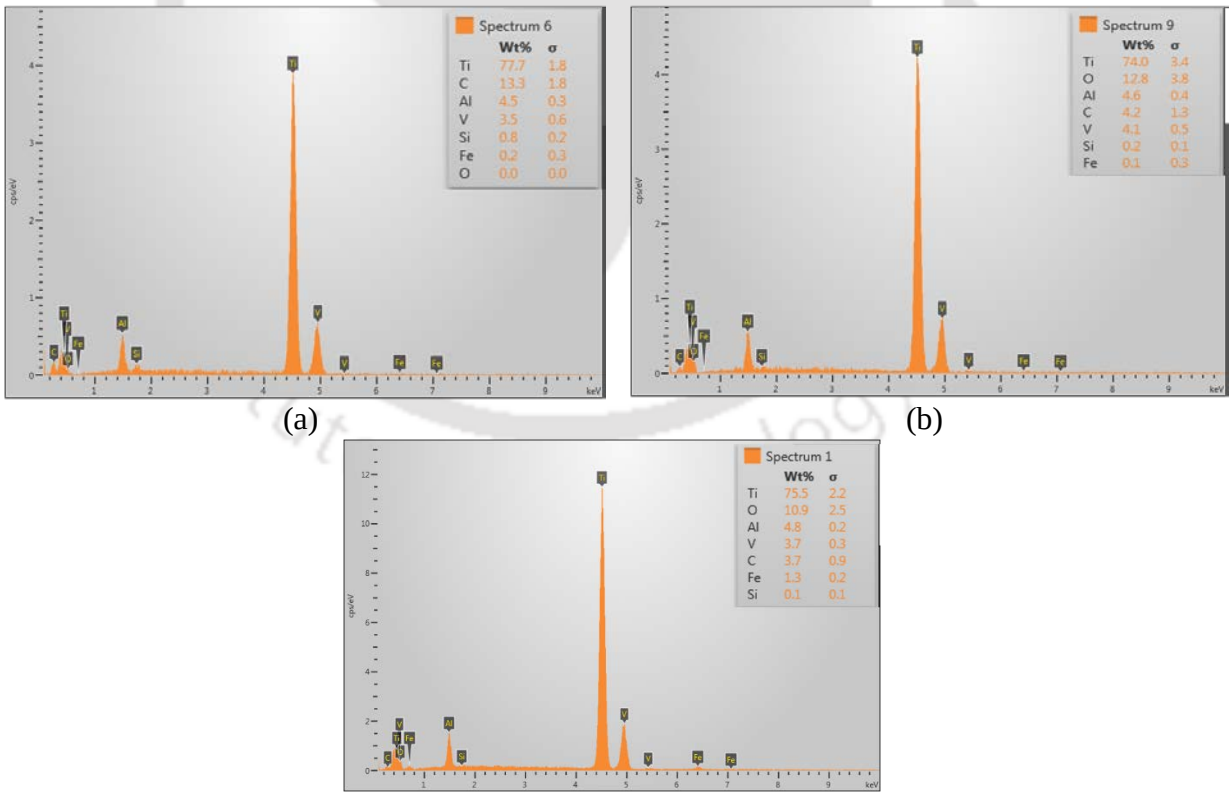

Fig. 3.14 EDX analysis for composition of workpiece surface (a) before finishing; Composition of workpiece surface after finishing by MR fluid of (b) Type I and (c) Type II

The chemical reaction between MR fluid of Type – I (having HF and HNO_3) and Ti alloy workpiece surface is much more aggressive than the reaction with MR fluid of Type – II (having H_2O_2). More softening of the workpiece surface occurs with MR fluid of Type – I than MR fluid of Type – II. Due to this more material removal and further easy removal of initial scratch marks by the abrasive particles occur which results in better surface finish while finishing using MR fluid of Type – I than MR fluid of Type – II. Therefore, MR fluid of Type – I provides smoother surface than MR fluid of Type – II. Hence, the measured contact angle on the surface finished with MR fluid of Type – I is less than the surface finished with MR fluid of Type – II.

3.3.4 Comparison of Experimental Results Using Different Toolpaths

Total three experiments are carried out for each toolpath for the comparison between the two toolpaths to ensure repeatability. Same experimental conditions (1200 tool rpm, 0.8 mm working gap and 6 hrs.30 min finishing time) are considered for both the toolpaths. Experimental results for both toolpaths are shown in Table 3.3.

Table 3.3 Experimental results for parallel and spiral toolpath

No. of experiments	Spiral toolpath			Parallel toolpath		
	Initial Ra	Final Ra	%ΔRa	Initial Ra	Final Ra	%ΔRa
1	0.16	0.06	62.50	0.15	0.01	93.33
2	0.14	0.04	71.42	0.13	0.02	84.61
3	0.34	0.11	67.64	0.12	0.01	91.67

The %ΔRa is higher in case of parallel toolpath for all three experiments as compared to spiral toolpath. Also, in case of parallel toolpath the range of obtained final surface roughness (10 nm–20 nm) is better than the spiral toolpath (60 nm–110 nm). Figure 3.15 shows the surface roughness profiles of workpiece surfaces before and after finishing using spiral toolpath. The deep valleys and high peaks in the initial surface roughness profile (Fig. 3.15(a)) is considerably decreased in the final surface roughness profile (Fig. 3.15(b)). Figure 3.16 shows the surface roughness profiles of workpiece surfaces before and after finishing using parallel toolpath. The final surface roughness profiles (Fig. 3.16(b)) show less number of high peaks than surface roughness profile obtained using spiral toolpath (Fig. 3.15(b)). After analyzing all the experimental results for both the toolpaths, it is clear that parallel toolpath produces higher %ΔRa than spiral toolpath. Also, the final surface roughness obtained due to parallel toolpath is in the range of 10 to 20 nm, which is a very good surface finish for biomedical application according to ISO 7207-

2:2011 [102]. Also, surface roughness profiles obtained after finishing with both the toolpath shows that parallel toolpath (Fig. 3.16) is better than the spiral toolpath (Fig. 3.15).

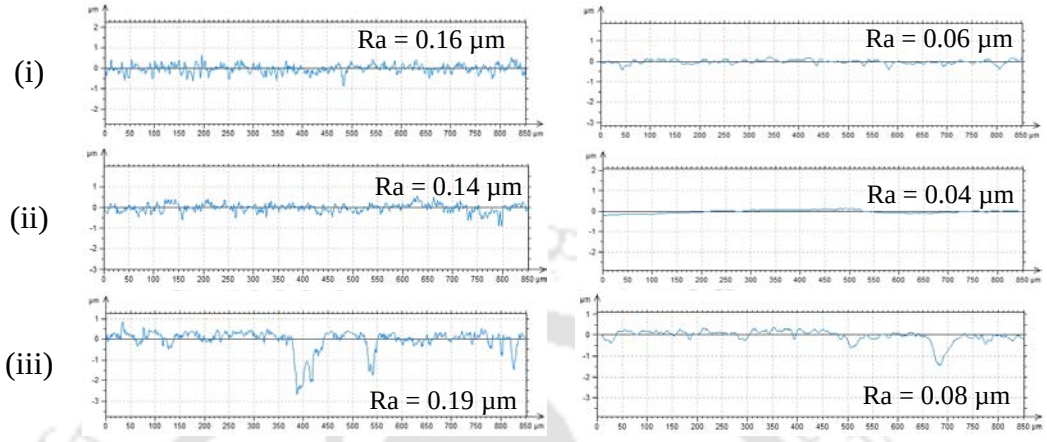

Fig. 3.15 Surface roughness profiles (wavelength cut-off–8 µm) of Ti alloy workpieces using spiral toolpath (a) before and (b) after finishing for (i) 1st, (ii) 2nd and (iii) 3rd experiment (Table 3.3)

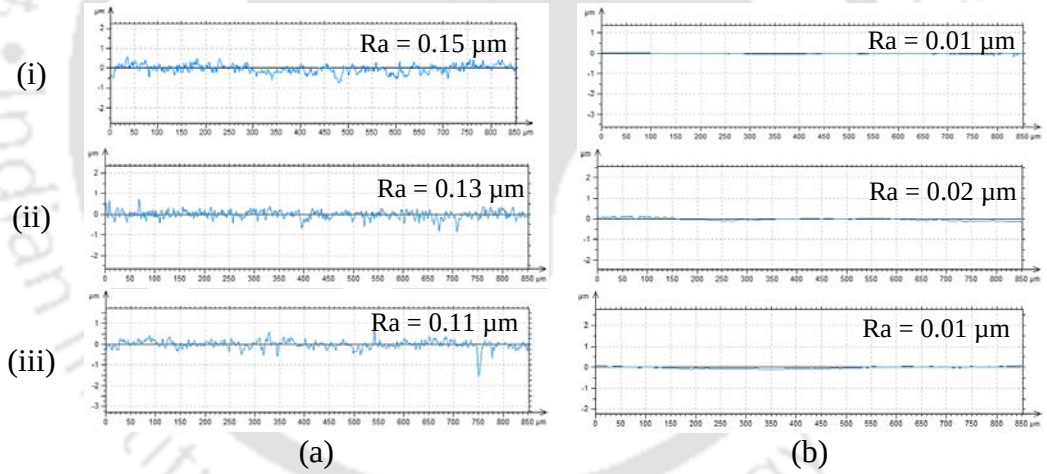

Fig. 3.16 Surface roughness profiles (wavelength cut-off–8 µm) of Ti alloy workpieces using parallel toolpath (a) before and (b) after finishing for (i) 1st, (ii) 2nd and (iii) 3rd experiment (Table 3.3)

After conducting all six experiments, the best result for spiral toolpath (Exp. No. 2 in Table 3.3) and parallel toolpath (Exp. No. 1 in Table 3.3) are considered to compare the finished surfaces. Figures 3.17(a) and (b) show the initial and final surface topography of the titanium workpiece obtained using optical profilometer. Figure 3.17(b) is the best surface obtained after finishing with spiral toolpath. As shown in the Fig. 3.17(a) initial area surface roughness (*Sa*) value is 150 nm and in Fig. 3.17(b) the final area surface roughness (*Sa*) value is 50 nm. Hence, the percentage change in area surface roughness is 66.67%. The final surface topography (Fig. 3.17(b)) shows

reduced scratch marks than the initial surface topography (Fig. 3.17(a)). Figures 3.18 (a) and (b) show initial and final surface topography of the Ti alloy workpiece when parallel toolpath is used. Figure 3.18(b) is the best surface obtained after finishing with parallel toolpath. The initial area surface roughness (*Sa*) value is 175 nm as shown in the Fig. 3.18(a) and in Fig. 3.18(b) the final area surface roughness (*Sa*) value is 12.74 nm. Hence, the percentage change in area surface roughness is 92.72% in case parallel tool path which is much higher than the spiral toolpath (66.67%). The final surface topography (Fig. 3.18(b)) obtained after using parallel toolpath is free from deep scratch marks and the achieved surface topography is better than the final surface topography obtained from spiral toolpath (Fig. 3.17(b)). After comparing 3D final surface topographies (Fig. 3.17(b) and Fig. 3.18(b)) for both the toolpaths, it is observed that the parallel toolpath generates better surface topography than spiral toolpath.

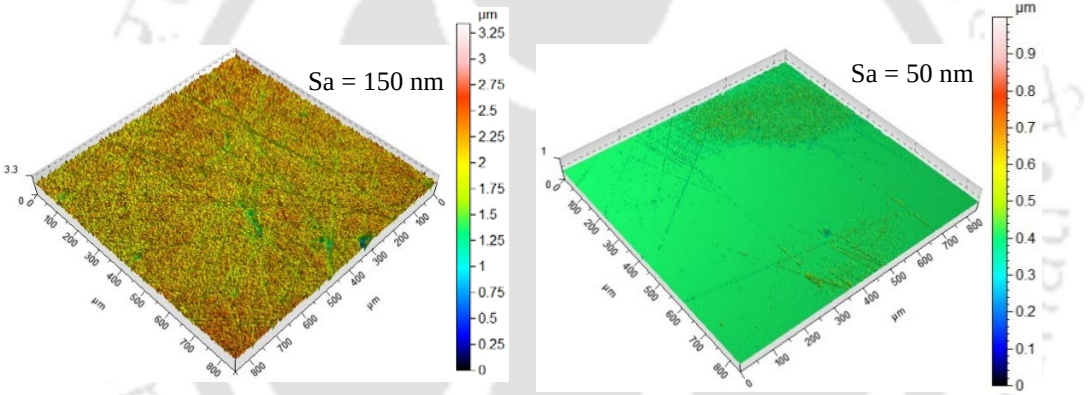

(a) (b)

Fig. 3.17 Best 3D surface topography image (i.e. optical profilometer image) of (a) initial and (b) final of Ti alloy workpiece after finishing using spiral toolpath (Exp. No. 2 in Table 3.3)

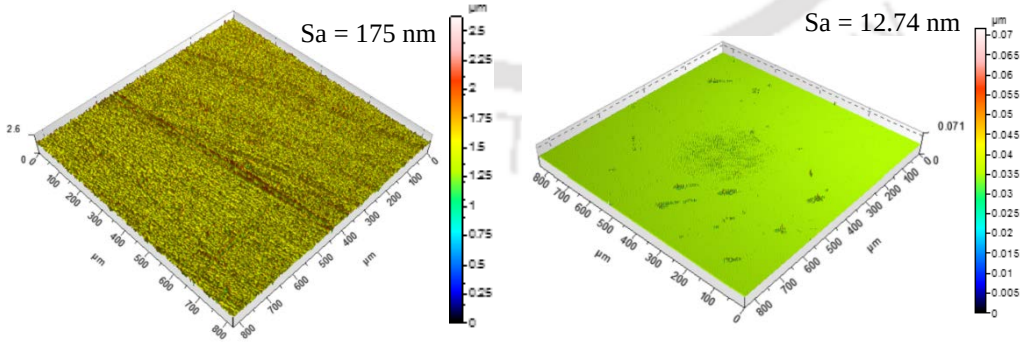

(a) (b)

Fig. 3.18 Best 3D surface topography image (i.e. optical profilometer image) of (a) initial and (b) final of Ti alloy workpiece after finishing using parallel toolpath (Exp. No. 1 in Table 3.3)

Figures 3.19(a) and (b) show the atomic force microscope (AFM) images of the workpiece surface before and after finishing while employing spiral toolpath. The AFM image of the initial

surface (Fig. 3.19(a)) shows valleys, peaks and scratch marks. The AFM image after finishing (Fig. 3.19(b)) shows few remaining scratch marks on the finished surface although the rest of the surface is highly polished. Figures 3.20(a) and (b) show the best AFM images of the workpiece surface before and after finishing when parallel toolpath is employed. The AFM image of the initial surface (Fig. 3.20(a)) shows deep valleys and high peaks. However, after finishing, the AFM image (Fig. 3.20(b)) shows uniformly finished surface without any prominent scratch marks. Figures 3.21(a) and (b) show the FESEM images at 1000X magnification of the workpiece surface before and after finishing when spiral toolpath is used. The scratch marks in the final surface (Fig. 3.21(b)) are reduced. Figures 3.22(a) and (b) show the FESEM images at 1000X magnification of the workpiece surface before and after the finishing when parallel toolpath is used. The deep scratch marks on the initial surface vanish (Fig. 3.22(a)) in the final surface (Fig. 3.22(b)). Also, the final surface texture (Fig. 3.22(b)) obtained from the parallel toolpath has fewer scratch marks and smoother than the final surface texture obtained from the spiral toolpath (Fig. 3.21(b)). Hence, after analyzing surface textures for both toolpaths, it is clear that parallel toolpath is better suited for polishing Ti alloy in the present study.

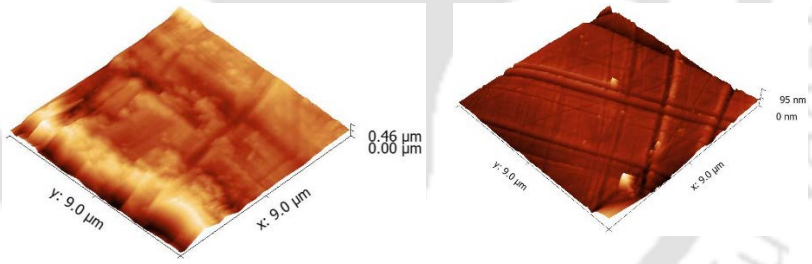

(a) (b)

Fig. 3.19 Best AFM images of (a) initial and (b) final surface obtained using spiral toolpath (Exp. No. 2 in Table 3.3)

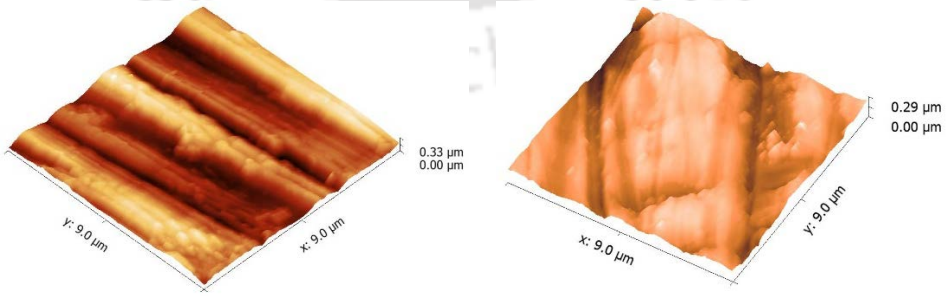

(a) (b)

Fig. 3.20 Best AFM images of (a) initial and (b) final surface obtained using parallel toolpath (Exp. No. 1 in Table 3.3)

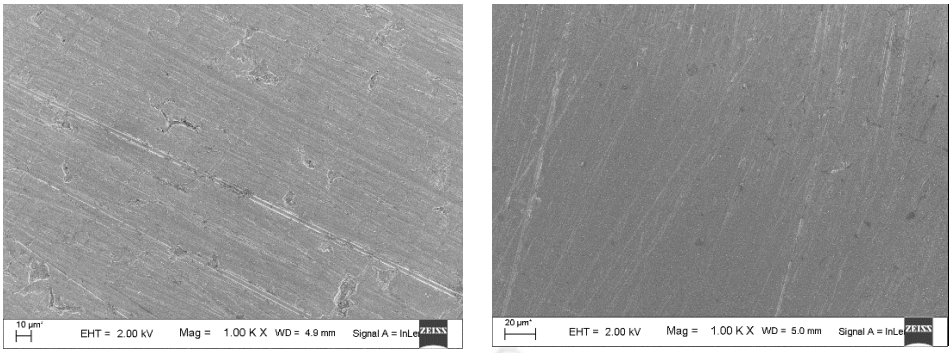

(a) (b)

Fig. 3.21 Best FESEM images at 1000X magnification of (a) initial and (b) final surface obtained using spiral toolpath (Exp. No. 2 in Table 3.3)

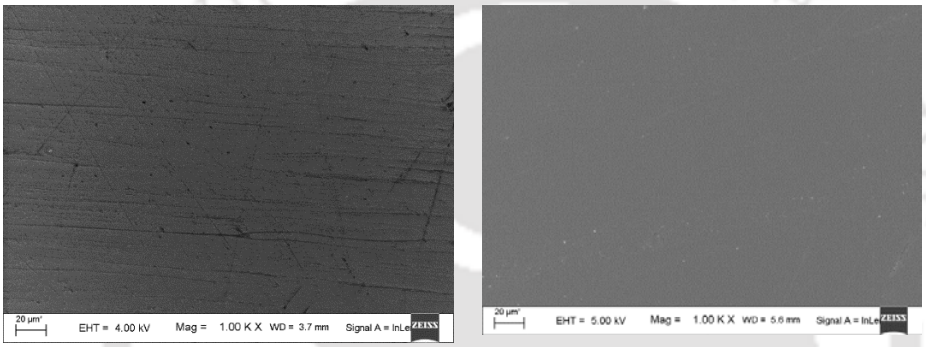

(a) (b)

Fig. 3.22 Best FESEM images at 1000X magnification of (a) initial and (b) final surface obtained using parallel toolpath (Exp. No. 1 in Table 3.3)

3.4 Summary

Different types of surfaces are generated using two types of MR fluid on Ti alloy. The generated surface morphologies are studied and analyzed in relation to the implant surfaces. The obtained surface roughness after finishing with MR fluid of Type – I is 10 nm (having %ΔRa of 98.21%) and with MR fluid of Type – II is 70 nm (having %ΔRa of 89.06%). The finished surface with MR fluid of Type – II has more number of pits and valleys than the surface finished with MR fluid of Type – I as observed from surface topography. From wettability study, it is found that the surface finished with MR fluid of Type – I is hydrophilic in nature while with MR fluid of Type – II is hydrophobic. The conclusions drawn from the experimental study is as follows:

- The surface characteristics obtained from MR fluid of Type – I is better suited for semi-permanent type of implants or implants which partake in relative motion like femoral part of knee joint and hip joint.

- MR fluid of Type – II is better suited for permanent implants like dental implants. It is better suited to finish permanent implants as it provides better chance of osseointegration.
- The formation of oxide layer on the finished surface is observed which enhances the bio-compatibility of the implant.
- The necessary implant surfaces can be generated depending upon the requirements with the help of specific composition of MR fluid.

Spiral and parallel toolpath are generated using sprutcam® software to find out the appropriate toolpath to finish the workpiece. From the experimental studies, it is found that parallel toolpath gives the best surface finish, surface topography and as well as surface texture. Final surface roughness obtained after using parallel toolpath is 10 nm. The obtained surface roughness is sufficient enough for biomedical application of Ti alloy according to literature survey. The surface topography and surface texture show reduced surface roughness and scratch marks when the surface is finished with parallel toolpath. Hence, in MFAF process parallel toolpath performs better than spiral toolpath while finishing Ti alloy at the nanometer level.

Chapter 4 Characterization of 3D surface parameters of finished surface

4.1 Introduction

Nowadays, 3D surface parameters (according to ISO 25178-605 [106]) are widely used to understand and interpret surface topography due to the 3D nature of the surface. Surface topography is a very important feature for different types of implant materials. Surface topography and surface texture are the key controlling elements to increase the lifespan and performance of implants. Implants performance and longevity can be improved by finishing the implant surface up to nanometer level having particular surface topography. In the present study, one height parameters (*Sa*) and three functional parameters (*Spk*, *Sk* and *Svk*) are considered. The parameters are selected on the basis of their significance concerning implant material. The significance of the surface parameters concerning femoral knee joint implant is explained below.

Sa*: *Sa is **arithmetic mean of absolute height** in the measured sampling area. *Sa* gives the general idea of surface texture [107]. From *Sa* values the general idea of the knee implant surface topography is attainable. Low *Sa* value generally implies better surface finish. However, only *Sa* values are not sufficient to define a surface as it does not differentiate between peaks, valleys and the spacing of the various texture features. Different functional 3D surface parameters (i.e. *Spk*, *Sk* and *Svk*) are also considered to understand and interpret the generated surface of the implant.

***Spk*:** The **reduced peak height** as shown in Fig. 4.1 is expressed as *Spk*. This is the peak height above the core roughness of the surface [107]. The femoral knee joint implant produces debris during in-vivo performance. This parameter can be used to define the amount of debris generation. With the reduction of *Spk*, wear particle debris generation will be less. Hence, small *Spk* value refers to less wear during the implant performance.

***Sk*:** *Sk* i.e. **core roughness depth** as shown in Fig. 4.1 measures the peak-to-valley height of the surface after removal of the predominant peaks and valleys [107]. Lower core roughness depth

indicates better wear properties. Hence, a small value of the final *Sk* implies better wear properties of the knee implant.

Svk*: *Svk i.e. **reduced valley depth** measures the valley depth below core roughness [107] as shown in Fig. 4.1. The presence of valley increases body fluid retention capability which results in better femoral implant performance. Hence, higher value of *Svk* means better performance of the implant material.

In this chapter, finishing experiments are carried out based on response surface methodology (RSM) of statistical design of experiments (DOE). Central composite rotatable design (CCRD) of RSM is used to plan the experiments. This method is very efficient to achieve optimal process performance [108]. In RSM, a minimum number of experiments will provide maximum amount of information about the process.

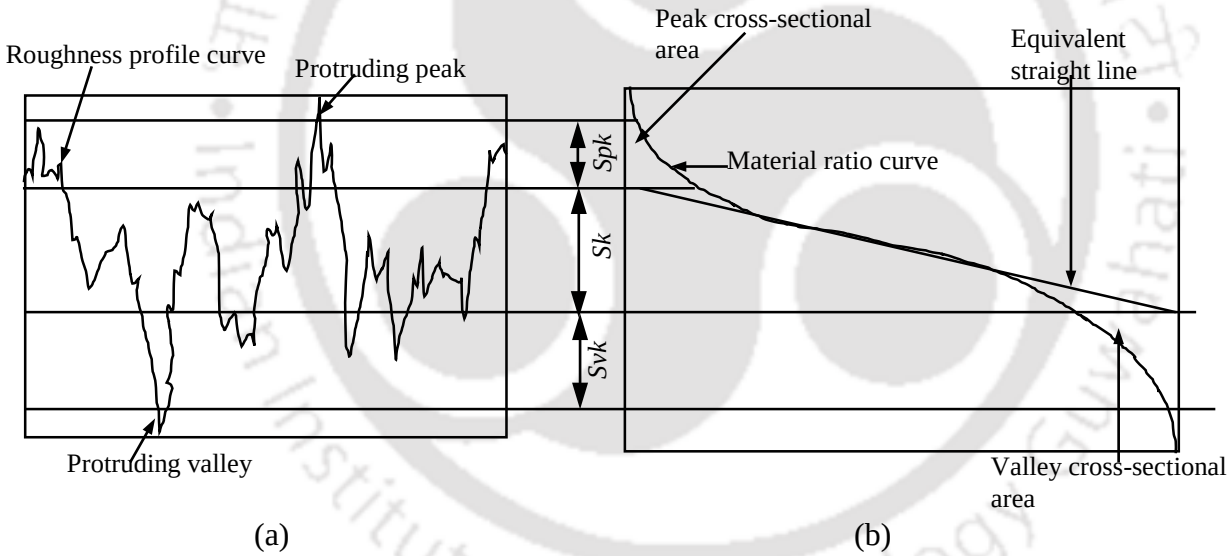

Fig. 4.1 (a) Surface roughness profile and (b) material ratio curve along evaluation length showing three functional parameters i.e. core roughness depth (*Sk*), reduced peak height (*Spk*) and reduced valley depth (*Svk*)

The objective of the present study is to find out the optimum values of the process parameters to obtain minimum value of *Sa, Spk, Sk* and maximum value of *Svk*. CCRD is used for fitting a second order model and to optimize the input process parameters to acquire necessary 3D surface roughness parameter values for Ti alloy. Optimization of the process parameters of MFAF process will give necessary surface finish and surface topography for higher performance and longevity of femoral knee joint implant after finishing. Also, the effect of each process parameter

on output responses is analyzed for better understanding of the finishing process. After that, validation experiments are conducted to confirm the optimization results obtained from the DOE study.

4.2 Experimental Investigation

From preliminary experimental study, it is observed that the main influential process parameters in MFAF process are rpm of the tool (*N*), working gap (*G*) between tool & workpiece and finishing time (*T*). The 3D surface roughness parameters (i.e. height and functional parameters) are considered as output responses. The range of each process parameters with coded levels and actual values are given in Table 4.1. The plan of experiments along with all the responses are shown in Table 4.2. All the surface roughness parameters are measured before and after experiments using optical profilometer. The initial *Sa* values of all the workpiece are in the range of 70-80 nm having minor variation. Hence, the final value of the 3D surface parameters after finishing are considered as responses due to the uniformity of the initial surface roughness of the workpiece. Also, final values of the surface roughness parameters are enough to interpret the surface roughness and topography of the workpiece.

Table 4.1 Coded levels and actual values of the process parameters

Sr. No.	Parameter	Unit	Levels		
			−1	0	1
1	RPM of the tool (*N*)	rpm	600	900	1200
2	Working gap (*G*)	mm	0.6	1	1.4
3	Finishing time (*T*)	hrs.	4	5	6

Table 4.2 Plan of experiments

Std.	Factors			Responses (nm)			
	N (rpm)	*G* (mm)	*T* (hrs.)	Final *Sa**	Final *Spk*	Final *Sk*	Final *Svk*
1	600	0.6	4	12.33	16.90	19.04	50.03
2	1200	0.6	4	18.06	29.38	16.01	62.75
3	600	1.4	4	11.22	13.99	24.55	36.32
4	1200	1.4	4	16.83	16.48	16.87	43.20
5	600	0.6	6	37.73	22.83	19.36	32.56
6	1200	0.6	6	39.17	30.08	13.93	52.03
7	600	1.4	6	31.75	16.99	17.33	32.44
8	1200	1.4	6	33.07	24.22	11.32	45.07
9	400	1	5	17.55	19.79	25.06	42.37
10	1400	1	5	35.10	36.22	10.75	49.33
11	900	0.4	5	20.92	23.45	3.17	55.56

12	900	1.6	5	25.76	18.14	11.15	43.06
13	900	1	3:30	15.53	10.91	25.23	14.538
14	900	1	6:30	49.77	13.59	12.65	28.88
15	900	1	5	4.90	5.90	1.90	24.54
16	900	1	5	10.81	7.49	6.69	20.95
17	900	1	5	4.20	4.93	2.73	13.10
18	900	1	5	11.80	9.51	6.27	24.57
19	900	1	5	6.41	3.08	2.57	22.92
20	900	1	5	8.91	5.19	8.36	18.68

*Sa** – Surface roughness, *Spk*– reduced peak height, *Sk*– core roughness depth and *Svk*– reduced valley depth

4.3 Results and Discussion

Analysis of variance (ANOVA) for final *Sa* and final *Spk* is shown in Table 4.3. ANOVA table helps to understand the significance of the developed model and the impact of the process parameters on the responses. In Table 4.3, ANOVA models for both final *Sa* and final *Spk* are significant as *p* values ("Prob > F") for both the cases are less than 0.05 for 95% significance level. For final *Sa*, the significant model terms are *N*, *T*, N^2, G^2 and T^2. The significant model terms for final *Spk* are *N*, *G*, *T*, N^2, G^2 and T^2. Also, it is found that "Lack of Fit" relative to the pure error is insignificant for both the cases. In case of *Sa*, the most significant term is *T* i.e. finishing time with highest contribution (47.88%) followed by T^2 i.e. square of the finishing time (26.62% contribution) and N^2 i.e. square of rpm of the tool (12.55% contribution). For final *Spk* the contribution of the most significant terms in descending order is square of the rpm of the tool (49.82% contribution), square of the working gap (22.94% contribution) and finishing time (14.74% contribution). The coefficient of determination (R^2) value in case of final *Sa* is 0.92 and in case of final *Spk* is 0.96 which shows good fitting of the regression equation with the experimental results. From regression analysis, the response surface models for final *Sa* and final *Spk* are given in Eqs. (4.1) and (4.2), respectively.

$$Sa = 212.31 - 0.07N - 44.86G - 71.46T - 2.60\times10^{-4}NG - 3.57\times10^{-3}NT - 3.04GT + 5.74\times10^{-5}N^2 + 29.44G^2 + 8.85T^2 \quad (4.1)$$

$$Spk = 148.84 - 0.12N - 79.20G - 21.47T - 0.01NG - 2.06\times10^{-4}NT + 1.28GT + 8.37\times10^{-5}N^2 + 37.52G^2 + 2.20T^2 \quad (4.2)$$

As shown in Table 4.4, ANOVA models for both *Sk* and *Svk* are significant. For *Sk*, the most significant model terms in descending order are T^2 (40.59%), N^2 (31.43%) and *N* (14.88%) while for *Svk* the most significant model terms are G^2 (47.59%), N^2 (33.16%) and N (7.97%). Also, "Lack of Fit" for both *Sk* and *Svk* are insignificant relative to the pure error. The R^2 value for *Sk* and *Svk* are 0.93 and 0.90, respectively which proves that the regression line approximates the real data points very well. From regression analysis, the response surface models for *Sk* and *Svk* are given in Eqs. (4.3) and (4.4), respectively.

$$Sk = 213.72 - 0.10N + 9.86G - 63.29T - 5.45\times10^{-3}NG - 3.08\times10^{-4}NT - 3.43GT + 5.35\times10^{-5}N^2 + 7.48G^2 + 6.43T^2 \quad (4.3)$$

$$Svk = 260.45 - 0.18N - 204.45G - 21.77T - 0.01NG + 5.20\times10^{-3}NT + 8.18GT + 1.03\times10^{-4}N^2 + 81.80G^2 + 0.82T^2 \quad (4.4)$$

Table 4.3 ANOVA for Final *Sa* and Final *Spk*

Source	Final *Sa*			Final *Spk*		
	F Value	***p*-value Prob > F**	**Percent contribution**	**F Value**	***p*-value Prob > F**	**Percent contribution**
Model	12.56	**0.0002**		27.04	< **0.0001**	
N	5.26	**0.04**	4.58	37.03	**0.0001**	14.74
G	0.16	0.7016	0.14	15.63	**0.0027**	6.22
T	54.99	< **0.0001**	47.88	5.68	**0.0384**	2.26
NG	0.00	0.9866	0.00	1.94	0.1937	0.91
NT	0.35	0.5682	0.30	0.00	0.9464	0.00
GT	0.45	0.5174	0.39	0.33	0.5791	0.13
N^2	14.41	**0.0035**	12.55	125.16	< **0.0001**	49.82
G^2	8.66	**0.0147**	7.54	57.64	< **0.0001**	22.94
T^2	30.57	**0.0003**	26.62	7.80	**0.0190**	3.10
Lack of Fit	4.32	0.0672		1.59	0.3119	

Hence, from ANOVA for all the responses (Tables 4.3 & 4.4), it can be concluded that the square of the working gap between the tool and workpiece is the most significant process parameter to control surface finish, wear capability and performance criteria of the implant.

An optimization study is carried out based on Derringer and Suich's algorithm [109] considering multiple responses. This algorithm uses desirability functions. The desirability shape of the goal can be changed by the weight field. Weights are assigned to target value for added

emphasis. 3D surface roughness parameters are the primary target performance. Minimizing of *Sa*, *Spk* and *Sk* and maximizing of *Svk* is the objective of the optimization study. Upper and lower limits are specified for the input process parameters as mentioned in Table 4.1. Weight value of 1 is added to all the input process parameters values and responses. With the added weight the parameters will behave in a linear way. The results of the optimization study are given in Table 4.5. From Table 4.5, it can be concluded that to achieve optimum 3D surface parameter values, the rotation speed of the tool should be 901.63 rpm with a working gap of 0.6 mm and finishing time of 4 hrs. 45 min The effect of each process parameter on surface roughness and surface topography is discussed in the next sub-section.

Table 4.4 ANOVA for Final *Sk* and Final *Svk*

Source	Final *Sk*			Final *Svk*		
	F Value	***p*-value Prob > F**	**Percent contribution**	**F Value**	***p*-value Prob > F**	**Percent contribution**
Model	14.20	**0.0001**		10.58	**0.0005**	
N	19.57	**0.0013**	14.88	7.82	**0.0189**	7.97
G	1.89	0.1993	1.44	7.40	**0.0216**	7.54
T	11.17	**0.0075**	8.49	0.16	0.6979	0.16
NG	0.43	0.5267	0.38	0.53	0.4822	0.59
NT	0.01	0.9280	0.01	0.52	0.4884	0.53
GT	1.90	0.1986	1.44	2.27	0.1628	2.31
N^2	41.36	< **0.0001**	31.43	32.55	**0.0002**	33.16
G^2	1.85	0.2034	1.41	46.71	< **0.0001**	47.59
T^2	53.41	< **0.0001**	40.59	0.18	0.6772	0.19
Lack of Fit	1.21	0.4210		2.91	0.1330	

Table 4.5 Results of the optimization study

Sol. no.	***N*** **(rpm)**	***G*** **(mm)**	***T*** **(hrs.)**	**Final *Sa* (nm)**	**Final *Spk* (nm)**	**Final *Sk* (nm)**	**Final *Svk* (nm)**	**Desirability**	
1	**901.63**	**0.60**	**4.65**	**10.82**	**14.94**	**6.03**	**39.98**	**0.703**	Selected
2	944.09	0.60	4.68	11.62	15.87	5.58	40.86	0.701	
3	1018.96	1.40	5.03	15.06	11.79	6.06	31.78	0.645	

4.3.1 Effect of Process Parameters on Output Responses

The effects of individual process parameter on output responses are calculated using regression equations (Eqs. ((4.1) – (4.4))). The effect of tool rpm on *Sa*, *Spk*, *Sk* and *Svk* are shown in Figs. 4.5 – 4.8. With the increase in rpm of the tool, the values of the 3D surface roughness

parameters start to decrease till it reaches a certain speed. Beyond that particular speed, 3D surface roughness parameter values start to increase with an increase in the tool rpm.

Centrifugal force (F_{cfg}) acts as finishing force in MFAF process. It depends on the tool rpm. The centrifugal force (F_{cfg}) acting on an abrasive particle is given as [110].

$$F_{cfg} = m\left(\frac{2\pi N}{60}\right)^2 r \tag{4.5}$$

where, m is the mass of the abrasive particle, N is the rpm of the tool and r is the distance between the axis of the cylindrical tool and a particular abrasive particle. Hence, the finishing force (i.e. F_{cfg}) acting on the abrasive particle increases with the increase in the tool rpm. The increased finishing force results in a higher material removal from the roughness peaks. Hence, with the increase in tool rpm final *Sa*, *Spk*, *Sk* and *Svk* values decrease. The value of F_{cfg} increases further with higher tool rpm. Due to the growing force, the CIP chains start to break due to the shear thinning nature of MR fluid and the abrasive particles break loose from the CIP chain structures and move into the outward direction from the finishing zone. It is explained clearly with the help of schematic diagrams in Fig. 4.2. In Fig. 4.2(a), unyielded CIP chains are observed while there is no shear force like tool rotation or translational motion of the workpiece. The CIP chains are started to shear without breakage with slight increase in tool rpm as shown in Fig. 4.2(b). However, at high rpm (>1100 rpm), shearing force also becomes very high which leads to breakage in chain structure and it gets little time to recombine as shown in Fig. 4.2(c).

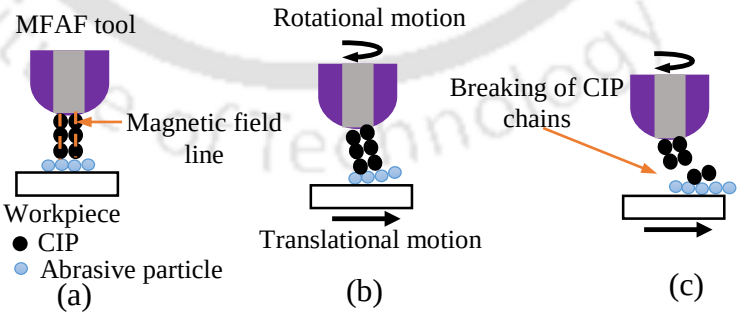

Fig. 4.2 CIP chains and abrasive particles in MR fluid below MFAF tool under (a) static condition, (b) nominal shearing condition & sheared chains without breaking and (c) high shearing condition & breaking of chains

Hence, the strength of the CIP chains reduces due to the breaking of the chains and the CIP chains does not provide sufficient bonding force to the abrasive particles for cutting the roughness

peaks. It results in a lower material removal. Hence, higher value of final 3D surface roughness parameters is observed. As shown in the Figs. 4.5 – 4.8, the effect of working gap on final *Sa, Spk, Sk* and *Svk* is significant. Initially, final 3D surface roughness parameter values start to decrease with the increase in the working gap and it reaches to a particular value. Increasing working gap means there is an increase in the available abrasive particles in the finishing zone resulting in higher material removal. Higher material removal gives low final *Sa, Spk, Sk* and *Svk* values. However, further increase in the working gap beyond this particular working gap, the final *Sa, Spk, Sk* and *Svk* values start to increase. With an increase in the working gap, there is a reduction in magnetic force on the abrasive particles through surrounding CIP chains which results in the lower indentation of the abrasive particles on the workpiece surface. Hence, penetration depth by the abrasive particle decreases resulting in an increase in final *Sa, Spk, Sk* and *Svk* values. The effect of working gap on 3D surface topography of the workpiece is shown in Fig. 4.3. The initial unfinished workpiece surface shows deep scratch marks as shown in Fig. 4.3(a). Finishing experiments are carried out at 1 mm (Fig. 4.3(b)) and 1.4 mm (Fig. 4.3(c)) working gap with tool rpm of 1000 and 4 hrs. of finishing time. The surface topography in Fig. 4.3(b) for 1 mm working gap shows no scratch marks with low roughness peaks and a very good surface finish is achieved. However, the generated surface topography (Fig. 4.3(c)) for 1.4 mm working gap shows the presence of initial scratch marks which MR polishing fluid could not remove properly. It proves that at 1.4 mm working gap the finishing capability of abrasive particles reduces. It happens due to the insufficient magnetic flux density in the finishing zone. The available magnetic flux density under the tool after 1.4 mm working gap is less than 0.2 T which is not enough to carry out the finishing operation efficiently [111].

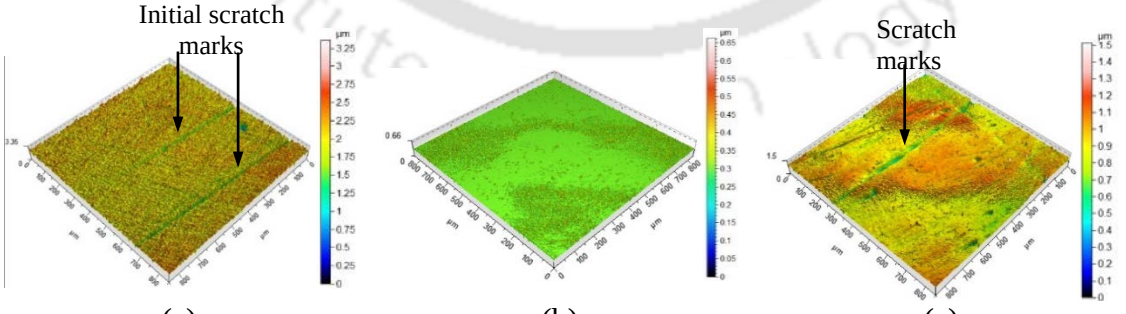

(a) (b) (c)

Fig. 4.3 3D surface topography of workpieces (a) before finishing, for (b) 1 mm and (c) 1.4 mm working gap with 1000 tool rpm and 4 hrs. finishing time

Figs. 4.5 – 4.8 show the effect of finishing time on output responses. Initially, final *Sa, Spk, Sk* and *Svk* values start to decrease with the increase in the finishing time until it reaches an

optimum value. However, beyond the optimum value, 3D surface roughness parameter values start to increase with further increase in the finishing time. At first, with the increase in the finishing time, the abrasive particles get more time to finish the surface resulting in low 3D surface roughness parameter values. After the optimum finishing time, the abrasive particles rub the already finished surface resulting in an increase in the response parameters. The effect of finishing time on 3D surface topography of the workpiece is shown in Fig. 4.4. The initial surface topography with high peaks and deep valleys is shown in Fig. 4.4(a). Here, the experiments are carried out at 1000 tool rpm and 1 mm working gap. After finishing for 4 hrs. 30 min, the generated surface has little scratch marks than the initial surface with reduced surface roughness as shown in Fig. 4.4(b). After finishing for 6 hrs., abrasive particles start to scratch the already finished surface which deteriorates the final surface as shown in Fig. 4.4(c).

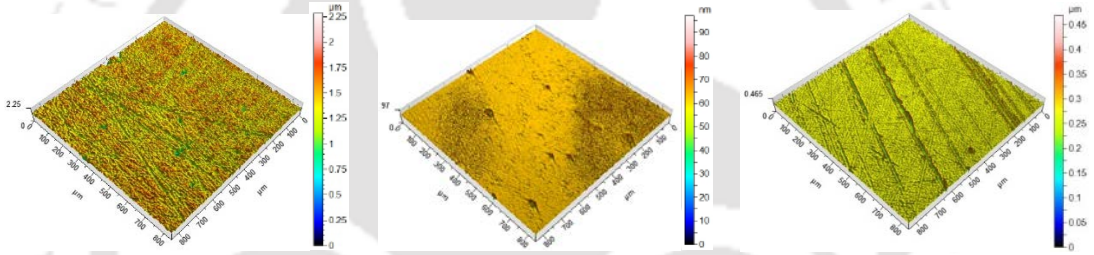

(a) (b) (c)

Fig. 4.4 3D surface topography of workpieces (a) before finishing, after (b) 4 hrs. 30 min and (c) 6 hrs. finishing time with 1000 tool rpm and 1 mm working gap

4.3.1.1 Effect of Process Parameters on Final *Sa*

Sa determines the overall surface roughness of the implant material. Hence, lower value of final *Sa* implies overall good surface finish of the component. Effect of tool rpm on final *Sa* is shown in Figs. 4.5(a) and (c) where it is observed that with the increase in tool rpm the final *Sa* starts to decrease. However, beyond 900 rpm, the final *Sa* starts to increase. The reason for which is already explained in section 4.3.1. The final surface roughness differs at different working gap for a certain tool rpm as shown in Fig. 4.5(c). At 0.6 mm working gap, the value of surface roughness is higher because of less amount of abrasive particle in the finishing zone. At 1 mm working gap, the available active abrasive particles increase result in a decrease in final surface roughness. At 1.4 mm working gap the magnetic force responsible for indenting the abrasive particle reduces. Hence, the material removal starts to decrease which increases the final *Sa* value.

Effect of working gap on final *Sa* is shown in Figs. 4.5(a), (b), (c) and (b). With the increase in working gap final *Sa* values start to decrease due to the increase of active abrasive particles in the finishing zone. The increased amount of active abrasive particles removes more material resulting in low final *Sa* values. However, after 1.2 mm working gap final *Sa* values start to increase due to the reduction of magnetic force acting on the abrasive particles. As shown in Fig. 4.5(d), for the same working gap, the final *Sa* values are different at different finishing time. Hence, the finishing capability of the abrasive particles decreases resulting in lower material removal rate which in turn increases final *Sa* values.

Effect of finishing time on final *Sa* values are shown in Figs. 4.5(b) and (d). After 5 hrs. 30 min of finishing time, the final *Sa* values start to increase at a higher rate due to the longer finishing time. With a longer finishing time, the abrasive particles start to abrade the already finished workpiece surface which increases final *Sa* values. Hence, to achieve good surface finish for Ti alloy implant the range of tool rpm, working gap and finishing time should be in the range of 800–1000 rpm, 0.8–1.2 mm and 4–5 hrs., respectively.

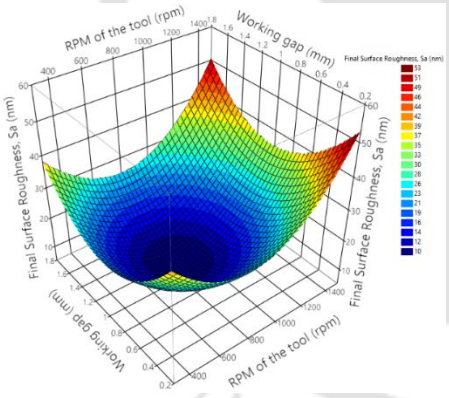

(a)

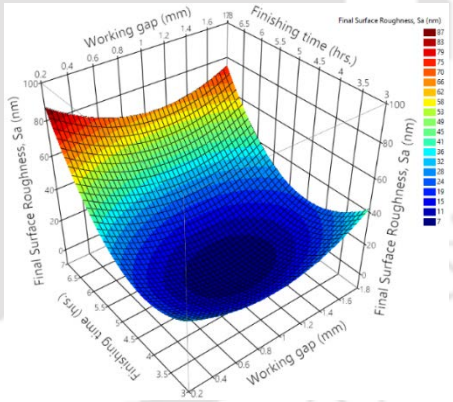

(b)

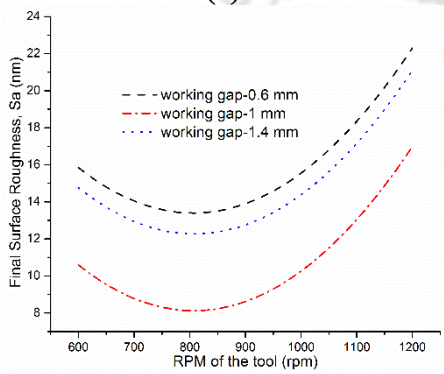

(c)

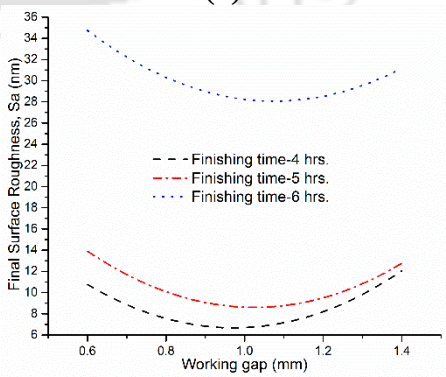

(d)

Fig. 4.5 3D graph showing the combined effect of (a) rpm of the tool & working gap and (b) working gap & finishing time on final surface roughness (*Sa*); The effect of (c) rpm of the tool at different working gap and (d) working gap at different finishing time on final *Sa*

4.3.1.2 Effect of Process Parameters on Final *Spk*

Wear properties of bearing surfaces of femoral knee implant greatly depends on final *Spk* values. Low final *Spk* value implies good wear properties which are required for the use of Ti alloy as a femoral knee joint implant. Effect of tool rpm on final *Spk* is shown in Figs. 4.6(a) and (c) where it is observed that with the increase in the tool rpm the final *Spk* starts to decrease. However, beyond 900 rpm with the increase in tool rpm, the final *Spk* starts to increase. As *Spk* represents the mean height of peaks above the core surface, the increasing tool rpm helps in shearing of the roughness peaks which decreases the final *Spk* values. After 900 rpm shearing of the peaks starts to decrease due to the weak bonding of the active abrasive particles in the finishing zone which increases the final *Spk* values. As shown in Fig. 4.6(c), the final *Spk* is different at different working gaps for the same tool rpm. At 0.6 mm working gap, amount of active abrasive particle in the finishing zone is low resulting in lower rate of peak shearing. At 1 mm working gap the available active abrasive particle increases result in higher rate of peak shearing which decreases the final *Spk* values. At 1.4 mm working gap, the magnetic force responsible for indenting of abrasive particle reduces which lowers the peak shearing capability of abrasive particles resulting in higher final *Spk* values than 1 mm working gap.

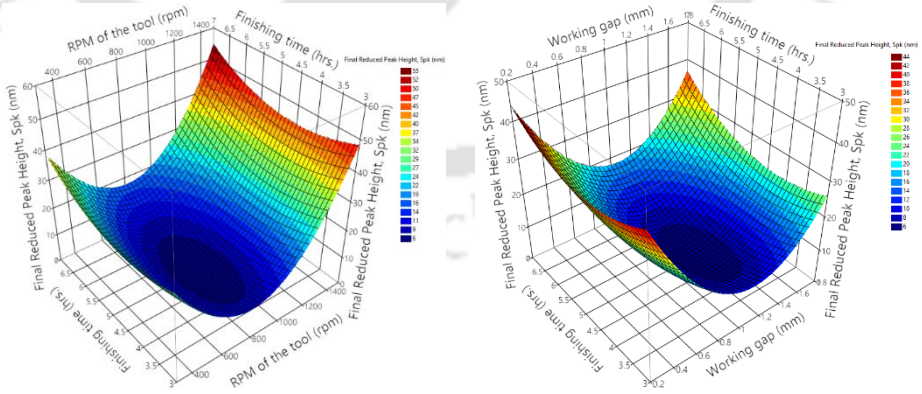

(a) (b)

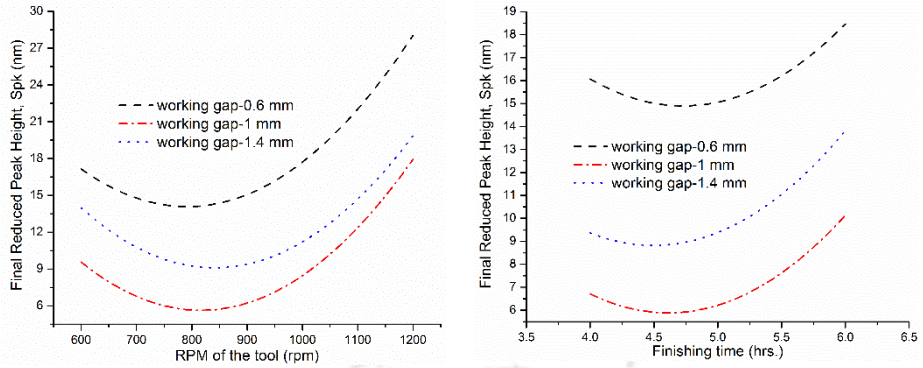

(c) (d)

Fig. 4.6 3D graph showing the combined effect of (a) finishing time & rpm of the tool and (b) finishing time & working gap on final reduced peak height (*Spk*); The effect of (c) rpm of the tool and (d) finishing time on final *Spk* at different working gap

Effect of working gap on *Spk* is shown in Fig. 4.6(b), (c) and (d). With the increase in working gap, final *Spk* values start to decrease, however after 1.2 mm working gap it starts to increase. The reason behind these is already explained in the previous paragraph.

Figures 4.6(a), (b) and (d) show the effect of finishing time on final *Spk* values. From 4 to 5 hrs. finishing time, the final *Spk* values start to decrease with increasing finishing time. This increases the interaction time of active abrasive particles with the workpiece surface which results in more shearing of peaks. After 5 hrs. of finishing time, final *Spk* value starts to increase because the abrasive particles start to plow the finished surface resulting in higher peaks. Hence, to achieve good wear properties rpm of the tool, working gap and finishing time should be in the range of 700–900 rpm, 0.9–1.2 mm and 4–5 hrs., respectively during MFAF process.

4.3.1.3 Effect of Process Parameters on Final *Sk*

Low *Sk* value implies less wear of the femoral knee joint implant during in vivo performance. From the Figs. 4.7(a) and (c), it is observed that with the increase in tool rpm the final *Sk* values start to decrease however beyond 1100 rpm its value starts to increase. Final *Sk* value is calculated by subtracting the minimum height from the maximum height of the core surface. Now, with the increase in tool rpm the material removal capability of abrasive particles increase. These results in decreasing the difference between maximum and minimum height of the core surface. Due to this, the final *Spk* values start to decrease. However, after 1100 rpm due to the reduction of finishing capability of abrasive particles the difference between maximum and minimum height of the core surface starts to increase resulting in higher final *Sk* values.

Effect of working gap on final *Sk* values is shown in Fig. 4.7(b). Final *Sk* values start to decrease up to 1.2 mm working gap. Increasing working gap implies higher amount of active abrasive particles in the finishing zone which helps to reduce difference between minimum height and maximum height. However, after 1.2 mm working gap final *Sk* values start to increase with the increase in working gap due to the reduction in finishing force.

The effect of finishing time on final *Sk* values is shown in Figs. 4.7(a), (b) and (c). Initially, with the increase in finishing time final *Sk* values start to decrease, however after 5 hrs. 30 min final *Sk* values start to increase with increasing finishing time. Before 5 hrs. 30 min finishing time the abrasive particles finish the workpiece surface by reducing the peak height which in turn diminishes the maximum and minimum height difference resulting in lower final *Sk* values. After 5 hrs. 30 min, the abrasive particles start to abrade the already finished workpiece resulting in unwanted scratch marks. These escalate the difference between the maximum and minimum height implying increase in the final *Sk* values. As shown in Fig. 4.7(d), for same tool rpm final *Sk* values are different for different finishing time. Hence, to achieve better performance and wear properties for Ti alloy implant rpm of the tool, working gap and finishing time should be in the range of 800–1100 rpm, 0.8–1.2 mm and 4 hrs. 30 min–5 hrs. 30 min, respectively.

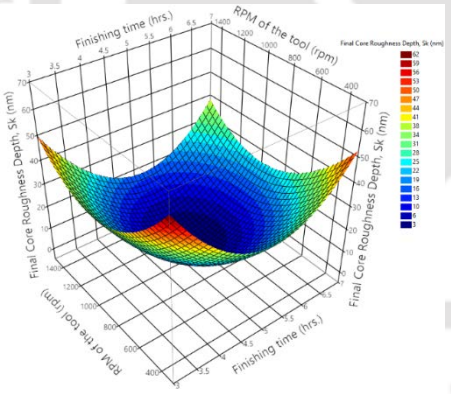

(a)

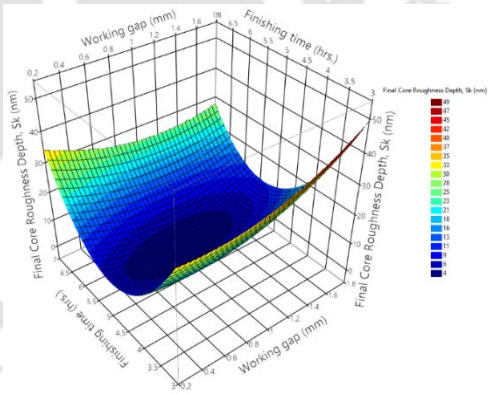

(b)

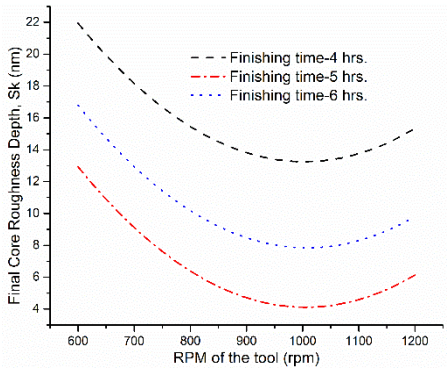

(c)

Fig. 4.7 3D graph showing the combined effect of (a) rpm of the tool & finishing time and (b) finishing time & working gap on final core roughness depth (*Sk*); The effect of (c) rpm of the tool at different finishing time on final *Sk*

4.3.1.4 Effect of Process Parameters on Final *Svk*

For better performance of the Ti alloy implant, final *Svk* values should be high. Effect of tool rpm on final *Svk* is shown in Figs. 4.8(a) and (c). With the increase in tool rpm final *Svk* values start to decrease, however beyond 900 rpm final *Svk* values increases. *Svk* represents the mean depth of the valleys below the core surface. The finishing capability of the abrasive particles grows due to the increase in tool rpm which increases the material removal rate. Due to these, the valley depth decreases resulting in lower final *Svk* values. After 900 rpm, the abrasive particles start to rub the workpiece surface which results in increased valley depth making higher values of final *Svk*.

Effect of working gap on final *Svk* value is shown in Figs. 4.8(a), (b) and (c). Firstly, with the increase in working gap final *Svk* value starts to decrease. The increase in working gap implies an increase in available active abrasive particle in the finishing zone resulting in better finishing of workpiece surface reducing the valley depth. Beyond 1.2 mm working gap final *Svk* value increases. High working gap means a reduction in finishing capability of the abrasive particles. Hence, the valley depth increases. As shown in Fig. 4.8(c), at same working gap the final *Svk* values are different for different tool rpm.

Figure 4.8(b) shows the effect of finishing time on final *Svk* values. Initially, with an increase in finishing time final *Svk* value starts to decrease. The increase in finishing time results in a better surface finish which means reduction in valley depth. After 5 hrs. 30 min final *Svk* value starts to increase with an increase in finishing time. With longer finishing time the surface roughness increases resulting in deeper valleys. Hence, to achieve good Ti alloy implant performance rpm of the tool, working gap and finishing time should be in the range of 1100–1200 rpm, 0.6–0.8 mm and 5 hrs. 30 min–6 hrs., respectively.

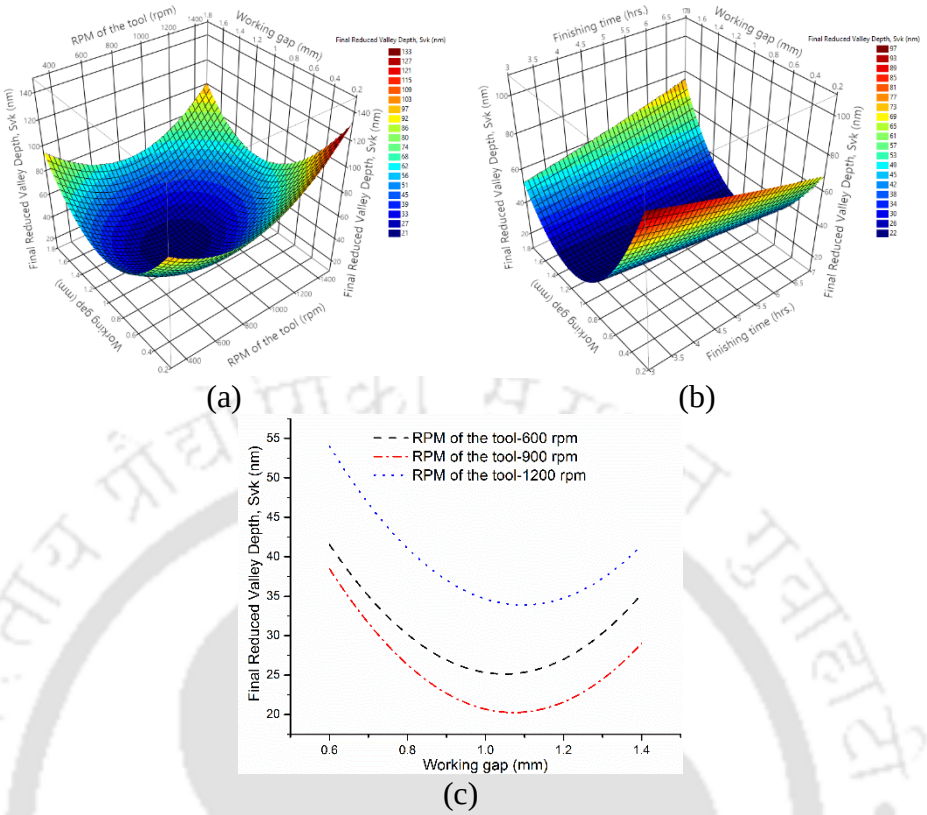

(a) (b)

(c)

Fig. 4.8 3D graph showing the combined effect of (a) working gap & rpm of the tool and (b) working gap & finishing time on final reduced valley depth (*Svk*); (c) The effect of working gap on final *Svk* at different rpm of the tool

4.3.2 Confirmation Tests

After conducting DOE, three confirmation tests are carried out at optimum process parameters (Table 4.5, Sol. no. 1). Average value of the 3D surface parameters from three confirmation tests are considered. Table 4.6 shows the responses from both confirmation test and the regression results at optimum experimental conditions which shows close agreement between them. Also, the % error between them for all the 3D response parameters are less than 8%.

Surface roughness and surface topography of the finished components are analyzed using optical profilometer, FESEM and AFM. Figures 4.9(a) and (b) show the 3D surface topography of initial (before finishing) and final (after finishing) workpiece surfaces, respectively. The initial surface topography shows scratch marks as well as high peaks and deep valleys (Fig. 4.9(a)). The finished surface shows reduced peak height and reduced valley depth (Fig. 4.9(b)). Also, the smoothness of the surface is increased due to the finishing at nanometer level. Figures 4.10(a) and (b) show the initial and final surface roughness profiles of the workpiece, respectively. The initial

surface roughness of the workpiece is 120 nm and it is reduced to very lower value of 20 nm in the final surface roughness profile. The percentage change in surface roughness is 83.33%, which proves that MFAF process is a very efficient finishing method to finish Ti alloy. Figures 4.11(a) and (b) show the FESEM images of the initial and final surface, respectively at 1000X magnification. The FESEM image of the initial surface shows random scratch marks as well as deep valleys. The final surface is smooth and the scratch marks are reduced considerably as shown in Fig. 4.11(b). Figures 4.12(a) and (b) show the AFM images of the initial and final surface topography, respectively. The final surface (Fig. 4.12(b)) has reduced surface undulations than the initial surface (Fig. 4.12(a)).

Table 4.6 Confirmation test at optimum experimental condition

Results from	Experimental conditions			Responses			
	N **(rpm)**	***G*** **(mm)**	***T*** **(hrs.)**	**Final *Sa* (nm)**	**Final *Spk* (nm)**	**Final *Sk* (nm)**	**Final *Svk* (nm)**
Confirmation test	901	0.6	4:30	11.32	15.82	6.51	41.15
Regression Equations				10.82	14.94	6.03	39.98
% Error				4.85	5.98	7.68	4.62

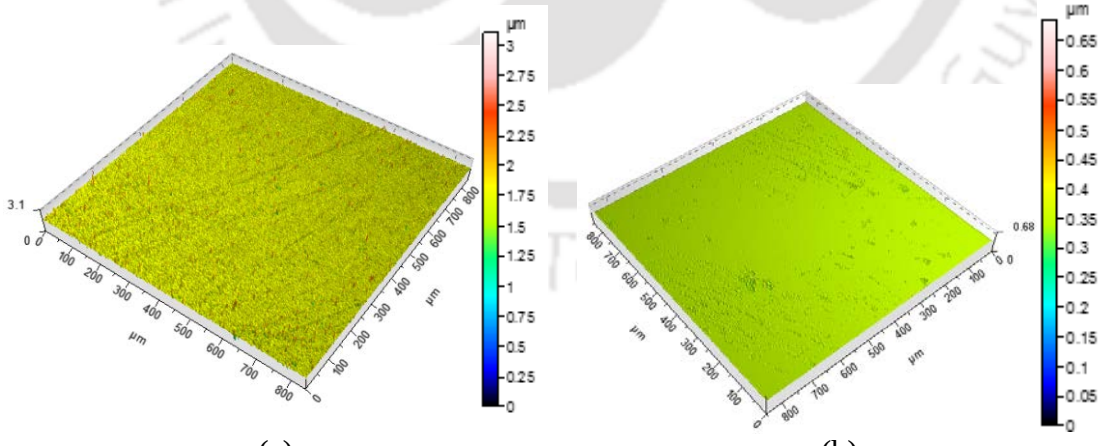

(a) (b)

Fig. 4.9 3D surface topography of (a) initial (before finishing) and (b) final (after finishing) workpiece surfaces at optimum process parameters

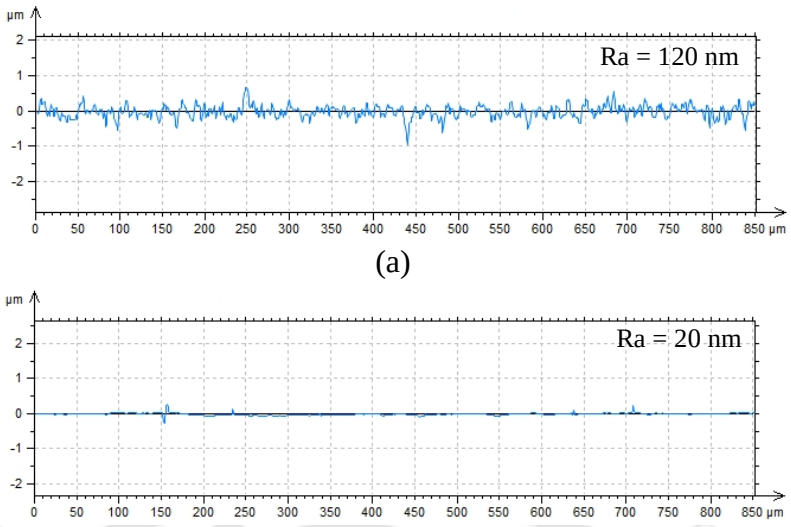

Fig. 4.10 2D surface roughness profiles of (a) initial and (b) final workpiece surface at optimum process parameters

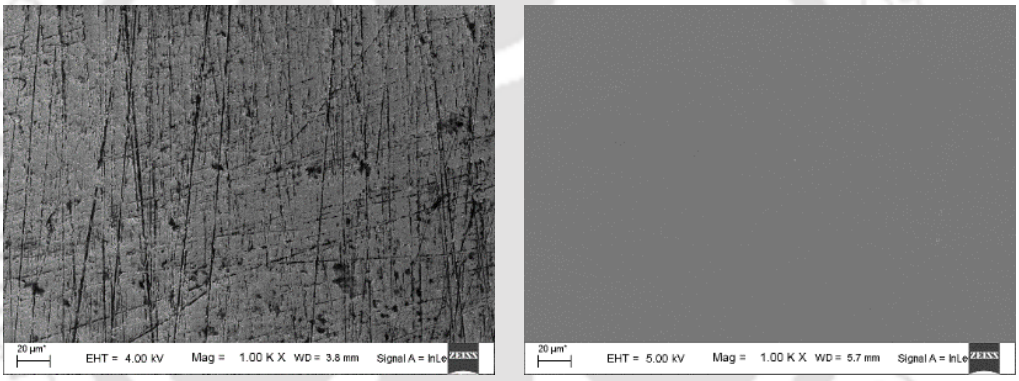

(a) (b)

Fig. 4.11 FESEM images of (a) initial and (b) final workpiece surface at optimum process parameters

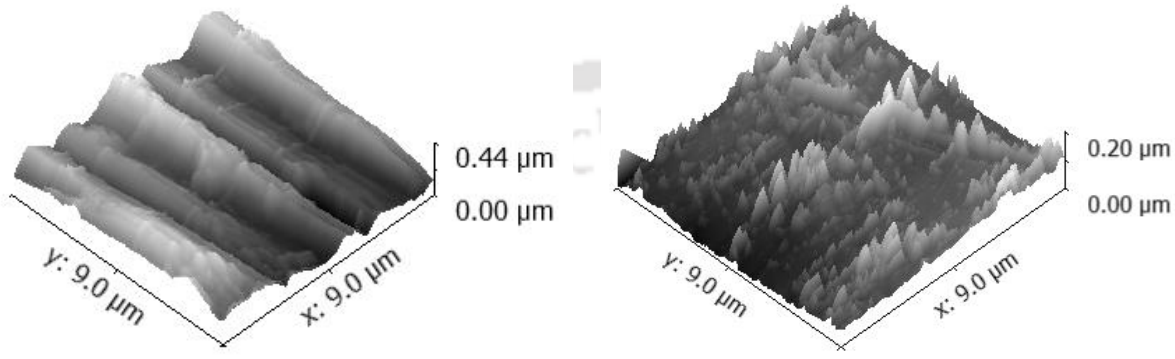

(a) (b)

Fig. 4.12 AFM images of (a) initial and (b) final workpiece surfaces at optimum process parameters

4.4 Summary

The capability of the MFAF process to deliver implant worthy surface roughness and texture is analyzed here by exploring 3D surface roughness parameters. A DOE study consisting 20 experiments are conducted and the output responses are predicted using regressing analysis. After that, an optimization study is carried out to minimize the value of *Sa*, *Spk* & *Sk* and maximize *Svk* for achieving optimum implant surface roughness and surface topography. The optimum values of *Sa, Spk, Sk* and *Svk* are observed as 901 rpm of the tool, 0.60 mm working gap and 4 hrs. 30 min of finishing time. The optimized value of *Sa, Spk, Sk* and *Svk* are 11.32 nm, 15.82 nm, 6.51 nm and 41.15 nm, respectively and their values are more than sufficient against the requirement of the femoral knee joint implant surface. Hence, MFAF process provides nanometer level surface finish along with the necessary surface topography for better wear properties to achieve better performance and longer implant life. From experimental analysis it is observed that for good *Sa* values the rpm of the tool, working gap and finishing time should be in the range of 800–1000 rpm, 0.8–1.2 mm and 4–5 hrs., respectively. For good *Spk* values the rpm of the tool, working gap, and finishing time should be in the range of 700–900 rpm, 0.9–1.2 mm and 4–5 hrs., respectively. For good *Sk* values the rpm of the tool, working gap and finishing time should be in the range of 800–1100 rpm, 0.8–1.2 mm and 4 hrs. 30 min–5 hrs. 30 min hrs. respectively. For good *Svk* values the rpm of the tool, working gap and finishing time should be in the range of 1100–1200 rpm, 0.6–0.8 mm and 5 hrs. 30 min–6 hrs., respectively. Hence, depending upon finishing requirements, the necessary values of the process parameters can be chosen to achieve required surface roughness and topography for implant surface. From experimental investigation, it is concluded that CIP chains break at a high rpm due to the shear thinning nature of MR fluid. Also, at high working gap, the finishing capability of abrasive particles reduces due to the insufficient magnetic field in the finishing zone. Furthermore, after 6 hrs. of finishing time the surface roughness of workpiece increases again due to the plowing of abrasive particle on already finished workpiece surface.

A final confirmation experiment is also conducted at optimized process parameter which shows that the experimental results are nearly same as predicted results obtained from regression equations. After measuring and comparing the surface topographies and roughness profiles of initial and final surface it can be concluded that MFAF process provides nanometer level finishing of Ti alloy with low peaks and shallow valley rather than initial surface.

Chapter 5 Investigation of finishing forces

5.1 Introduction

Force analysis helps in better understanding of the MFAF process. It will provide a better scope to control the finishing process precisely and to gain satisfactory output. The forces involved in MFAF process are broadly categorized as normal force and tangential force as represented in Fig. 5.1. Abrasive particle indent on workpiece due to normal force (F_n). Shearing of indented material happens due to tangential force (F_{tan}) [112]. Normal force and tangential force acts along the normal direction and tangential direction. respectively on an abrasive particle (Fig. 5.1).

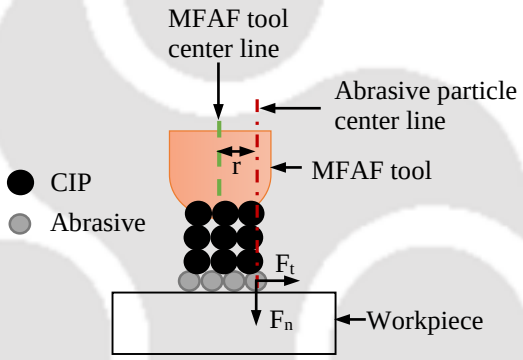

Fig. 5.1 Finishing forces acting on an abrasive particle during MFAF process

In MFAF process, magnetic force is the most dominant force which acts along the normal direction. Hence, magnetic force (F_m) is considered as the normal force. Magnetic levitation force contributes to the material removal process by pushing the abrasive particles towards workpiece surface. Magnetic levitation force depends on the Vol. concentration of nonmagnetic abrasive particles, intensity of magnetization and magnetic field gradient [79]. However, in current scenario, volume concentration of abrasive particles in MR fluid is higher than 3.5 Vol.%. Hence, F_m acting on the CIPs which transmits to abrasive particles in the finishing spot is represented as [94]

$$F_n = F_m = -m_{CIPs} M \nabla B \tag{5.1}$$

Eq. (5.1) is different than magnetic levitation force. Here, m_{CIPs} is mass of magnetic particles i.e. CIPs in the present scenario, M is CIPs magnetization and ∇B is gradient of magnetic flux density. Magnetic property of MR fluid is measured using vibrating sample magnetometer (VSM) and the data obtained from VSM is plotted in Fig. 5.2(a). Now, the relationship between magnetization and magnetic flux density is expressed as

$$B = \mu_0 (M + H) \tag{5.2}$$

where B is magnetic field intensity (T), μ_0 is relative permeability of free space (Wb/Am), M is volume magnetization (emu/m^3) and H is magnetic field strength (A/m). The relationship between volume magnetization (M) and mass magnetization (M_m) is given below.

$$M = \rho_{MR\ fluid} M_m \tag{5.3}$$

where $\rho_{MR\ fluid}$ is density of MR fluid (g/cm^3), M_m is mass magnetization (emu/g). Equations (5.2) and (5.3) are used to obtain BH curve of MR fluid with the data obtained from VSM and it is shown in Fig. 5.2(b).

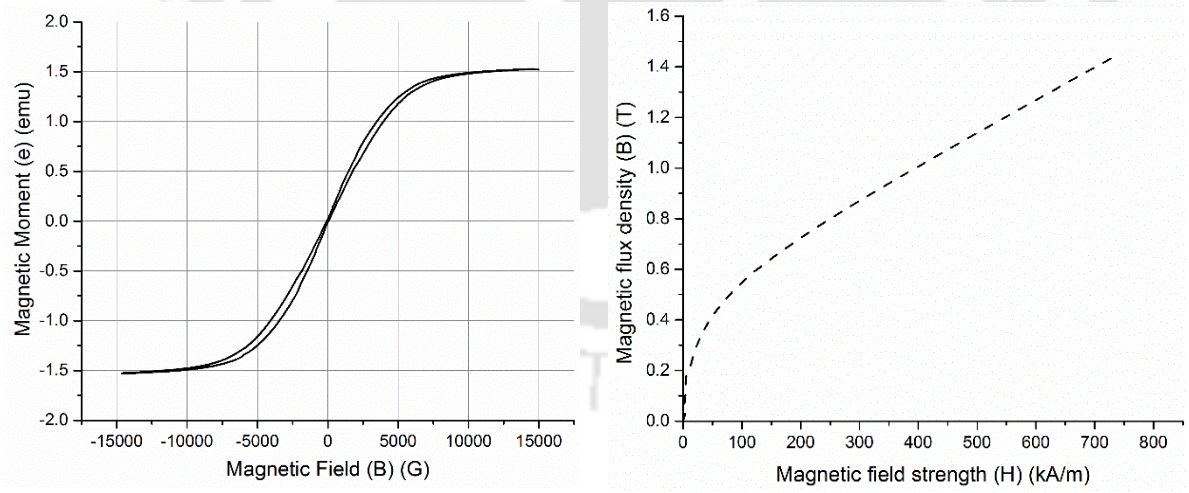

(a) (b)

Fig. 5.2 (a) Magnetic moment vs. magnetic field strength plot from VSM and (b) BH curve of MR polishing medium

MR finishing medium is a uniform blend of CIPs and diamond abrasive particles in acidic base medium. Hence, the density ($\rho_{MR\ fluid}$) of MR fluid is calculated as

$$\rho_{MR\ fluid} = V_{CIP}\rho_{CIP} + V_{DP}\rho_{DP} + V_G\rho_G + V_{HF}\rho_{HF} + V_{HNO_3}\rho_{HNO_3} + V_{DI}\rho_{DI} \tag{5.4}$$

where, V and ρ represents the volume concentration and density of each constituent of MR fluid, respectively. Constituents of MR fluid of Type I (Chapter 3, section 3.2) are carbonyl iron particle (CIP), diamond powder (DP), glycerol (G), hydrofluoric acid (HF), nitric acid (HNO_3) and deionized water (DI). The VSM data is used to obtain a relationship between M_m and B as

$$\begin{aligned} M_m = {} & 2.18X10^{-51}B^{10} - 3.05X10^{-45}B^9 + 1.81X10^{-39}B^8 - 5.95X10^{-34}B^7 + 1.17X10^{-28}B^6 \\ & -1.44X10^{-23}B^5 + 1.07X10^{-18}B^4 - 4.56X10^{-14}B^3 + 9.97X10^{-10}B^2 - 6.26X10^{-6}B + 1.19X10^{-2} \end{aligned} \tag{5.5}$$

Equation (5.5) will be incorporated in Eq. (5.1) to calculate F_n applied on abrasive particles. In the present scenario, a combination of centrifugal force (F_{cfg}) and shear force (F_s) acting on abrasive particle is considered as the tangential force in MFAF process as

$$F_{\tan} = F_{cfg} + F_s \tag{5.6}$$

F_{cfg} acting on an abrasive particle is calculated [108] as

$$F_{cfg} = m\left(\frac{2\pi N}{60}\right)^2 r \tag{5.7}$$

F_{cfg} acting on an abrasive particle depends on MFAF tool rotational speed (N), distance of an abrasive particle from the tool central axis (r) (Fig. 5.1), and mass of an abrasive particle (m). Shear force acting upon abrasive particles depend on MR fluid shear yield stress (τ_y) and projected finishing spot area (A_p) on workpiece surface. An analytical model to calculate shear yield stress of MR fluid under magnetic field is proposed by Ginder et al. [54] by a sub-quadratic power-law model given as

$$\tau_y = \sqrt{6}\phi\mu_0 M_s^{\frac{1}{2}} H_0^{\frac{3}{2}} \tag{5.8}$$

where, ϕ is volume fraction of CIP, μ_0 is permeability of free space, M_s is saturation magnetization and H_o is applied magnetic field in the finishing zone. In the present study, Eq. (5.8) is used to calculate MR fluid shear yield stress applied on the finishing spot. Now, shear force

(F_s) acting on abrasive particle is calculated by multiplying shear yield stress of MR fluid (τ_y) with the projected finishing spot area (A_p) as given below.

$$F_s = \tau_y A_p \tag{5.9}$$

A simulation study is conducted to analyze finishing forces involved in MFAF process and their effect on MFAF process performance. Finishing forces applied on abrasive particles in the finishing spot is calculated from simulation study using finite element analysis (FEA) based software package utilizing equations explained earlier.

In the present investigation, finishing forces on a flat Ti alloy workpiece using a novel developed tool [111] are analysed with the help of simulation and experimental study for better understanding of the process mechanism in MFAF process. The simulation study is carried out to calculate the finishing forces and further corroborated with the validation experiments. After that, a material removal model is simulated using the simulated forces to predict the material dislodgement from workpiece surface. Further, experimental investigation using statistical design of experiments (DOE) is carried out to ascertain the significant process parameters and their influence on finishing forces.

5.2 Simulation Study

Ansys Maxwell® and COMSOL® Multiphysics softwares are used to simulate the MFAF process. The simulation study is conducted to analyze the forces involved in MFAF process. Also, it is used to simulate finishing spot area during MFAF process at different process conditions. The assumptions considered during simulation study are as follows:

- The abrasive particles and CIPs are considered as spherical in shape.
- Simulation study is conducted in static condition implying all components are stationary during simulation.

5.2.1 Governing Equations

The simulation study is carried out in three steps. Initially, Ansys Maxwell® is used to carry out magnetostatic simulation study of MFAF process for getting finishing spot area. At the second

step, COMSOL® Multiphysics is used to model MFAF process to incorporate force analysis with magnetostatic solver. At third step, a material removal model consisting single abrasive particle is carried out using COMSOL® Multiphysics. The force output obtained in the second step is used as input in the third step to calculate material removal. Maxwell equations are solved to carry out the magnetostatic simulation study. In addition to the Maxwell equations, some other equations also have a direct impact on the magnetostatic simulation as given in Eqs. (5.10) and (5.11).

$$\nabla \times \text{applied magnetic field } (H) = \text{current density } (J_e) \tag{5.10}$$

$$\text{Magnetic flux density } (B) = \nabla \times \text{magnetic vector potential } (A) \tag{5.11}$$

Equations (5.12) and (5.13) are solved at the second and third step of the simulation study. Force per unit volume is applied in second step as boundary load (Eq. (5.13)) and in the third step as point load (F_p).

$$-\nabla . \text{ stress } (\sigma) = \text{force per unit volume } (F_v) \tag{5.12}$$

$$F_A = \frac{\text{Total force}}{\text{Finishing spot area}} \tag{5.13}$$

5.2.2 Simulation Set-up

It is obligatory to analyze the influence of magnetic field on MR fluid during finishing to simulate MFAF process. The MR fluid demonstrates non-linear magnetic properties. The BH curve of MR fluid is obtained from VSM data as explained in previous section. After that, the BH curve (Fig. 5.2(b)) data is given as an input in MR fluid material property. A 3D FE study using Ansys Maxwell® is carried out for better understanding of the magnetic field behaviour in MFAF process. However, in COMSOL® Multiphysics two different physics of MFAF process are simulated. Hence, to reduce the complexity and computational time, a 2D study is carried out in COMSOL®. The simulation set-up for both the cases are shown in Figs. 5.3(a) and (b). The dimension of the cylindrical-shaped permanent magnet (Nd-Fe-B of grade N48) is 15X70 mm. Mu-metal is used to construct the magnet holder. Initially, a distance of 1 mm is kept amidst MFAF tool and Ti alloy workpiece to accommodate MR fluid. After conducting the simulation study, a set of validation experiments are carried out at different process parameter conditions. The simulation setup for material removal model is shown in Fig. 5.3(c) which is also solved in

COMSOL® Multiphysics. A point contact is defined between diamond abrasive particle and Ti alloy workpiece surface in the third step of the simulation study.

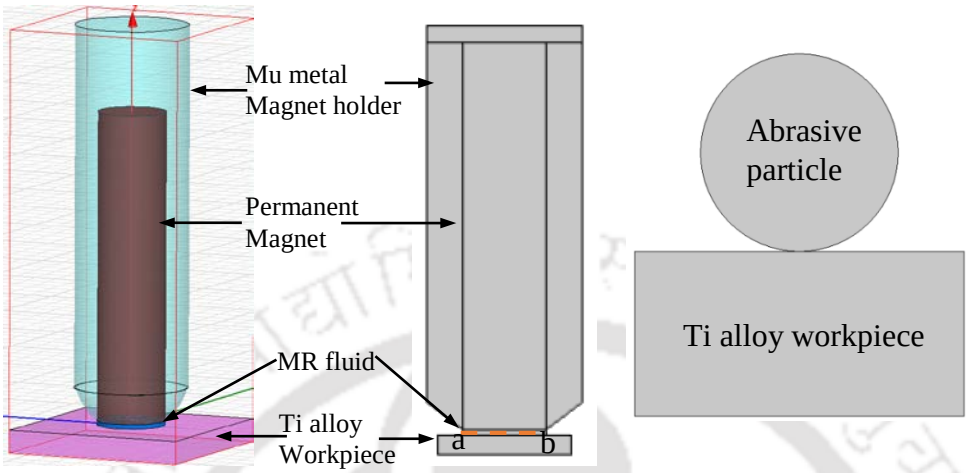

Fig. 5.3 Simulation setups considered in (a) Ansys Maxwell® (1st step) and (b) 2nd & (c) 3rd step of COMSOL® Multiphysics

5.2.3 Boundary Conditions

Magnetic field, solid mechanics and multibody dynamics physics module is used to carry out the simulation. Boundary condition at selected boundaries are considered for each step of simulation study. In the magnetostatic analysis for magnetic field module, the common boundary conditions are as follows

- Magnetic insulation is considered as the boundary condition on the region boundary (Fig. 5.4(a)).
- H field is continuous across the boundaries between two objects where they interface each other.
- H Field is tangential to the outer boundary of each object and magnetic flux cannot cross it.

At 2nd step, the boundary conditions for multibody dynamics module are as follows

- A rotational motion is provided to the both **A** and **B** boundaries of MR fluid brush as shown in Fig. 5.4(b).
- Normal and tangential forces are applied to the **B** boundary between MR fluid brush and workpiece (Fig. 5.4(b)).

At 3rd step, the boundary conditions for solid mechanics module are as follows

- Normal force is applied on the abrasive particle as shown in Fig. 5.4(c).
- Contact pressure between the abrasive particle and workpiece is defined at the **C** boundary (Fig. 5.4(c)).

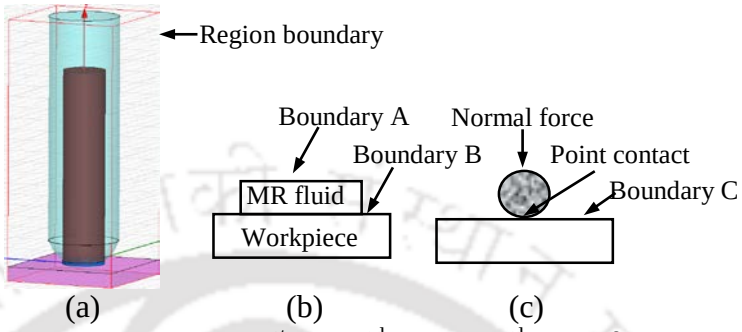

Fig. 5.4 Boundaries considered in (a) 1st, (b) 2nd and (c) 3rd step of simulation study

5.2.4 Mesh Refinement Study

The accuracy of the obtained results in FEA is related to the finite element mesh. The meshing divides the model domain into small elements. The governing equations are defined for each element and then solved. Mesh becomes refined with the reduction in element size resulting in an accurate solution. However, with the decrease in element size, computation time also increases which leads to an impractical solution time. In this sub-section, the convergence of the solution with respect to the mesh size is carried out to find out the optimum mesh size. In the present study free triangular mesh element is used with three different mesh size.

The important parameters for mesh refinement study are given in Table 5.1. The maximum value of F_{tan} acting in the finishing zone on the workpiece surface along with % change in maximum F_{tan} are calculated for each mesh size and are given in Table 5.1. The condition for grid independence is % change in maximum F_{tan} should be within 1% for different mesh size. From Table 5.1, it is observed the % change in F_{tan} is within 1% for one grid level to the more refined one till mesh element size of 2.6. At 2.7 mesh size, the % change becomes more than 1%. According to the condition of grid independence mesh size 2.7 is discarded. The study shows that the convergence of solutions is achieved with different mesh sizes which validate the FEA force modelling of MFAF process. Hence, lowest mesh element size of 2.3 is selected for further study to obtain accurate results. Figure 5.5 shows mesh in the computational domain. The values of process parameters for mesh refinement study is given in Table 5.2.

Table 5.1 Mesh refinement parameters and results

Maximum mesh element size	No of elements	No of degrees of freedom	Maximum F_{tan} on the finishing zone	%change
2.3	18316	37093	1.63136	-
2.4	16634	33725	1.62237	0.55
2.5	15170	30783	1.60994	0.77
2.6	14124	28679	1.59724	0.79
2.7	13338	27103	1.58137	1.07

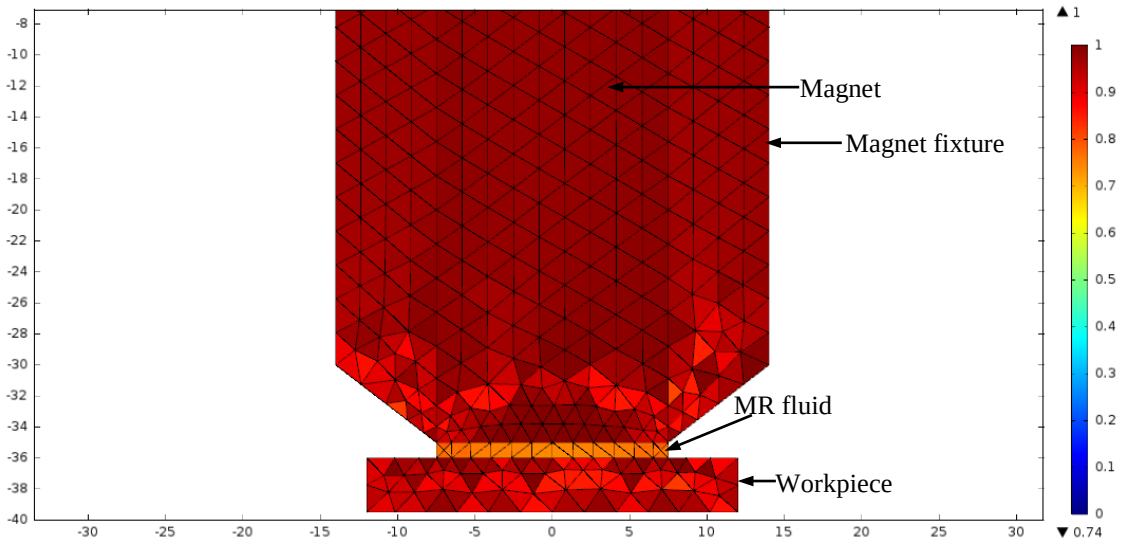

Fig. 5.5 Meshing of the computational domain with element size of 2.3

Table 5.2 The values of process parameters during mesh refinement

Process parameter	Unit	Value
CIP concentration (C)	Vol. %	35
Abrasive concentration (A)	Vol. %	14
Working gap (G)	mm	1
Tool rpm (N)	rpm	900

5.3 Experimental Investigation

To measure forces involved during MFAF process, a 3-axis dynamometer is used during finishing. Dynoware software is used to process and analyze the acquired signal from the dynamometer. Force measurement is started before the MFAF tool came in contact with the workpiece. During finishing, feed is given to the workpiece in X direction while the MFAF tool is rotating with respect to the Z axis. Hence, the main force components acting on the abrasive particles are normal force along Z axis (F_n) and tangential force along X axis (F_{tan}).

A 4-axis vertical milling machine clamps MFAF tool during MFAF process. Ti alloy is considered as the workpiece in the present study. Workpiece is attached with the dynamometer during finishing with the help of a workpiece fixture. The experimental setup is given in Fig. 5.6(a) mentioning all the main components. Figure 5.6(b) shows the graphical presentation depicting finishing process setup during force measurement.

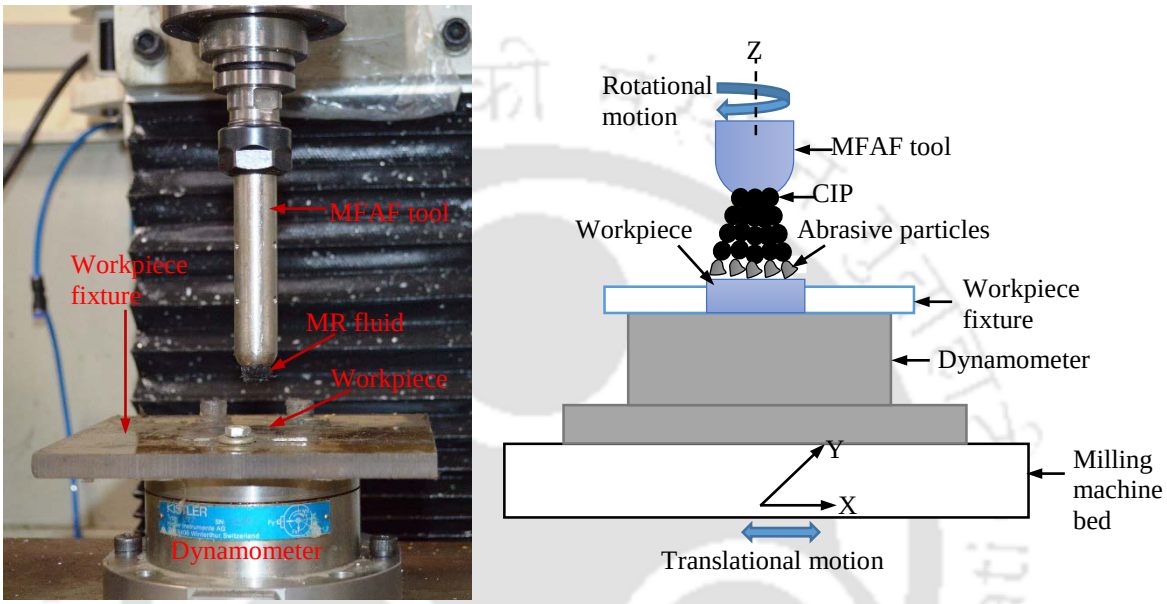

(a) (b)

Fig. 5.6 (a) Pictorial view and (b) graphical presentation of MFAF experimental setup

The finishing process parameters considered during force measurement are CIPs concentration (Vol. %), abrasive concentration (Vol. %) in MR polishing medium, tool rotational speed (rpm) and working gap amidst tool and workpiece (mm) due to their influence on finishing forces [93]. The MR fluid is prepared by mixing CIPs (8 µm), diamond abrasive powder (6 µm), glycerol, HF, HNO_3 and DI [113]. Different combination of MR fluid is prepared by varying volume concentration of CIP and diamond abrasive powder as given in Table 5.4 and the balance is filled with base medium. The base medium is prepared separately by mixing 2 ml glycerol and Kroll's reagent (3 ml HF, 6 ml HNO_3 in 100 ml DI). The range of process parameters is shown in Table 5.3. A statistical DOE analysis considering central composite rotatable design (CCRD) of response surface methodology (RSM) is considered and 30 experiments are conducted. From analysis of variance (ANOVA), influence of each process parameter on finishing forces are analysed and significant process parameters are selected. Regression equation will help to explore the process parameter influence on finishing forces. The plan of experiments along with their responses are shown in Table 5.4 and the experiments are carried out randomly.

Table 5.3 Coded levels and actual values of process parameters

Process parameter	Unit	Levels		
		-1	0	1
CIP concentration (*C*)	Vol. %	30	35	40
Abrasive concentration (*A*)	Vol. %	3.5	7	10.5
Working gap (*G*)	mm	0.6	1	1.4
Tool rpm (*N*)	rpm	600	900	1200

Table 5.4 Plan of experiments through DOE

Std. order	Factors				Responses	
	***C* (vol%)**	***A* (vol%)**	***G* (mm)**	***N* (rpm)**	F_n **(N)**	F_{tan} **(N)**
1	30	3.5	0.6	600	33.65	0.72
2	40	3.5	0.6	600	35.54	1.29
3	30	10.5	0.6	600	11.38	0.84
4	40	10.5	0.6	600	30.48	1.96
5	30	3.5	1.4	600	24.92	0.28
6	40	3.5	1.4	600	30.11	0.65
7	30	10.5	1.4	600	1.51	0.55
8	40	10.5	1.4	600	8.18	1.34
9	30	3.5	0.6	1200	30.25	3.28
10	40	3.5	0.6	1200	38.62	3.48
11	30	10.5	0.6	1200	4.46	3.49
12	40	10.5	0.6	1200	24.37	3.86
13	30	3.5	1.4	1200	20.27	1.19
14	40	3.5	1.4	1200	30.49	1.89
15	30	10.5	1.4	1200	0.41	1.22
16	40	10.5	1.4	1200	10.16	1.94
17	25	7	1	900	3.52	2.77
18	45	7	1	900	40.51	4.35
19	35	0	1	900	35.07	1.47
20	35	14	1	900	15.39	1.93
21	35	7	0.2	900	44.54	1.12
22	35	7	1.8	900	0.74	0.88
23	35	7	1	300	20.89	1.39
24	35	7	1	1500	16.22	6.60
25	35	7	1	900	21.27	2.96
26	35	7	1	900	14.30	1.56
27	35	7	1	900	18.35	1.12
28	35	7	1	900	14.54	1.55
29	35	7	1	900	13.81	1.34
30	35	7	1	900	19.79	1.90

5.4 Results and Discussion

The detail discussion of simulation and experimental results are represented in this section. The measured force data obtained from the dynamometer for experiment No. 20 in Table 5.4 is

represented in Fig. 5.7. The initial constant horizontal line in both Figs. 5.7(a) and (b) show force data before starting of the experiment. Both normal and tangential forces act on workpiece surface after MFAF tool comes in contact with the workpiece which results in a sharp increase in both the forces which decrease further at the end of finishing experiment.

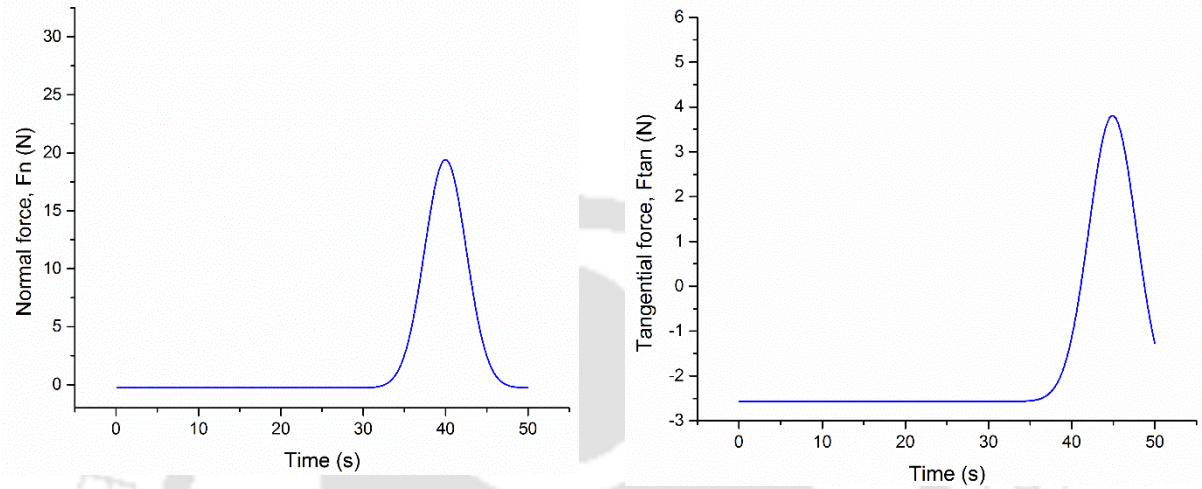

(a) (b)

Fig. 5.7 Measured force data as recorded from dynamometer; (a) Normal and (b) tangential force for Std. order 20 (Table 5.4). Exp. condition: Concentration of CIP 35 Vol.%, abrasive 14 Vol.%, 1 mm working gap and 900 tool rpm

5.4.1 Simulation Study and Validation Results

The results obtained from the simulation study in Ansys Maxwell® is analyzed below. The contour and vector plot of magnetic flux density distribution around MFAF tool are given in Figs. 5.8(a) and (b), respectively. The finishing spot generated in simulation study at different working gap is shown in Figs. 5.9(a), (b) and (c). The finishing spot follows a circular pattern as spherical finishing brush is generated at polishing tool end. The diameter of the finishing spots decreases with increasing working gaps as seen in Fig. 5.9. It is due to lower squeezing force by the polishing tool on MR polishing medium at higher working gap.

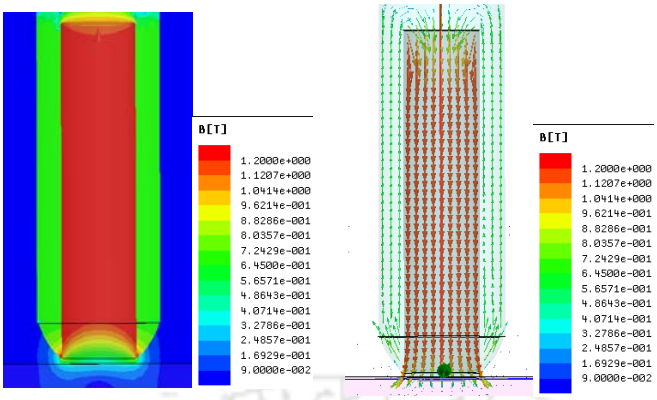

(a) (b)

Fig. 5.8 (a) Contour plot and (b) vector plot of magnetic flux density

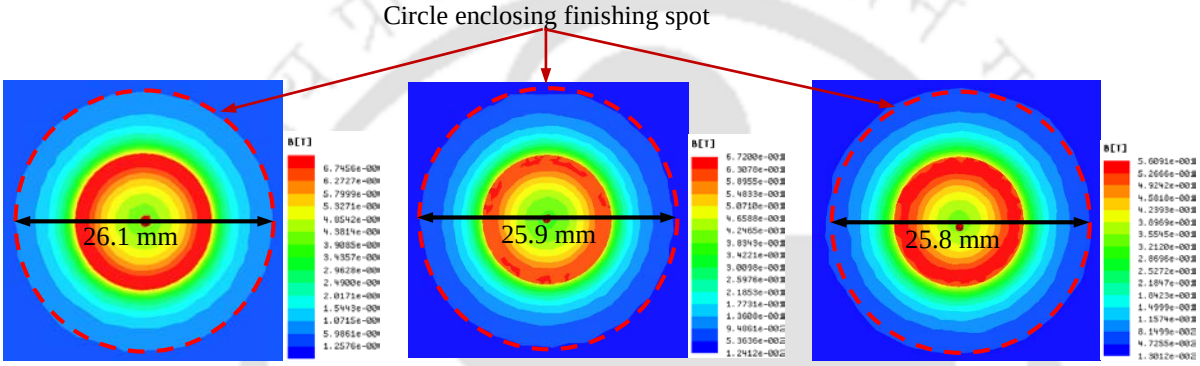

(a) (b) (c)

Fig. 5.9 Simulated finishing spot on workpiece surface at different working gaps (a) 0.6 mm, (b) 1 mm and (c) 1.4 mm

The finishing forces (F_n and F_{tan}) acting on the finishing spot are obtained from the simulation study in COMSOL® Multiphysics. A set of validation experiments are carried out to ratify simulation investigation. The comparison between simulation study and validation experimental results are given in Table 5.5. The forces are measured five times during each experimental condition and an average of five measured forces is considered. The % error between experimental results and simulation results is less than 10% which proves that the result obtained from simulation study is realistic.

After validating simulation study, a material removal model is simulated in COMSOL®. Figure 5.10(a) shows the indentation by a single diamond abrasive particle on Ti alloy workpiece. As shown in the Fig. 5.10(a), at any point of time, a single contact point between abrasive particle and workpiece surface occurs. Indentation of an abrasive particle on the workpiece surface propagates from that single contact point with maximum indentation force. The dislodgement of workpiece by a single abrasive particle along line AB (Fig. 5.10(a)) is plotted in Fig. 5.10(b). For

Sr. 1 in Table 5.5, the maximum displacement is 0.23 µm. Material removal at any experimental condition is predicted from this simulation study of material dislodgement.

Table 5.5 Validation results between experimental and simulation study

Sr. No.	*C* (vol.%)	*A* (vol.%)	*G* (mm)	*N* (rpm)	F_n (N)			F_{tan} (N)		
					Exp.	Sim.*	% error	Exp.	Sim.	% error
1	40	3.5	1	600	30.37	24.97	4.61	1.28	0.88	9.35
2	45	10.5	1.4	1200	21.69	16.89	8.29	3.74	2.84	4.54
3	35	7	0.6	900	23.31	17.71	6.86	1.65	0.95	9.09

Sim.*–simulated

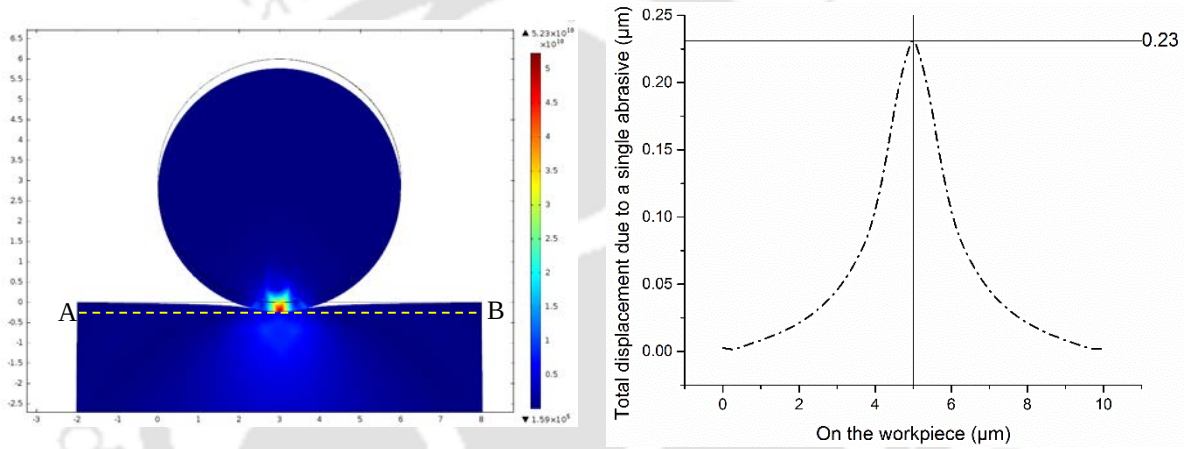

(a) (b)

Fig. 5.10 (a) Indentation by a single diamond abrasive particle on Ti alloy workpiece and (b) dislodgement of workpiece by a single abrasive particle along line AB for Exp. 1 in Table 5.5

Diagrams of the experimental force data (obtained from dynamometer) for the validation of simulation study is provided in Fig. 5.11 for Sr. No. 1, in Table 5.5. Mean value of the experimentally measured force data (Fig. 5.11) is used for the validation of the simulation study (i.e. normal and tangential force in Table 5.5, Sr. No. 1).

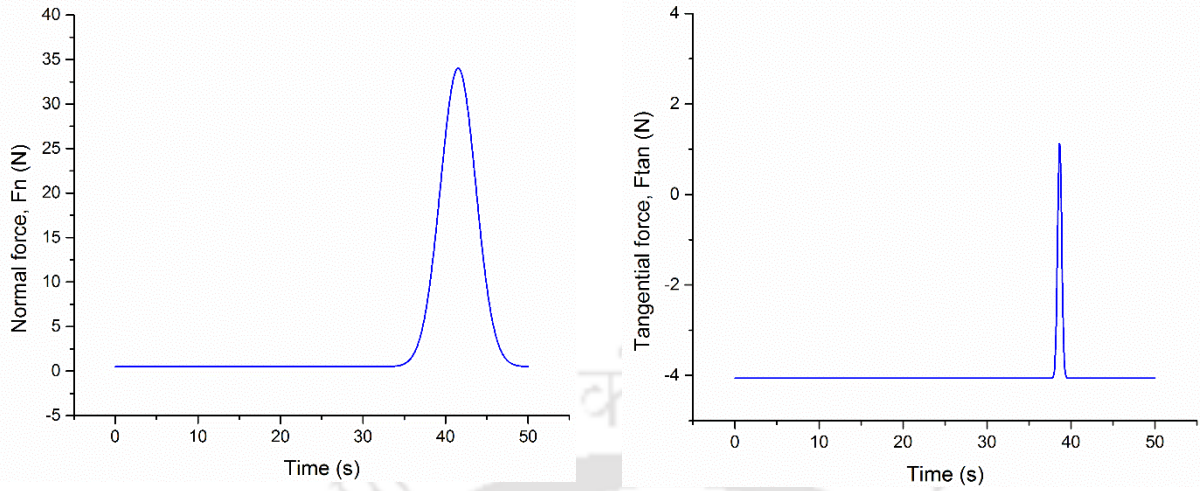

(a) (b)

Fig. 5.11 Measured force data as recorded from the dynamometer; (a) Normal and (b) tangential force for validation experiment (Sr. No. 1 in Table 5.5)

5.4.2 ANOVA Analysis

The ANOVA of experimental results (Table 5.4) along with percentage contribution of each factor are given in Table 5.6. The model *p*-value (Prob>F) for F_n is very small (= 0.0001) and is less than 0.05 (for 95 % confidence interval) indicating model is significant. There is only a 0.01 % chance that the model "F-value" of 8.35 could happen because of noise which implies that the model is significant. As shown in Table 5.6, the significant process parameters in decreasing order of % contribution are abrasive concentration (37.89%), working gap (29.73%) and CIP concentration (24.65%). The model *p*-value (Prob>F) of 0.0013 for F_{tan} indicates that the model is significant. The significant factors in case of F_{tan} in decreasing order of % contribution are tool rpm (51.29%), square of tool rpm (11.57%), working gap (10.24%), square of CIP concentration (6.47%) and square of working gap (6.45%). The regression equations for both the forces F_n and F_{tan} are given below.

$$F_n = 100.44 - 2.43C - 6.92A - 12.79G - 0.03N + 0.11CA - 0.54CG + 6.41\times10^{-4}CN - 0.81AG - 4.50\times10^{-4}AN + 5.19\times10^{-3}GN + 0.04C^2 + 0.15A^2 + 7.56G^2 + 2.10\times10^{-6}N^2 \quad (5.14)$$

$$F_{\tan} = 11.27 - 0.84C + 0.13A + 5.42G - 6.01\times10^{-4}N + 4.16\times10^{-3}CA + 9.93\times10^{-3}CG - 3.55\times10^{-5}CN - 0.01AG - 6.57\times10^{-5}AN - 3.05\times10^{-3}GN + 0.01C^2 - 0.01A^2 - 1.99G^2 + 4.76\times10^{-6}N^2 \quad (5.15)$$

Another important factor to consider during regression analysis is coefficient of determination (R^2) of regression equation which varies between 0 to 1. Higher value of R^2 suggests that the model fits the data better. R^2 value for both F_n and F_{tan} is 0.80 which is good enough for the model to fit the force data well.

Table 5.6 ANOVA for finishing forces (F_n and F_{tan})

Source	F_n			F_{tan}		
	F Value	***p*-value Prob > F**	**Percent contribution**	**F Value**	***p*-value Prob > F**	**Percent contribution**
Model	8.35	**0.0001**		5.38	**0.0013**	
C	29.05	< **0.0001**	24.65	4.45	0.0521	6.13
A	44.65	< **0.0001**	37.89	0.77	0.3945	1.06
G	35.03	< **0.0001**	29.73	7.44	**0.0156**	10.24
N	0.82	0.3793	0.70	37.27	< **0.0001**	51.29
CA	1.60	0.2245	1.36	0.14	0.7120	0.19
CG	0.55	0.4693	0.47	0.01	0.9196	0.01
CN	0.42	0.5226	0.36	0.08	0.7871	0.10
AG	0.59	0.4520	0.51	0.01	0.9189	0.01
AN	0.10	0.7519	0.09	0.13	0.7264	0.17
GN	0.18	0.6771	0.15	3.59	0.0777	4.94
C^2	0.88	0.3624	0.75	4.70	**0.0466**	6.47
A^2	2.74	0.1185	2.33	0.98	0.3379	1.35
G^2	1.16	0.2978	0.99	4.69	**0.0469**	6.45
N^2	0.02	0.8683	0.02	8.41	**0.0110**	11.57
Lack of Fit	4.54	0.0543		1.59	0.3163	

5.4.3 Influence of Process Parameters on Forces

Influence of each process parameters on F_n and F_{tan} are plotted with the help of regression equations (Eqs. (5.14) and (5.15)). The plots are analyzed and discussed to clarify the process mechanism.

5.4.3.1 Normal Force (F_n)

The main component of F_n comes from magnetic force (F_m) in MFAF process as given in Eq. (5.1). Effect of each process parameters on F_n is shown in Fig. 5.12. Influence of abrasive concentration on F_n is very significant (with 37.95% contribution) as perceived from ANOVA (Table 5.6). Rise in abrasive particle concentration in MR fluid results in a reduction in F_n during

finishing as shown in Figs. 5.12(a) and (d). Increasing abrasive concentration implies more number of abrasive particles in the CIP chains in the finishing zone which makes the CIP chains weak resulting reduced MR fluid stiffness. The reduction in MR fluid stiffness causes a decrease in F_n due to weakly formed embedded CIP chains surrounding abrasive particle acting on the workpiece surface.

As shown in Figs. 5.12(a), (b) and (c), with an increase in CIP concentration, F_n acting on the workpiece increases. The rigidity of MR fluid enhances with the increase in CIPs concentration. The column-like structure formed by CIPs in the finishing zone along the magnetic lines of force embedding the abrasive particles farthest from magnetic pole becomes stronger due to the presence of more CIPs. F_m acts upon abrasive particle through the surrounding CIPs chains embedding it. Hence, magnitude of F_m rises with the surge in CIP concentration which leads to higher F_n acting on finishing spot.

Working gap amidst MFAF tool and workpiece plays a vital role on F_n acting on finishing spot. Rise in working gap leads to a reduction in F_n as represented in Figs. 5.12(b) and (c). Increase in working gap implies that the distance between the finishing spot and MFAF tool increases which leads to decreased magnetic flux density on the finishing spot [111]. Hence, magnetic force or F_n acting on finishing spot starts to decline with increased working gap.

According to ANOVA (Table 5.6), the % contribution of tool rpm in case of F_n is small and the change in F_n is almost constant as shown in Fig. 5.12(d). Although, a little decrease in F_n is observed with the increase in tool rpm (Fig. 5.12(d)). At high tool rpm, the CIP chains start to break due to high centrifugal force which leads to the reduction in MR fluid rigidity resulting in decreased F_n. Probably, the normal component of F_{cfg} influence F_n because with the increase in tool rpm normal component of F_{cfg} acting on the finishing spot increases.

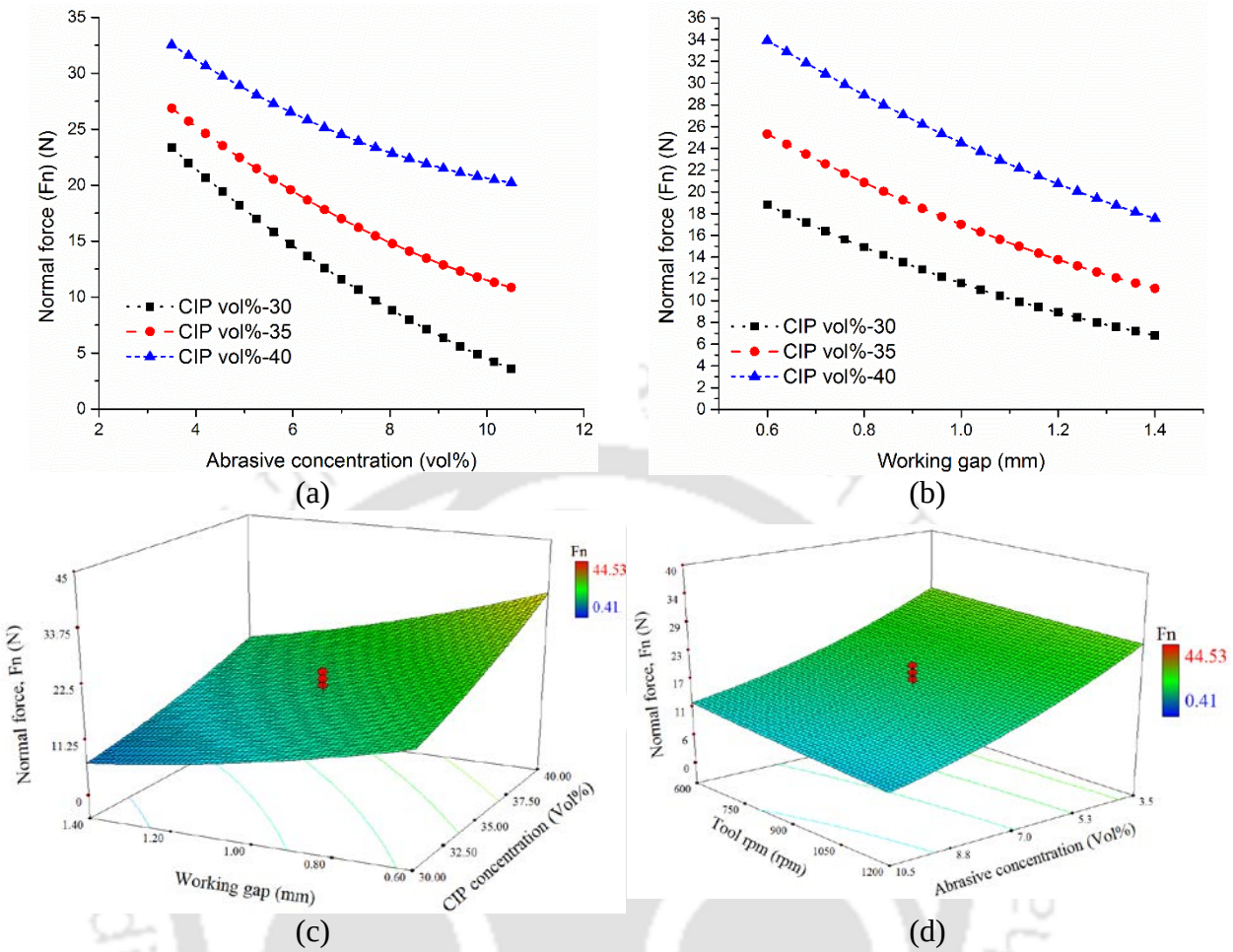

Fig. 5.12 Influence of (a) abrasive concentration and (b) working gap at different CIP concentration on normal force (F_n); 3D plots showing combined effect of (c) CIP concentration & working gap and (d) tool rpm & abrasive concentration on F_n

5.4.3.2 Tangential Force (F_{tan})

F_{tan} acting on the abrasive particles during finishing is presumed to be a combination of F_{cfg} and F_s as given in Eq. (5.6). The most significant process parameters in decreasing % contribution for F_{tan} is tool rpm, working gap, CIP concentration and abrasive concentration according to ANOVA (Table 5.6). F_{tan} increases continuously with the increase in the tool rpm as shown in Figs. 5.13(a) and (c). F_{cfg} increases with the increase in tool rpm as mentioned in Eq. (5.7). The abrasive particles at the end of CIP columnar structure in the finishing zone start moving towards the edge with an increased tool rpm resulting increased F_{tan} on the abrasive particle.

F_{tan} acting on abrasive particles reduces with the rise in working gap as represented in Figs. 5.13(b) and (d). F_s depends on the projected finishing spot area (Eq. (9)) and finishing spot area depends on the working gap. Finishing spot area increases with a decrease in working gap due to

the squeezing of MR fluid in the finishing zone. Finishing spot area increases due to a decrease in working gap is supported by the simulation study (Fig. 5.9). Also, increased working gap reduces shear stress applied on the abrasive particles due to the dependency of shear stress on the applied magnetic field (Eq. (5.8)). Hence, increase in working gap results in a reduction of magnetic force on the finishing spot ensuing reduced shear stress which prompts to a reduction in shear force. Therefore, reduction in F_{tan} is observed with increasing working gap due to decreasing F_s.

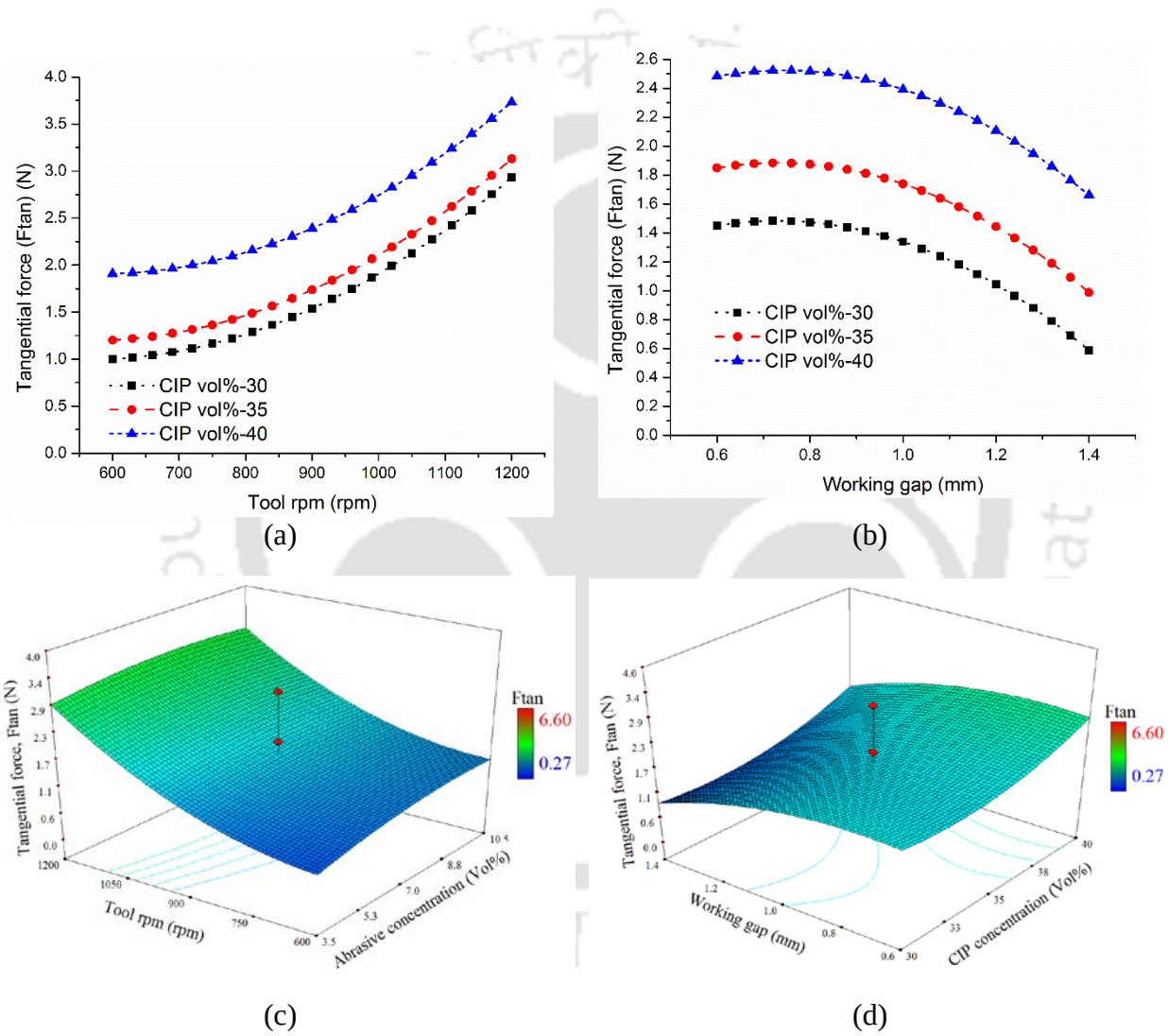

Fig. 5.13 Influence of (a) tool rpm and (b) working gap at different CIP concentration on tangential force (F_{tan}); 3D plots showing combined effect of (c) abrasive concentration & tool rpm and (d) CIP concentration & working gap on F_{tan}

Shear stress is proportional to the CIP volume concentration (Eq. (5.8)). Rise in CIP volume concentration increases MR fluid stiffness resulting in enhanced MR fluid shear stress. Also, increased CIP concentration increases available magnetic field in the finishing spot. It causes

an increase in MR fluid shear stress. Hence, with increased CIP concentration, F_{tan} also increases as shown in Figs. 5.13(a), (b) and (d).

As shown in Fig. 5.13(c), F_{tan} increases initially (a bit) and further decreases with a rise in abrasive concentration. Total F_{cfg} acting on all abrasive particles rises with the increment in abrasive concentration due to the increase in total abrasive mass (Eq. (5.7)). However, with continuous increase in abrasive volume concentration, the columnar structure of CIPs embeds more abrasive particle resulting weaker structure which leads to decreased MR fluid shear stress. It results in decreased F_{tan}.

5.5 Summary

The analysis of finishing forces involved in the present MFAF process is carried out for better understanding and precise control of the process. Simulation study of MFAF process concerning finishing forces is carried out in two FEA based softwares. Validation experiments are conducted to substantiate the simulation study. The simulation results obtained from Ansys Maxwell® is incorporated in the COMSOL® Multiphysics for force simulation. The validation experimental investigation shows minor variation between experimentally measured and simulated forces. Hence, the conducted simulation study can be used to simulate the MFAF process precisely and efficiently. A material removal model for a single abrasive particle is also simulated with known finishing force values.

A statistical DOE analysis is conducted to evaluate the significance of each process parameter and their % contribution on normal and tangential forces. Significant process parameters in case of F_n are abrasive concentration with 37.89% contribution, working gap with 29.73% contribution and CIP concentration with 24.65% contribution. The significant factors in case of F_{tan} are tool rpm (51.29%), square of tool rpm (11.57%), working gap (10.24%), square of CIP concentration (6.47%) and square of working gap (6.45%). The influence of each process parameter on finishing forces in the design space is explored with the help of regression equation obtained from the statistical analysis. After analysis, it shows that F_n acting on the abrasive particles surges with rise in CIP concentration. Although, surge in abrasive particle concentration, working gap and tool rpm results in a reduction in F_n. F_{tan} increases continuously with the rise in

the tool rpm, CIP concentration and decrease in working gap. Initially, F_{tan} increases little bit with a rise in abrasive concentration however it decreases with additional abrasive concentration.

Chapter 6 Finishing of freeform surface of femoral part of prosthetic knee joint

6.1 Introduction

A freeform surface is created from an array of control points along with a mathematical model to define the surface. Freeform surfaces are widely used in automotive, aerospace, medical and other industries. Finishing of freeform surface is a very difficult task due to its complex nature. Freeform surfaces are adopted to a great degree in prosthetic implant surfaces in medical industry. Femoral component of knee joint implant is an example of freeform surface. Employing manual finishing and semi-automated finishing to polish femoral knee implant is time consuming, labor intensive and less uniform. The issues of manual finishing are resolved using advanced nanofinishing processes. Many advanced finishing processes are proposed and developed to finish femoral knee implants. Performance and life of knee implants largely depend on the surface finish [114]. Low surface roughness of femoral knee implant causes less friction during relative motion of the femoral component resulting reduced wear and mixing of wear related debris in blood stream [115,116]. According to ISO 7207-2:2011 [102], the surface roughness of femoral knee implant should be in the nanometer range. Commercially grinding, drag finishing, vibratory finishing systems etc. are used to finish metallic femoral knee implants. Industrial robots are also employed for grinding of femoral knee implant [117]. To finish femoral knee implant with better surface roughness, different methods are proposed by researchers. Hilerio et al. [116] proposed a mechanochemical method (MCM) to achieve required surface finish of femoral knee implant made of CoCrMo. The MCM process is carried out in different stages using different abrasive-bands at each stage [118]. Charlton and Blunt used a 7 axis Zeeko CNC polishing machine to attain required surface finish and form on CoCr alloy femoral knee implant. They proved that this process can be used to generate nanometer level surface topography [119].

Magnetorheological fluid based finishing processes are also employed to finish femoral knee implants with better control of finishing forces than previously mentioned processes. Sidpara and Jain did nanofinishing of titanium femoral knee implant using magnetorheological fluid based

finishing (MRFF) process [84]. Later, femoral knee implant made of stainless steel is finished using rotational-magnetorheological abrasive flow finishing (R-MRAFF) process to improve surface topography with less finishing time than MRFF process [120].

Magnetic abrasive finishing (MAF) is also employed to finish femoral knee implants at nanometer level surface roughness [85]. All these processes provide nanometer level finishing on the femoral knee implant. However, the uniform surface roughness along the curvature of the femoral knee implant is not achieved by the previous processes. Hence, to obtain an uniform surface roughness along the curvature of femoral knee implants, a novel developed tool [111] in magnetic field assisted finishing (MFAF) process is employed.

In the present chapter, the ability of the MFAF tool to provide uniform finishing along the curvature of freeform surface of a femoral knee implant is analyzed. Surface topography and surface roughness of workpiece surfaces at different positions along the curvature before and after finishing are investigated to find out the MFAF tool capability. A statistical design of experiments (DOE) analysis is carried out for better understanding of the process mechanism and to increase the process performance.

6.2 Experimental Investigation

Femoral knee implant made of Ti alloy of grade 5 is finished using newly developed MFAF tool [111]. Finishing of a femoral knee implant is a difficult task due to its complex freeform nature. To finish freeform surface efficiently the MFAF tool is particularly made. The experimental setup is represented in Fig. 6.1. A 4-axis CNC milling machine is used to hold the MFAF tool. A rotational motion to the MFAF tool is imparted during finishing with respect to the Z axis (Fig. 6.1). Workpiece is held with the help of a specially designed workpiece fixture. The developed workpiece fixture is attached to the rotary chuck and it rests on a vertical stand attached to the milling machine bed. A rotational motion is provided to the workpiece through the rotary chuck using computer console.

A toolpath is generated using sprutcam® software to uniformly finish femoral knee implant. Schematic diagram of the tool positions at different time during a finishing cycle are shown in Fig. 6.2. The toolpath is generated in such a way that the MFAF tool is perpendicular to the workpiece

surface as shown in Fig. 6.2. However, due to the complex geometry of the workpiece surface, in some positions the perpendicular position of the tool may not be maintained with a 4-axis CNC machine.

Volume concentration of CIP, abrasive and base medium is given in Table 6.1 [112]. Two types of experimental investigations are conducted on femoral knee implant. The first set of experiments are carried out to analyze MFAF tool capability to achieve uniform surface finish along the curvature of freeform surface. The second set of experiments are conducted to find out the influence of different process parameters on femoral knee implant and to obtain minimum surface roughness with optimum value of process parameters.

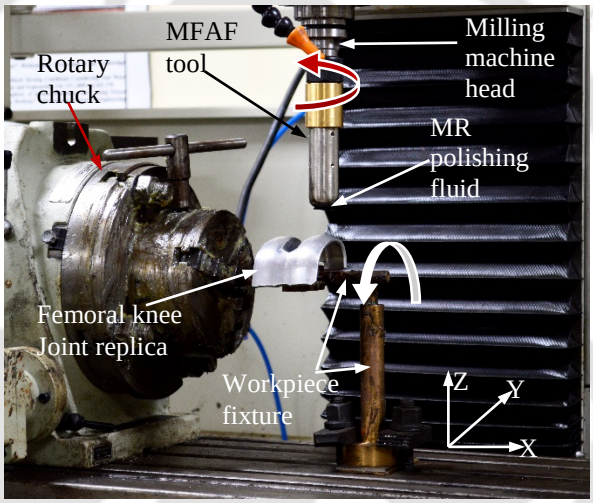

Fig. 6.1 MFAF experimental set-up to finish femoral knee implant

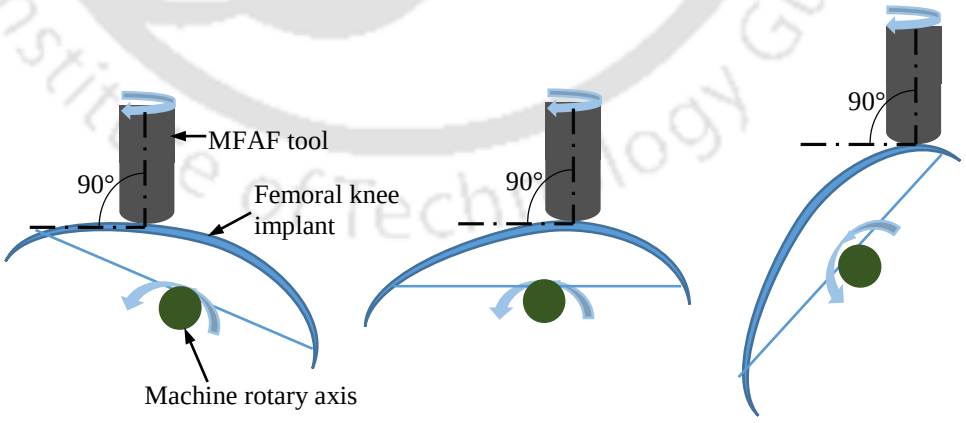

(a) (b) (c)

Fig. 6.2 Movement of femoral knee implant with respect to MFAF tool and their relative positions (a) at the start, (b) in between and (c) at the end of finishing cycle

6.2.1 Effect of Surface Curvatures (1st Set of Experiments)

The MFAF tool capability is analyzed to achieve uniform finishing along the curvature of the femoral component surface during 1st set of experiments. The entire curvature is divided equally into five different sections using CAD software as shown in Fig. 6.3(a). The surface roughness at those five different positions is analyzed after finishing. Figure 6.3(b) displays the finishing spot generated using MFAF tool with 30 mm spot diameter. The curvature length of each section in Fig. 6.3(a) is less than 30 mm so that overlapping of the finishing spot occur which will render uniform finishing of each position. The experimental conditions considered during finishing is given in Table 6.1. After the finishing of femoral knee implant, the surface roughness and surface topography at each positions are studied.

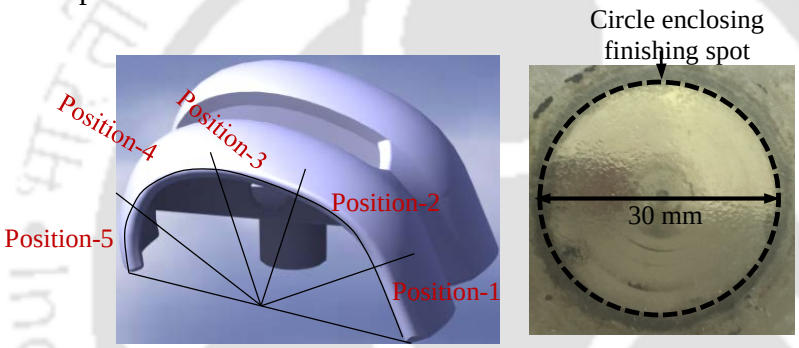

Fig. 6.3 (a) Positions considered to evaluate the effect of surface curvatures of femoral knee implant; Position 1 (0°–36°), position 2 (37°–73°), position 3 (74°–107°), position 4 (108°–138°), position 5 (139°–180°) and (b) finishing spot using MFAF tool

Table 6.1 Process parameter conditions

Process parameters	Value
Tool rpm	900 rpm
Working gap	0.6 mm
Rotary chuck rpm	5 rpm
CIP concentration	45 Vol. %
Diamond abrasive concentration	7 Vol. %
Base medium concentration	48 Vol. %

6.2.2 Design of Experiments (2nd Set of Experiments)

Statistical design of experiment (DOE) based on response surface method (RSM) is carried out to optimize the MFAF process parameters during finishing of freeform surface of femoral knee implant. Relationship between input process parameters and output response is established using regression equation and is used to evaluate the influence of key process parameters on surface

roughness of femoral knee joint implant. Principle objective of this statistical analysis is to optimize input process parameters to achieve minimum surface roughness. Central composite rotatable design (CCRD) of RSM is selected due to equal variance prediction in total design space. Three key process parameters are as listed in Table 6.2. The experiments are conducted randomly as listed in Table 6.3.

Table 6.2 Coded levels and actual values of process parameters

Parameters	**Unit**	**Levels**		
		-1	**0**	**1**
Rotational speed of the tool (*N*)	rpm	800	1000	1200
Feed rate (*F*)	mm/min	10	15	20
CIP concentration (*C*)	Vol. %	35	40	45

After completing 20 experiments (Table 6.3), the significance of process parameters in MFAF process is explored using analysis of variance (ANOVA). Further, an optimization study is executed to find out optimum process parameters value to achieve a minimum final area-surface roughness (*Sa*). Later, confirmation tests are conducted with optimized process parameter values.

Table 6.3 Plan of experiments through DOE

Sl. No.	***N* (rpm)**	***F* (mm/min)**	***C* (vol.%)**	**Final *Sa* (nm)**
1	1200	10	35	72.4
2	1000	15	40	21
3	800	10	35	91.8
4	1000	15	40	34
5	800	20	35	80.9
6	1200	20	45	31.6
7	800	10	45	65.2
8	1200	20	35	65
9	1000	15	30	34
10	1000	15	50	29.9
11	800	20	45	56.5
12	1000	15	40	35
13	1300	15	40	50.4
14	1200	10	45	44.3
15	1000	15	40	20
16	1000	6	40	61.6
17	1000	24	40	70.9
18	1000	15	40	20.6
19	1000	15	40	36
20	600	15	40	96.1

6.3 Results and Discussion

The results obtained from two different sets of experimental studies are discussed in this section.

6.3.1 Effect of Surface Curvature on Surface Roughness and Surface Topography

Table 6.4 shows the initial and final surface roughness values at each position. The standard deviation between the initial surface roughness values is reduced from 34.21 to 19.23 in the finished surfaces. Hence, the variation in the final surface roughness is reduced after finishing with MFAF tool. Hence, the MFAF tool can provide nearly uniform finishing at different surface curvatures of femoral knee implant.

Table 6.4 Initial and final *Ra* at different positions

Position	Initial *Ra* (nm)	Final *Ra* (nm)	% change in *Ra*
1	170	60	64.71
2	140	40	71.43
3	100	20	80
4	160	50	68.75
5	190	70	63.16
Std. dev.	34.21	19.23	

Figure 6.4 shows the initial and final surface roughness (*Ra*) plot considering "t-distribution with 95% confidence level" at different positions along the surface curvature of femoral knee implant. The scatter bars are plotted considering "t-distribution with 95% confidence level". This method is considered due to the small experimental data. It is calculated based on the mean of normally distributed dataset. From Table 6.4, it is observed that % change in surface roughness is highest in position 3 (Fig. 6.3(a)) and its lowest value is observed in positions 1 and 5. During finishing at positions 1 and 5 the MFAF tool is not properly perpendicular with the implant surface due to its highly complicated curvature which results in low % change in surface roughness. This leads to higher surface roughness in positions 1 and 5 than other positions. This occurs due to the restriction imposed by 4-axis CNC machine. This problem can be solved by using 5-axis CNC machine. Hence, MFAF tool provides almost uniform surface roughness over entire implant surface.

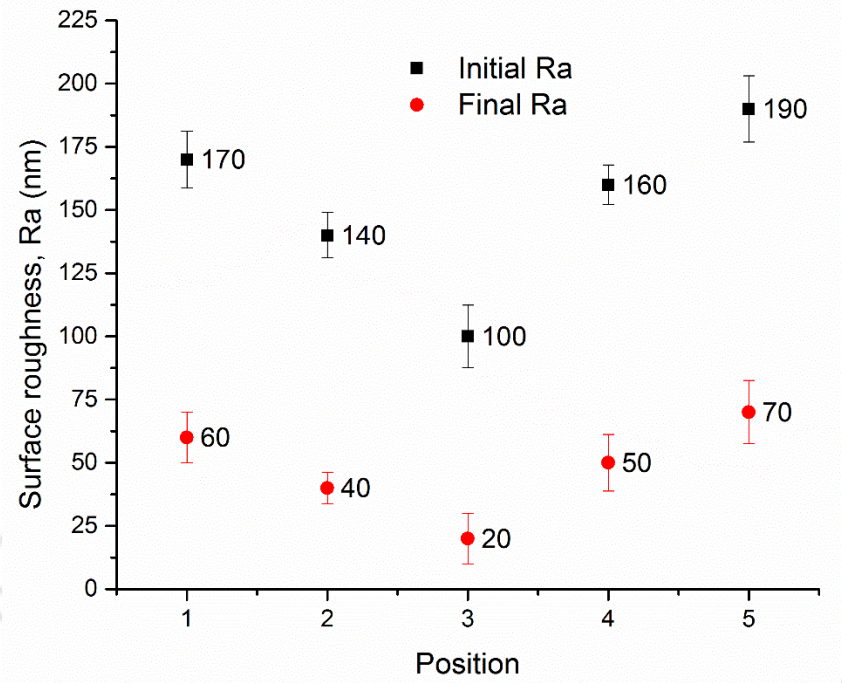

Fig. 6.4 Initial and final surface roughness (*Ra*) plot considering "t-distribution at 95% confidence level" at different positions along the surface curvature of femoral knee implant

To examine MFAF tool capability to achieve uniform finishing at different curvatures of implant surface, the surface topography and surface roughness at different positions (Fig. 6.3(a)) are compared before and after finishing. Figures 6.5–6.9 show 3D surface topographies and surface roughness profiles for each curvature (Fig. 6.3(a)) positions (a) before and (b) after MFAF process. All finished 3D surface topographies show lesser abrasion marks than their initial surface topographies. Also, the number of high peaks and deep valleys are reduced in the (b) final surface from their (a) initial one as observed in the surface roughness profiles (Figs. 6.5–6.9) at different positions.

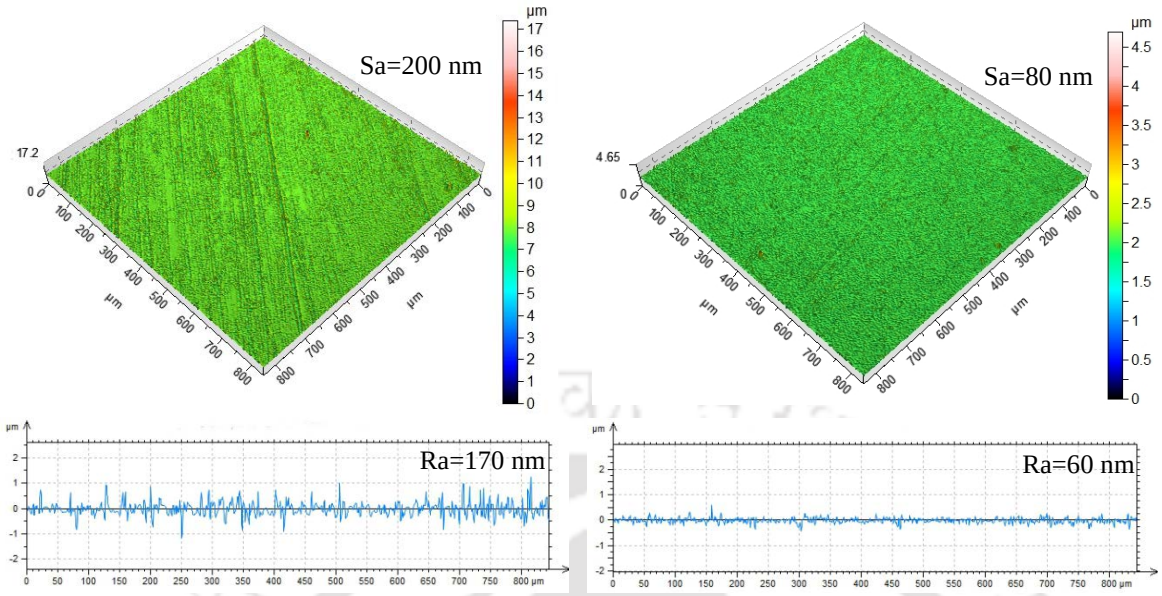

Fig. 6.5 3D surface topographies and surface roughness profiles of femoral knee joint implant at position 1 (a) before and (b) after MFAF process

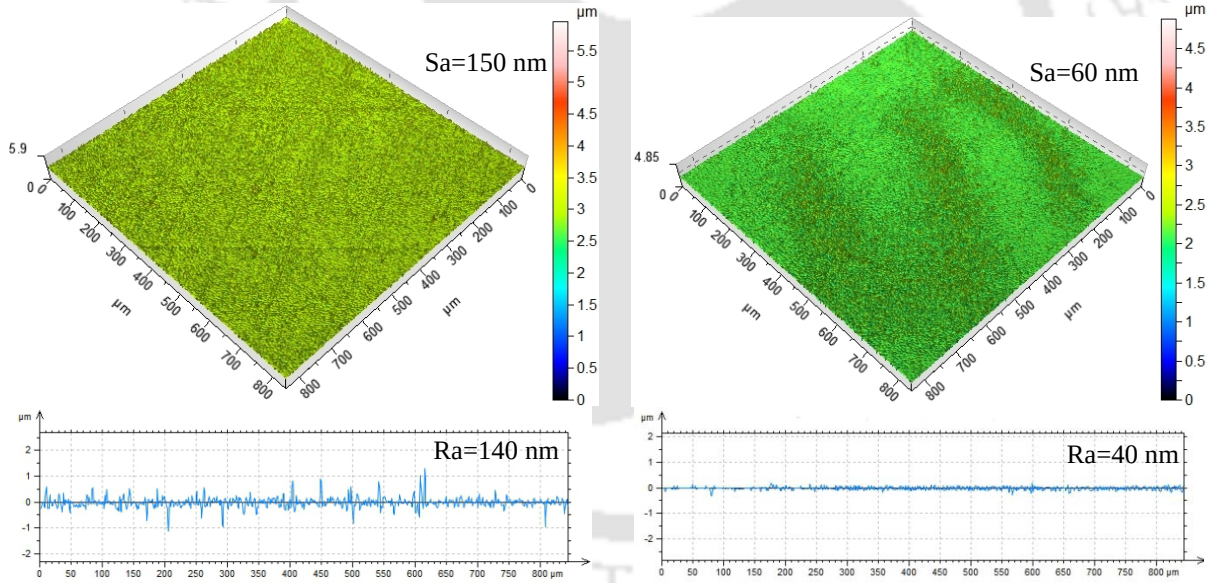

Fig. 6.6 3D surface topographies and surface roughness profiles of femoral knee joint implant at position 2 (a) before and (b) after MFAF process

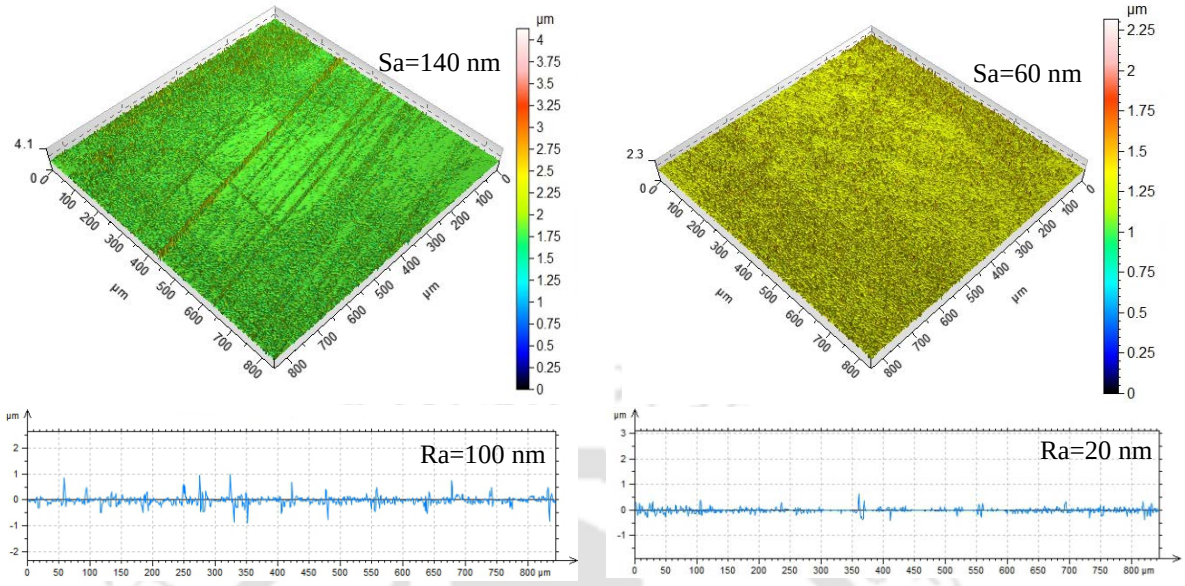

Fig. 6.7 3D surface topographies and surface roughness profiles of femoral knee joint implant at position 3 (a) before and (b) after MFAF process

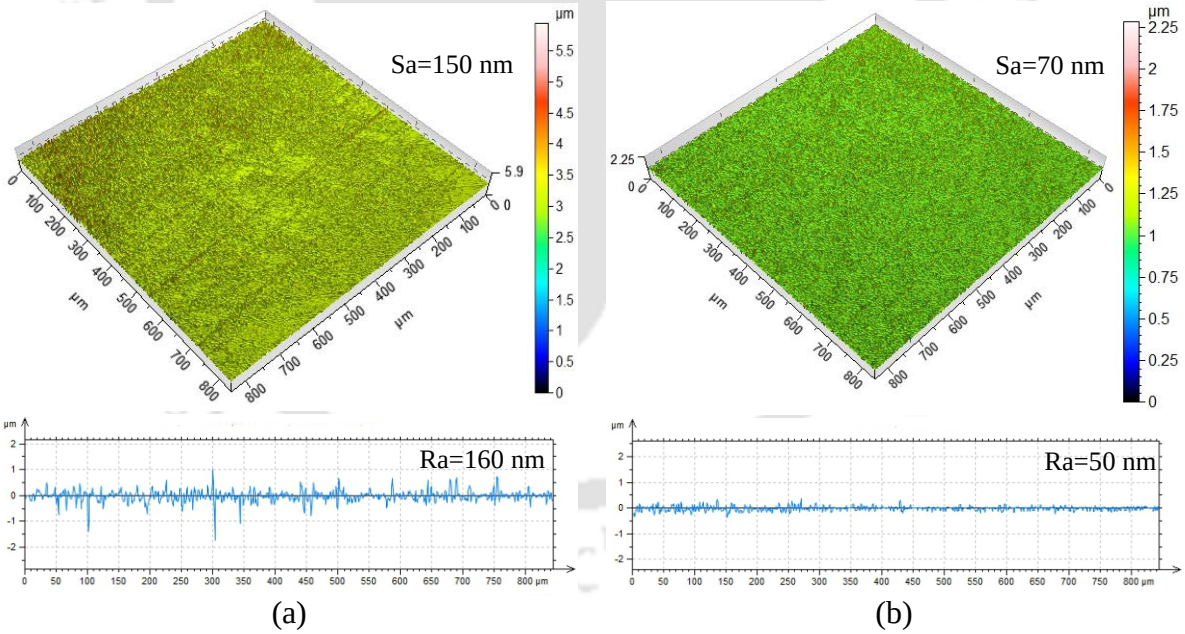

Fig. 6.8 3D surface topographies and surface roughness profiles of femoral knee joint implant at position 4 (a) before and (b) after MFAF process

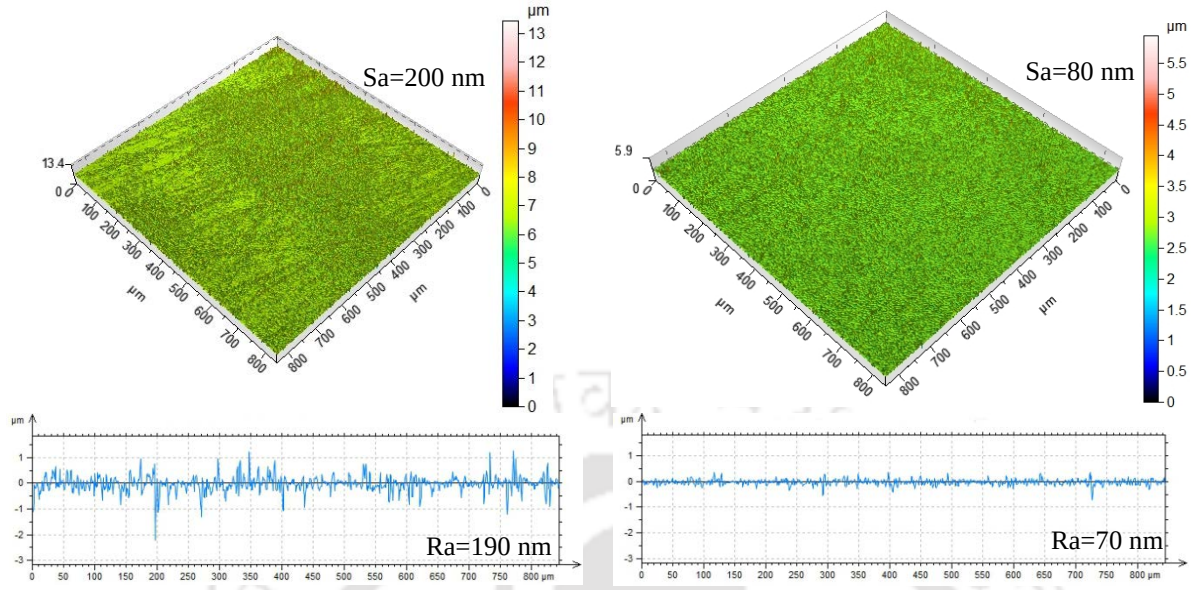

Fig. 6.9 3D surface topographies and surface roughness profiles of femoral knee joint implant at position 5 (a) before and (b) after MFAF process

6.3.2 Analysis of DOE Study

The ANOVA (Table 6.5) of final area surface roughness (*Sa*) is carried out based on experimental results given in Table 6.3. The model *p*-value of 0.0039 is lower than 0.05 for 95% confidence level implies that the model is significant. The most significant process term is square of tool rotational speed having 43.21% contribution on *Sa*. The 2nd and 3rd significant terms are square of feed rate and CIP concentration having 35.15% and 10.37% contribution, respectively. This model has insignificant "Lack of fit". The response surface model for final *Sa* obtained from regression analysis is given as

$$Sa = 685.75 - 0.74N - 15.51F - 5.98C - 6.25\times10^{-5}NF - 1.31\times10^{-3}NC - 0.01FC + 3.75\times10^{-4}N^2 + 0.53F^2 + 0.07C^2 \quad (6.1)$$

The coefficient of determination (R^2) of Eq. (6.1) is 0.85 which shows good fitting of the experimental results with the regression equation. An optimization study based on Derringer and Suich's algorithm [109] is carried out. The optimization study maximizes the desirability function. The values of optimum process parameters to obtain minimum final *Sa* is given in Table 6.6.

Table 6.5 ANOVA for final area surface roughness (*Sa*)

Source	F-value	*p*-value (Prob > F)	Percent contribution
Model	6.37	**0.0039**	
N	5.33	**0.0436**	9.65
F	0.23	0.6424	0.42
C	5.73	**0.0377**	10.37
NF	1.97×10^{-4}	0.9891	0.00
NC	0.087	0.7744	0.16
FC	7.56×10^{-3}	0.9324	0.01
N^2	23.87	**0.0006**	43.21
F^2	19.42	**0.0013**	35.15
C^2	0.57	0.4667	1.03
Lack of Fit	4.02	0.0765	

Validation experiments are carried out at optimum process parameter condition (Table 6.6, Sl. no. 1). Average value of final *Sa* from three validation experiments are considered. The comparative results from optimization study and validation experiments are shown in Table 6.7. The results are in close agreement as % error between them is 6.93% which is acceptable.

Table 6.6 Results of optimization study

Sl.	*N* (rpm)	*F* (mm/min)	*C* (Vol. %)	Final *Sa* (nm)	Desirability	
1	**1062.16**	**15.37**	**45.00**	**21.71**	**0.978**	Selected
2	1066.14	15.55	45.00	21.73	0.977	
3	1102.55	14.82	45.00	22.49	0.967	

Table 6.7 Confirmation test at optimum experimental condition

Results from	Process parameters			Final *Sa* (nm)	% Error
	N (rpm)	*F* (mm/min)	*C* (Vol. %)		
Confirmation test	1062	15	45	23.21	6.93
Optimization study				21.71	

Figures 6.10(a) and (b) represent 3D surface topographies of initial (before finishing) and final (after finishing) workpiece surfaces, respectively. The initial surface topography shows deep scratch marks as well as high peaks and deep valleys (Fig. 6.10(a)). The finished surface (*Sa* of 23.21 nm in Fig. 6.10(b)) becomes smoother with no visible scratch marks. Figures 6.10(a) and (b) also show initial and final surface roughness profile of the workpiece, respectively. Initial surface roughness (*Ra*) is 170 nm and it is reduced to a very lower value of 10 nm (*Ra*) in final

surface roughness profile. As represented in Fig. 6.10(a), a big variation between peaks and valleys is observed in initial surface profile. This variation is reduced extensively in the final surface profiles as represented in Fig. 6.10(b). All 3D surface roughness parameters of the finished surface (Fig. 6.10(b)) is provided in Table 6.8.

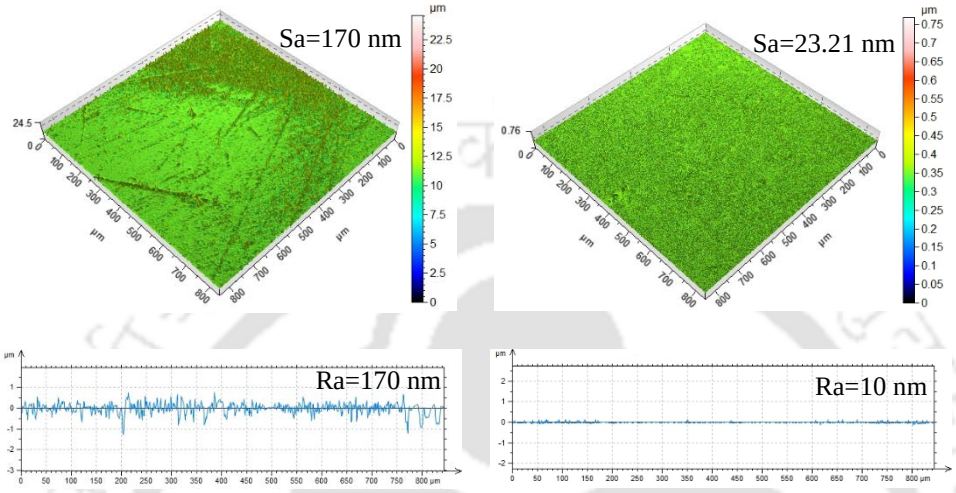

(a) (b)

Fig. 6.10 3D surface topographies and surface roughness profiles of femoral knee joint implant at optimum experimental condition (a) before and (b) after MFAF process

Table 6.8 Advanced field parameters i.e. 3D surface parameters of finished femoral knee component at optimum experimental condition

3D surface parameter	Initial values	Final values
Root mean square height (*Sq*)	210 nm	42.21 nm
Skewness (*Ssk*)	0.04	0.7
Kurtosis (*Sku*)	8.73	7.14
Maximum peak height (*Sp*)	2010 nm	419.23 nm
Maximum pit height (*Sv*)	2290 nm	349.81nm
Maximum height (*Sz*)	4300 nm	769.04 nm
Arithmetical mean height (*Sa*)	170 nm	23.21 nm
Reduced peak height (*Spk*)	300 nm	95.24 nm
Core roughness depth (*Sk*)	360 nm	24.25 nm
Reduced valley depth (*Svk*)	330 nm	63.47 nm

Figure 6.11 shows mirror finished femoral knee implant after complete finishing with MFAF tool. Therefore, MFAF process can provide uniform surface finish over entire surface at the nanometer level and can also generate mirror-finished surface on femoral knee implant.

(a) (b)

Fig. 6.11 (a) Finished titanium femoral knee implant using MFAF tool and (b) mirror finished surface with the reflection

6.3.3 Effect of Process Parameters

In this section, the effect of individual process parameters on final area surface roughness (*Sa*) is discussed in details.

6.3.3.1 Influence of Tool rpm

MFAF tool rpm is a key process parameter in the MFAF process. The final surface roughness and surface topography of femoral knee implant depend on MFAF tool rotational speed. With the rise in tool rpm, final *Sa* decreases and after 1150 tool rpm final *Sa* increases again as shown in Fig. 6.12(a). With the increase of tool rotational speed from 800 rpm to 1000 rpm the final *Sa* gradually decreases with improvement in 3D surface topographies as shown in Figs. 6.13(a) and (b), respectively. The surface topography obtained at 1000 tool rpm becomes more uniform with reduced final *Sa* (Fig. 6.13(b)) than the surface topography obtained at 800 rpm (Fig. 6.13(a)). The surface topography obtained at 1200 tool rpm is given in Fig. 6.13(c). The final surface roughness (40 nm) at 1200 tool rpm is lesser than at 800 rpm (60 nm), although the quality of surface topography is deteriorated in 1200 tool rpm with increased scratch marks due to higher finishing force at 1200 rpm. With the rise in tool rpm, tangential force applied on abrasive particles surges as shown in Table 6.9. The tangential forces are measured using 3-axis dynamometer during finishing. Final *Sa* reduces due to a rise in material removal which happens because of higher finishing force. CIPs form a columnar structure following magnetic field lines [121] embedding abrasive particles at the end of columnar structure as represented in Fig. 6.12(b). MR fluid columnar structures started moving outward due to the increased centrifugal force at higher tool rpm as shown in Fig. 6.12(b). Further increase in tool rpm at 1200 rpm, the columnar structures in

MR fluid starts to break due to a continuous increase in centrifugal force as given in Fig. 6.12(c). Due to uncontrolled random motion of the abrasive particles because of breaking of CIPs chain structure in the finishing zone leads to a rise in surface roughness. In Fig. 6.13(c), the random scratch marks by the abrasive particles are visible which leads to higher deterioration of the finished surface.

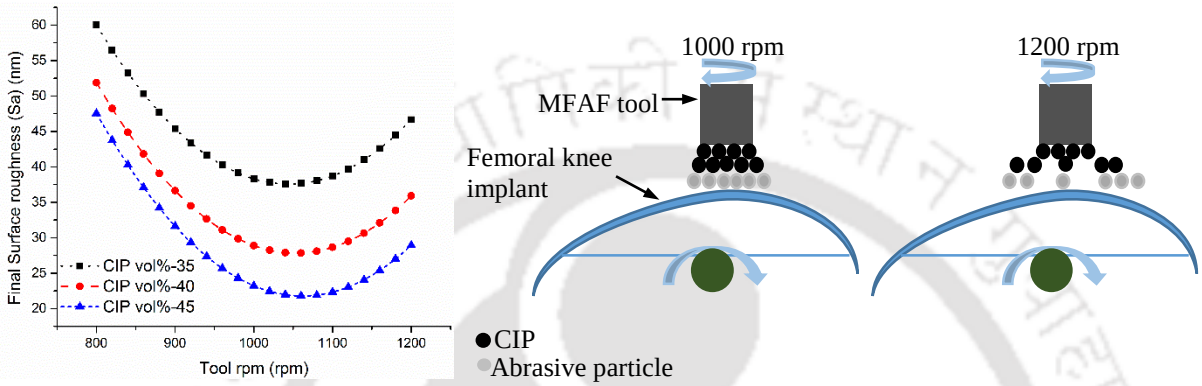

Fig. 6.12 (a) Influence of tool rpm on final *Sa* at different CIP concentration; MR fluid behavior at (b) 1000 and (c) 1200 tool rpm

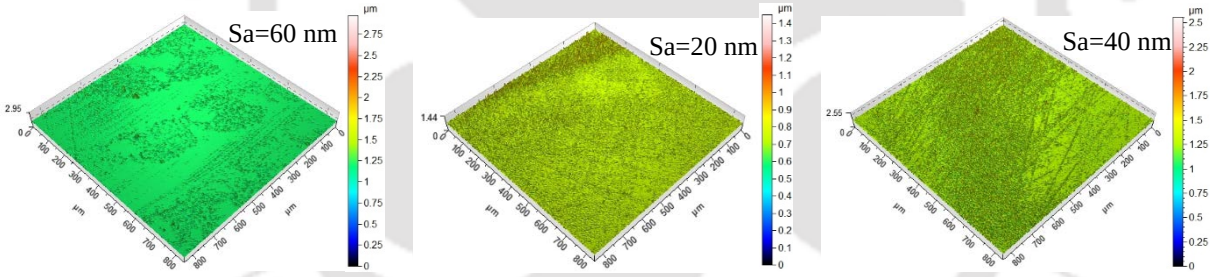

Fig. 6.13 Surface topography at (a) 800, (b)1000 and (c) 1200 tool rpm with 40% CIP concentration and 15 mm/min feed rate

Table 6.9 Tangential forces measured on workpiece surface at different tool rpm

Tool rpm	Tangential force (N)
800	2.24
1000	2.67
1200	3.37

6.3.3.2 Influence of CIP Concentration

Influence of CIP concentration on final *Sa* is shown in Fig. 6.14(a). Rise in CIP concentration improves surface finish of the component. Increase in CIP concentration implies more CIPs in MR fluid as represented in Figs. 6.14(b) and (c). Increase in CIPs results in increased normal force applied on abrasive particles during finishing as given in Table 6.10. The increased

normal force helps in deeper penetration of abrasive particles on workpiece surface which results in lower final *Sa* value. A continuous decrease in final *Sa* is observed with increasing CIP concentration up to 45 Vol. %. However, the rate of decrease in *Sa* reduces at higher CIP concentration. Beyond, 45 Vol. % of CIP concentration, the amount of available abrasive particles to conduct finishing is not sufficient. Also, higher normal force starts to make dents on the already finished surface. Hence, for achieving better polishing, the upper limit of CIP concentration needs to be fixed at 45 Vol. %.

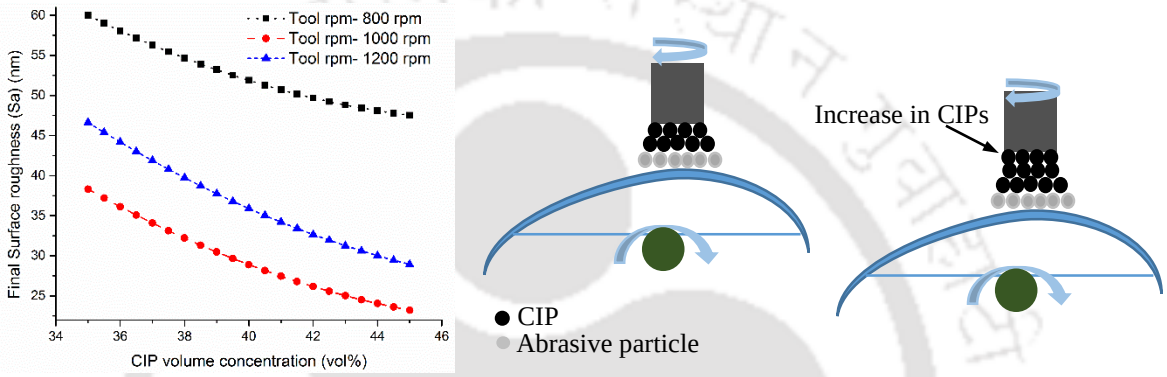

Fig. 6.14 (a) Influence of CIP concentration on final *Sa* at different tool rpm; MR fluid structure at (b) low and (c) high CIP concentration

Table 6.10 Normal forces measured on workpiece surface at different CIP concentration

CIP concentration (Vol. %)	Normal force (N)
35	6.69
40	8.55
45	14.40

6.3.3.3 Influence of Feed Rate

The effect of feed rate on final *Sa* at different tool rpm is shown in Fig. 6.15. Initially, final *Sa* begins to decrease with rise in feed rate and reaches to an optimum value at 15 mm/min. However, final *Sa* starts to increase beyond optimum feed rate as shown in Fig. 6.15. The contact time between MFAF tool and femoral knee implant surface is defined by feed rate as it defines the relative motion between the tool and workpiece. Also, shearing of MR fluid in the finishing zone depends on the feed rate. The contact time between tool and workpiece decreases and the shearing rate of MR fluid increases with the rise in feed rate. Initially, with the rise in feed rate abrasive particles in the finishing zone gets less time to indent the workpiece, although the shearing of the indented material is faster. This combination of indentation and shearing leads to a reduction in

surface roughness of the workpiece. Beyond optimum feed rate of 15 mm/min, the contact time between the tool and workpiece reduces continuously resulting in lower indentation by abrasive particles on the workpiece surface which leads to a very low material removal. Although the shearing force increases further beyond 15 mm/min feed rate, the material removal reduces considerably resulting in lesser improvement in surface finish as seen in Fig. 6.15.

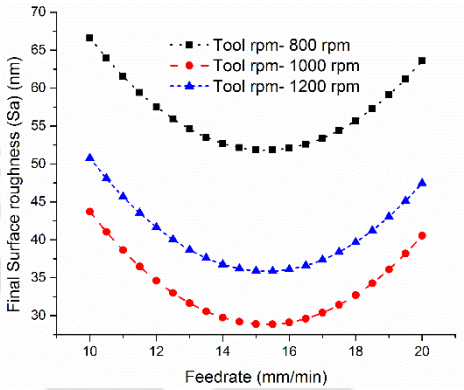

Fig. 6.15 Effect of feed rate on final *Sa* at different tool rpm

6.4 Summary

Nanofinishing of femoral knee implant made of Ti alloy of grade 5 is carried out using MFAF tool. Surface roughness and surface topography obtained at each position of femoral knee implant are analyzed and discussed to explore MFAF tool capability to finish freeform surface at nanometer level. Surface roughness obtained at each position of freeform workpiece after finishing is almost same with standard deviation of 19.23. Also, the final surface topography at different positions show a similar type of surface. The minimum surface roughness (*Ra*) obtained after finishing is 20 nm which satisfies the surface roughness criteria of femoral knee implant according to ISO 7207-2:2011 [102]. From experimental study, it can be concluded that MFAF tool is highly capable to finish freeform surface of femoral knee implant effectively with necessary requirement of surface properties. A statistical design of experiments is used to optimize the key process parameters to obtain minimum surface roughness (*Sa*). The optimum process parameter values to achieve minimum final *Sa* of 21.71 nm are 1062 tool rpm, 15.37 mm/min feed rate and 45% CIP concentration in MR fluid. Further, experiments are conducted at optimum process parameter condition to validate the results obtained from the optimization study. The results obtained from the validation experiments are in close agreement with the optimization study results with acceptable % error of 6.93. The regression equations obtained from the statistical analysis are used

to plot and evaluate the influence of process parameters on final *Sa*. After analyzing present study, to achieve a surface finish below 50 nm on Ti alloy femoral knee implant, the range of tool rpm, CIP concentration and feed rate should be within 900–1100 rpm, 40–45 Vol.% and 12–18 mm/min, respectively.

Chapter 7 Performance analysis of finished Ti alloy for femoral knee implant application

7.1 Introduction

Total Knee Arthroplasty (TKA) or total knee replacement (TKR) surgery is employed to counter knee joint debilitating diseases such as arthritis. The TKR is composed of a femoral component, plastic spacer or bearing and tibial component as shown in Fig. 7.1. Presently, most of the femoral component is made up of a metallic alloy like titanium alloy, cobalt–chrome–molybdenum (CoCrMo) etc. Generally, ultra-high molecular weight polyethylene (UHMWPE) of standard ASTMF648 [122] material is used to make the plastic spacer or bearing. UHMWPE has necessary material properties and biological inertness required for a bearing material in TKR [123]. The failure of TKR is a very serious problem faced by thousands of patient around the globe. The main reason of TKR deterioration is complications related to UHMWPE tibial bearing wear and generated debris due to wear. These type of tribological failures of tibial bearings lead to expensive and risky revision surgery.

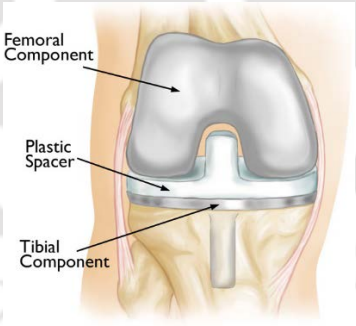

Fig. 7.1 A total knee replacement implant [124]

Implant wear related problems and its effect on the patient is severe [125]. In vivo, the femoral component and the UHMWPE bearing surface experience relative sliding motion. The implant wear occurs in between articulating femoral component and bearing surfaces due to two-body and three-body abrasion. Rough metal surface of femoral component induces abrasion on the UHMWPE bearing surface. The wear of the articulating surfaces further increases due to the trapped wear particles between them. The increase in wear debris leads to periprosthetic bone

resorption [126]. The excessive amount of wear debris causes synovitis and osteolysis. Osteolysis is one of the main reasons for implant failure in most of the patients [127]. Aseptic loosening occurs due to the osteolysis of surrounding bones. Failure of TKR is largely happened due to aseptic loosening or loosening of implants [128,129].

The amount of wear debris generated during in vivo performance of TKR partially depends on the femoral component surface roughness. Friction between the contacting articulating surfaces can be reduced by minimizing adhesion and also by minimizing normal and shear stresses which can be achieved through ultra-high polishing [115]. According to fundamental tribological investigation, wear of UHMWPE increases with an increase in counterface or femoral component surface roughness [130,131]. Also in the laboratory tests, UHMWPE wear escalates with the rise in femoral component surface roughness [132]. A 10-fold rise in the wear rate of UHMWPE is reported with the threefold increase in the roughness of femoral countersurface [133]. In the laboratory tests, with a three-fold surge in counterface roughness, a twenty-fold rise in wear rate of UHMWPE is observed [134]. Also, the wear volume and number of generated wear particles depend on the surface roughness of the counterface [135,136]. Researchers established an exponential relationship between surface roughness (Ra) of counterface i.e. femoral component made of cobalt–chromium alloy and wear of UHMWPE for an extensive range of femoral component surface roughness (*Ra*) of 0.005–0.10 μm based on experimental investigation. The regression equation of wear factor (*K*) [137] is given as

$$K = 6.29\times10^{-9}\exp(24.14Ra) \tag{7.1}$$

According to an experimental study conducted by the authors, a significant advantage is achieved by decreasing surface roughness from 0.05 to below 0.01 μm [137]. Hence, UHMWPE wear and wear debris related problems can be reduced by controlling femoral component surface roughness which results in longer implant life. Surface finish at the nanometer level on hard metals like titanium alloy is achievable using magnetic field assisted finishing (MFAF) process [111]. Hence, freeform surface of a femoral component made of Ti alloy can be nano-finished using MFAF process. Traditionally, tribological investigation to evaluate UHMWPE wear is conducted using a pin-on-disk tribometer or analogous test device [138]. Hence, a preliminary evaluation of UHMWPE (ASTMF648 standard, [122]) disc wear can be conducted using a pin-on-disc tribometer. In the present study, a pin-on-disc tribometer is used to evaluate disc wear relative to

Ti alloy grade 5 pin which is finished by MFAF process. The experimental study is conducted to analyze the performance of the pin polished by MFAF. The performance of MFAF and manually polished pins are compared to find out the ability of MFAF process to produce implant worthy surface. Weight of the sample is measured before and after, and the weight loss represents the level of debris produced after in-vivo performance of TKR [125]. This tribological study will help to understand how the articulating surface of femoral knee implant finished using MFAF process will act during it's in vivo performance.

7.2 Experimental Investigation

Tribology study is carried out to determine the performance of MFAF polished pin on UHMWPE (ASTMF648 standard, [122]) disc. Pin-on-Disc tribometer is used for the tribology investigation following ASTM G99 standard [139] of tribological characterization. Initially, a cylindrical pin made of Ti alloy of grade 5 is fabricated according to the dimension mentioned in Table 7.2 using wire electrical discharge machining (EDM). The UHMWPE discs of dimension 165 mm X 8 mm are prepared using a vertical saw and lathe machine. After fabricating the pins, flat surfaces of 3 pins are finished using MFAF process. The experimental conditions during MFAF process are given in Table 7.1. During finishing, pins are held using a precision vice. A four-axis vertical CNC milling machine is used to hold the MFAF tool during finishing process. A schematic description of MFAF process for polishing Ti alloy pin is presented in Fig. 7.2(a). During finishing of Ti alloy pins, only rotational motion is provided to the MFAF tool without pin movement due to less surface area of the pin as the polishing tool covers entire pin surface. The MR fluid of Type I (Chapter 3, Section 3.2) is used for finishing. Another 3 pins are manually hand polished using 2000 grit size emery paper. Hence, a total of 6 pins are prepared for the tribology study. In the present study, the pins prepared using MFAF process and manual hand polishing are referred as MFAF pin and HP pin, respectively.

Table 7.1 Experimental conditions during MFAF process

Process parameters	**Value**
Tool rpm	900 rpm
Working gap	0.6 mm
Finishing time	4 hrs.30 min
CIP concentration	45 Vol. %
Diamond abrasive concentration	7.1 Vol. %
Base medium concentration	48 Vol. %

After finishing, the specimens are cleaned with deionized water and acetone before tribology study [140]. All the pins and discs are initially weighed before tribology test using a digital balance having an accuracy of ± 0.0001 mg. Also, optical profilometer is used to evaluate surface roughness and surface topography of each pin. After that, the pin is mounted on the pin holder and UHMWPE disc is attached to the disc holder of the tribometer for wear test. Figure 7.2(b) represents a schematic view of pin-on-disc experimental setup for tribology study. A normal load is applied on Ti alloy pin and rotating UHWMPE disc throughout wear test as represented in Fig. 7.2 (b). The process parameter conditions during wear test are given in Table 7.2.

Table 7.2 Process parameter conditions during wear test

Process parameters	**Value**
Normal force	100 N
Disk rpm	100 rpm
Wear track diameter	120 mm
Disk diameter	165 mm
Disk thickness	8 mm
Pin diameter	6 mm
Pin height	25 mm

Ti alloy pin and UHMWPE disc attached with the tribometer during wear tests are given in Fig. 7.3(a). The wear track formed on UHMWPE disc after wear test is presented in Fig. 7.3(b). Weight of each sample (both pin and disk) is measured after wear test. Also, surface roughness and surface topography of each pin and wear track are analyzed.

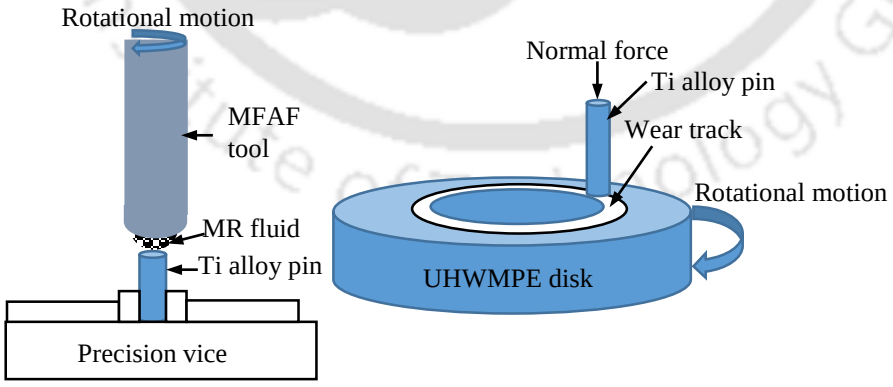

(a) (b)

Fig. 7.2 Schematic description of (a) polishing of Ti alloy pin using MFAF process and (b) pin-on-disc tribometer experimental set-up

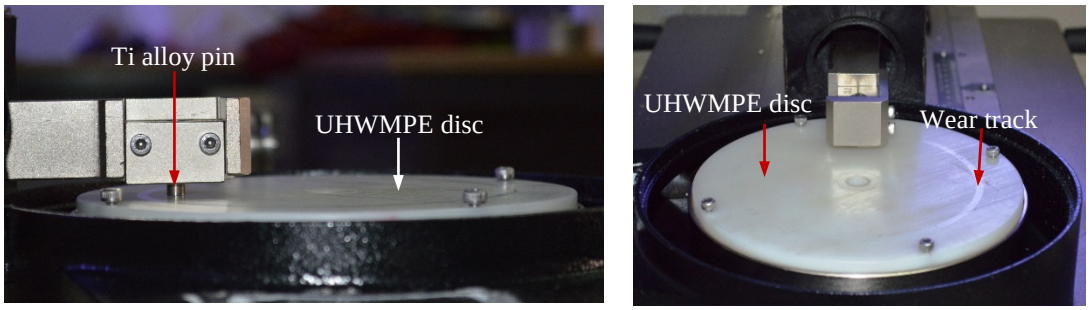

(a) (b)

Fig. 7.3 Experimental set-up of pin-on-disc tribometer showing (a) Ti alloy pin, UHMWPE disc and (b) wear track on UHMWPE disc

7.3 Results and Discussion

Wear test between the Ti alloy pins and UHMWPE disc is carried out to analyze the performance of the finished surface. The Ti alloy pins are polished using two different methods i.e. hand or manual polishing (HP) and MFAF process The obtained results will help to analyze the in vivo performance of the femoral knee implant finished using MFAF process. The following analysis such as volume loss, wear rate, surface roughness and surface topography are carried out after wear test and are discussed below.

7.3.1 Volume Loss Analysis

Volume loss analysis is carried out only for UHMWPE disc due to negligible weight loss of Ti alloy pins after wear test. The volume loss data is required for further calculation of wear rate. The weight and volume loss of UHMWPE disc after wear test for both MFAF and HP pins are given in Table 7.3. The volume loss calculated from respective weight loss data of UHMWPE disc after wear test is given as.

$$\text{Volume loss of UHMWPE disc } (\text{mm}^3) = \frac{\text{Weight loss of UHMWPE disc}}{\text{density}} \tag{7.2}$$

The density of UHMWPE for surgical implants (ASTM F648–10) [122] is 0.927 g/cm^3. From Table 7.3, it is observed that the average volume loss of disc in case of MFAF pin (11.7995 mm^3) is far lesser than HP pins (27.9726 mm^3). The lower volume loss of UHMWPE disc in case of MFAF pins proves that pins polished using MFAF process shows better performance than HP pins. Hence, femoral knee implant polished using MFAF process will provide better performance

due to the formation of lesser debris during knee movement. It will also reduce the problems due to the mixing of debris in the bloodstream.

Table 7.3 Volume loss analysis of UHMWPE disc

MFAF pins	UHMWPE disc		HP pins	UHMWPE disc	
	Weight loss (mg)	Volume loss (mm^3)		Weight loss (mg)	Volume loss (mm^3)
pin 1	9.9241	10.7056	pin 4	25.7258	27.7517
pin 2	12.8750	13.8889	pin 5	23.1389	24.9611
pin 3	10.0152	10.8039	pin 6	28.9272	31.2052
Avg.	10.9381	11.7995	Avg.	25.9306	27.9726

7.3.2 Wear Rate Analysis

Wear rate of articulate surface of knee implant has significant influence on its performance. Wear rate due to the relative motion between the UHMWPE disc and Ti alloy pin gives better understanding of their performance during in vivo performance of knee implant. Wear rate analysis of UHMWPE disc after wear test calculated from volume loss of UHMWPE disc and sliding distance of the pin during experiment is given as

$$\text{Wear rate } (mm^3/m) = \text{Volume loss } (mm^3)/\text{sliding distance (m)} \tag{7.3}$$

where, sliding distance depends upon wear track diameter (D in mm), UHMWPE disc speed (N_d in rpm), wear test duration (T_w in sec) given as

$$\text{Sliding distance (m)} = \frac{\pi D N_d T_w}{60,000} \tag{7.4}$$

The sliding distance during wear test calculated from Eq. (7.4) is 4524 m for 60 mins wear test. The wear rate for each UHMWPE disc is provided in Table 7.4. From Table 7.4, it is found that the average wear rate of UHMWPE disc in case of MFAF pins (0.002608 mm^3/m) is lower than HP pins (0.006359 mm^3/m) which demonstrates better performance by MFAF pins than HP pins.

Table 7.4 Wear rate analysis of UHMWPE disc

MFAF pins	UHMWPE disc Wear rate (mm^3/m)	HP pins	UHMWPE disc Wear rate (mm^3/m)
pin 1	0.002366	pin 3	0.006134
pin 2	0.003070	pin 4	0.005517
pin 3	0.002388	pin 5	0.006897
Avg.	0.002608	Avg.	0.006359

7.3.3 Surface Analysis

Initial and final surfaces of both MFAF and HP pins before and after wear tests are analyzed with the help of surface roughness and surface topography. Surface analysis of the pins shows the changes in surface characteristics after wear test. Also, the wear track generated on the UHMWPE disc after wear test is analyzed using optical surface profilometer. It will help to understand how the articulating surface of femoral knee implant will act during it's in vivo performance.

7.3.3.1 MFAF Pins Surface Analysis

The surface roughness and surface topography of all MFAF pins before and after wear tests are given in Figs. 7.4(i) and (ii), respectively. Surface topography after the wear test shows scratch marks which are not visible in the surface topography before the wear test. The relative motion between Ti alloy pin and UHMWPE disc during wear test results in increased surface roughness on the pin surface. However, the change in surface roughness after wear test is very small for all the pins.

MFAF pin 1

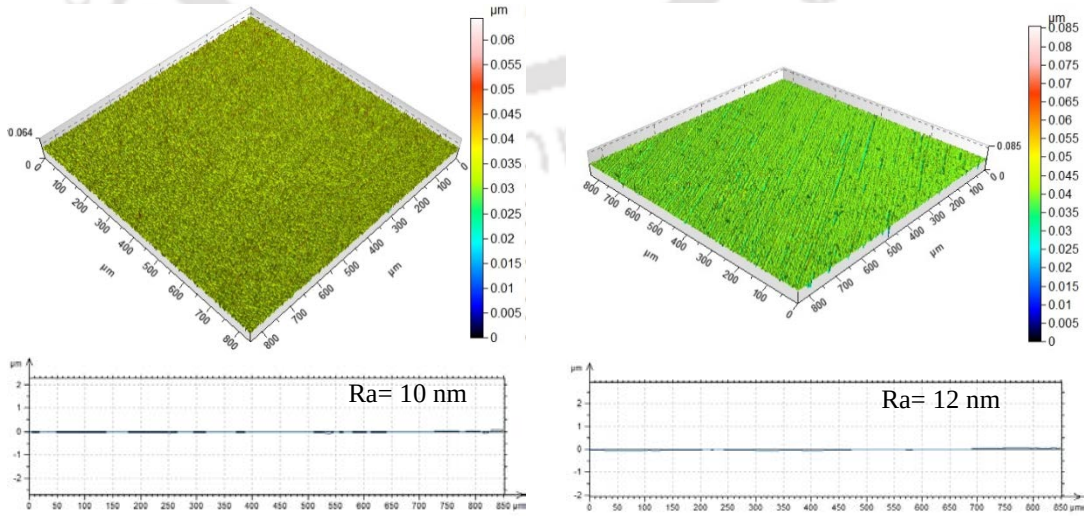

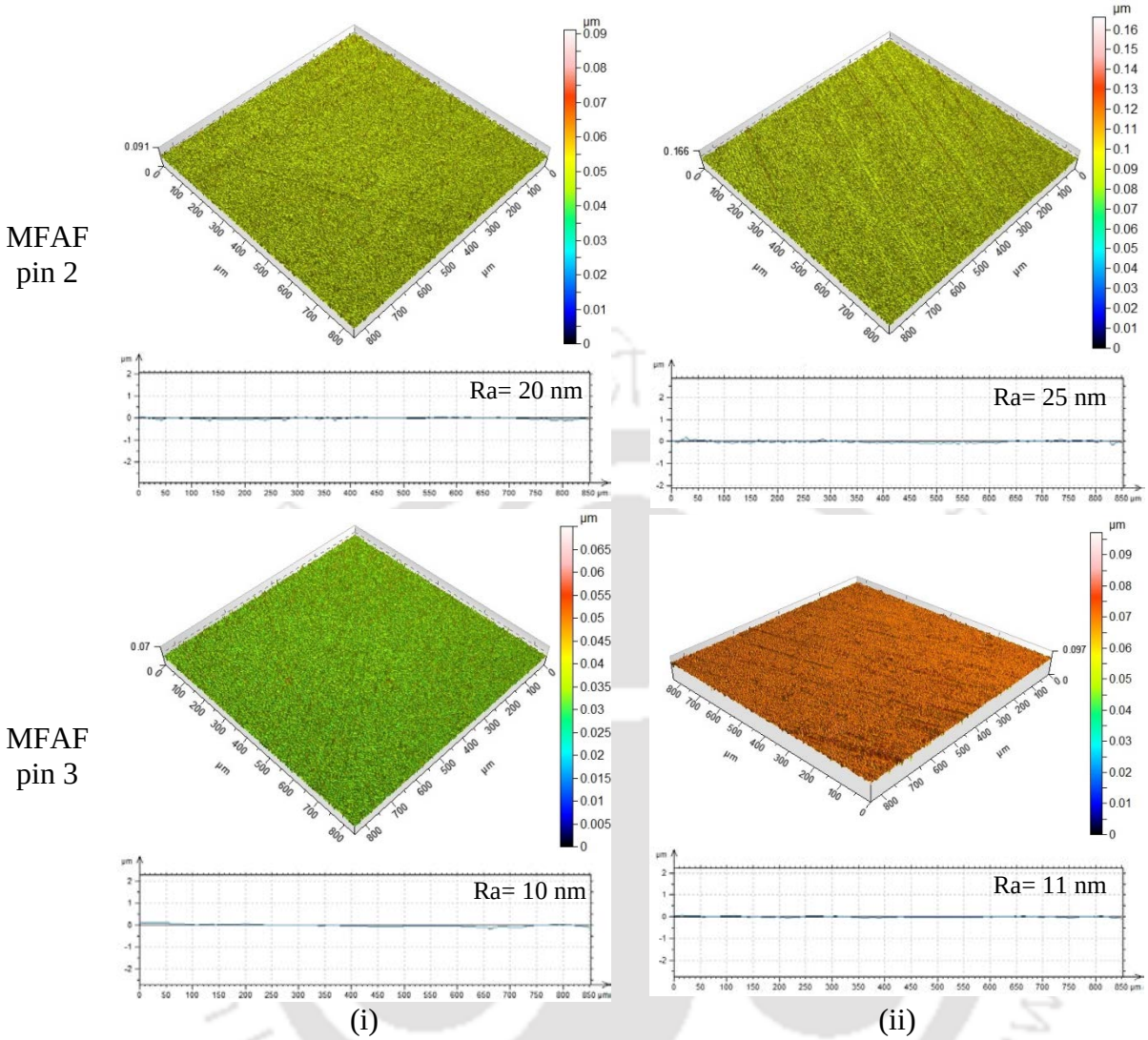

Fig. 7.4 Surface topography and surface profile of MFAF pins (i) before and (ii) after wear test

7.3.3.2 HP Pins Surface Analysis

Similarly, the surface roughness and surface topography of HP pins before and after wear tests are presented in Figs. 7.5(i) and (ii), respectively. Surface roughness of the HP pins (Fig. 7.5(i)) and also the change in surface roughness after wear test (Fig. 7.5(ii)) are higher than MFAF polished pins. Deep scratch marks (Fig. 7.5(ii)) are observed in all HP pins after wear test due to higher initial surface roughness of HP pins. The combined surface roughness of the pin and disc is higher in case of HP pins than MFAF pins. Therefore, the friction between the femoral component polished by MFAF process and the plastic bearing of knee implant (i.e. UHMWPE material) will be less during their relative motion [115]. Hence, better performance is expected in case of MFAF pins than HP pins.

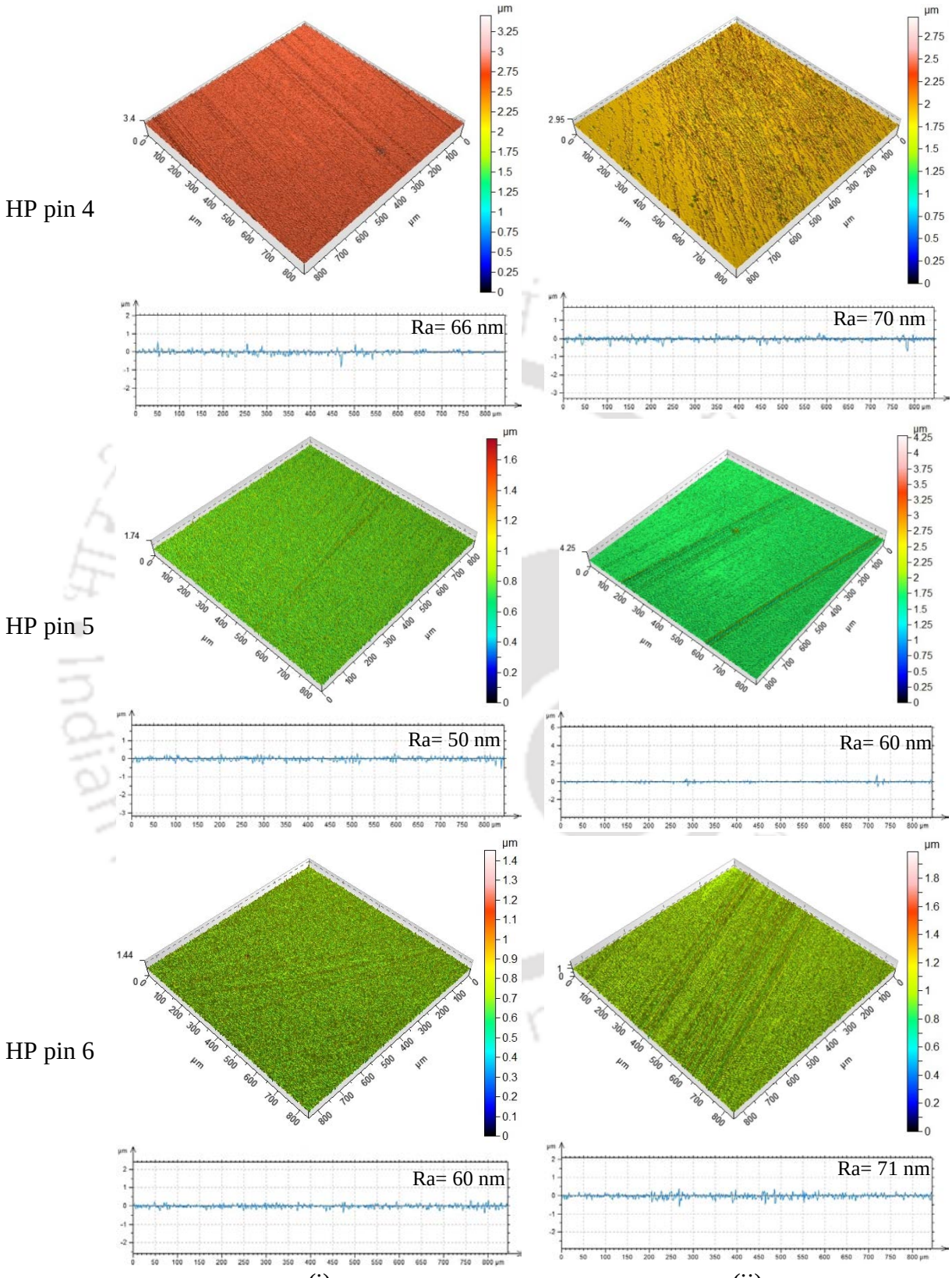

Fig. 7.5 Surface topography and surface profile of the HP pins (i) before and (ii) after wear test

7.3.3.3 Wear Track Surface Analysis

The wear track diameter is kept fixed to 120 mm during wear test. The surface topography of UHMWPE disc before wear test is given in Fig. 7.6(a). The trace of the wear track on UHMWPE disc after wear test is given in Fig. 7.6(b). The surface topography of the wear track on UHMWPE disc generated by MFAF and HP pins is analyzed using optical surface profilometer and are shown in Figs. 7.7(a) and (b), respectively. The surface topographies generated by this two pins are different as observed from Fig. 7.7. The wear track of MFAF pin (Fig. 7.7(a)) shows lesser deep valleys than HP pin (Fig. 7.7(b)). Deep scratch marks are generated by HP pin as compared to MFAF pins due to higher surface roughness of HP pins.

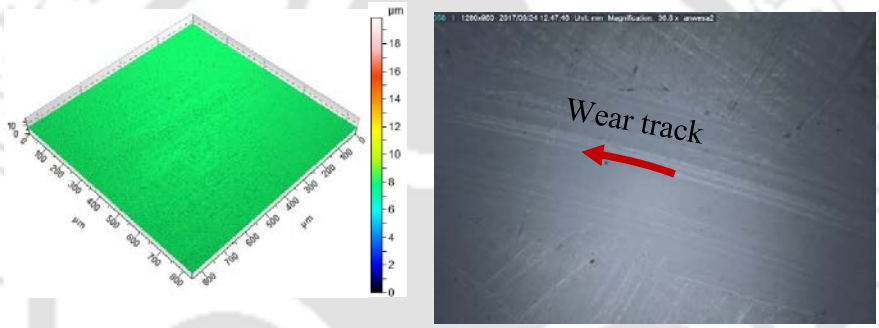

(a) (b)

Fig. 7.6 (a) Surface topography of UHMWPE disc before wear test and (b) wear track on UHMWPE disc after wear test

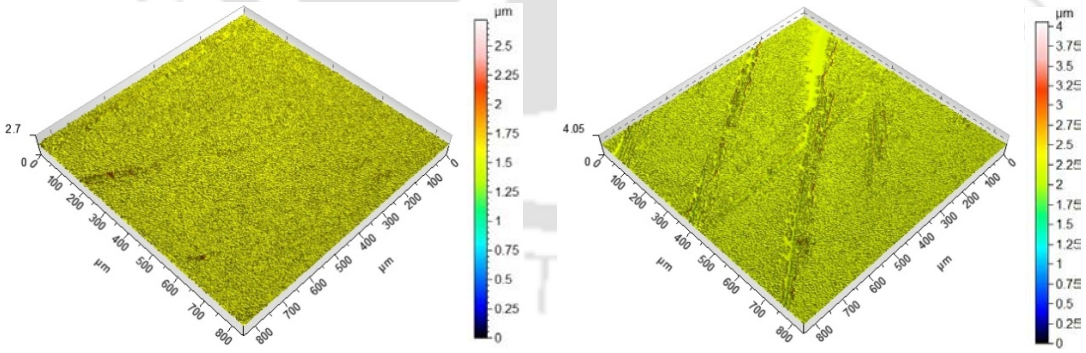

(a) (b)

Fig. 7.7 Surface topographies of wear track generated by (a) MFAF pin and (b) HP pin

Hence, the surface analysis shows that surface quality of the pin and corresponding wear track are better in case of MFAF pins than HP pins. The surface roughness of HP pins deteriorates at a higher rate than MFAF pins for same duration of wear test. Also, the wear track by HP pin has more deep scratch marks and deeper valleys as compared to MFAF pin. Hence, MFAF polished

femoral implant surface will provide higher performance for a longer duration of time than hand or manually polished surface.

7.4 Summary

In this chapter, tribological studies are carried out to analyze the performance of MFAF polished surface with respect to manually polished surface on UHMWPE disc used in prosthetic implants. This analysis will help to better understand in vivo performance of a femoral component of knee joint finished at nanometric level by MFAF process. After wear test, different analysis like volume loss, wear rate, surface roughness, surface topography and wear track analysis are carried out to explore the wear characteristics properly. From volume loss analysis, it is observed that the volume loss of UHMWPE disc in case of MFAF pin (11.7995 mm^3) is lower than HP pins (27.9726 mm^3). The lower volume loss of UHMWPE disc in case of MFAF pins leads to lesser wear debris generation resulting in lsser problems related to wear debris. Hence, femoral knee implant polished using MFAF process will have fewer problems related to wear debris. The wear rate analysis reveals that the wear rate of UHMWPE disc in case of MFAF pin (0.002608 mm^3/m) is lower than HP pin (0.006359 mm^3/m). It can be speculated from the wear analysis that the wear of UHMWPE bearing surface will be less with MFAF polished femoral component. From surface roughness analysis it is found that the change in surface roughness for MFAF pins is lower than HP pins after wear test. From surface roughness investigation it can be predicted that during in vivo performance of total knee replacement the change in surface roughness for MFAF polished femoral component will be less according to wear test results. The wear track analysis shows that more deep scratch marks are generated in the wear track for HP pins than MFAF pins for same wear test duration. Hence, wear test analysis proves that MFAF polished femoral surface will provide higher in vivo performance for longer time duration than manually polished surface.

Chapter 8 Conclusions and scope for future work

8.1 Conclusions

In the present work, a polishing tool is designed and developed to finish freeform surface of femoral part of knee joint made of Ti alloy. Preliminary experimental investigations are carried out to explore the capability of the developed tool, to find out appropriate MR fluid composition for different implants and to generate optimum toolpath. Afterward, flat Ti alloy workpiece and femoral component of knee joint are finished with developed tool and necessary experimental investigations are carried out to understand the process. Also, simulation and experimental study of the finishing forces involved in MFAF process are carried out. Later, wear analysis of finished surfaces is carried out to understand in vivo performance of the component. Following conclusions are drawn from the work reported in the thesis.

8.1.1 Preliminary Investigation

8.1.1.1 MFAF Tool Development

A polishing tool is designed and developed to finish freeform surfaces. FEA based software is used for the simulation study to find out the optimum design configuration and dimension of the developed tool for achieving better finishing characteristics. The conclusions drawn from this study are as follows:

- The optimum dimension of magnet is found to be 70 mm in height, 10 and 15 mm in diameter. The spherical shape of magnet fixture at the tool end is found to be the best configuration. Mu-metal is used as the material for magnet fixture due to its magnetic field shielding property.
- The maximum achieved magnetic flux density on the workpiece surface using novel developed tool is 0.4 Tesla which is sufficient enough to carry out finishing operation.

8.1.1.2 Synthesis of Optimum MR Fluid

Two types of MR fluids are synthesized to generate different type of surfaces. The generated surface morphologies are studied and analyzed in relation to the implant surfaces. The conclusions drawn from the study reported in the thesis are as follows:

- Both MR fluid consists of carbonyl iron particles (CIPs) and diamond abrasive powder in acidic base medium. Base medium constituents of MR fluid of Type – I is hydrofluoric acid (HF), nitric acid (HNO_3) and deionized water. In case of MR fluid of Type – II the base medium consists of hydrogen peroxide (H_2O_2) and deionized water
- The obtained surface after finishing with MR fluid of Type – I is smoother (having surface roughness of 10 nm) with less number of pits and valleys than with MR fluid of Type – II.
- From wettability study of finished surface using goniometer, it is found that the surface finished with MR fluid of Type – I is hydrophilic in nature while with MR fluid of Type – II is hydrophobic.
- In both cases, the formation of oxide layer on the finished Ti alloy surface is observed which enhances the bio-compatibility of the implant.
- MR fluid of Type – I is better suited for semi-permanent type of implants or implants which partake in relative motion like femoral part of knee joint and hip joint due to highly polished (*Ra*–10 nm) hydrophilic surface.
- MR fluid of Type – II is better suited for permanent implants like dental implants as it provides better chance of osseointegration due to the obtained surface characteristics of relatively higher surface roughness (*Ra*–70 nm) with hydrophobic nature.

8.1.1.3 Optimum Toolpath Generation

Both spiral and parallel toolpaths are generated to find out the appropriate toolpath to finish Ti alloy workpiece. The observations made during the study are as follows:

- The surface topography and surface texture show reduced surface roughness and scratch marks when the surface is finished with parallel toolpath having surface roughness of 10 nm than spiral toolpath (*Ra*–40 nm).

8.1.2 Experimental Investigation

8.1.2.1 Finishing of Flat Surface

The capability of the MFAF process to deliver implant worthy surface roughness and texture is analyzed by exploring 3D surface roughness parameters with the help of statistical DOE analysis. An optimization study is carried out to minimize the value of *Sa*, *Spk* & *Sk* and maximize *Svk* for achieving optimum implant surface roughness value which will aid in increased implant life, better implant performance along with better wear properties.

- The optimum values of *Sa* (11.32 nm), *Spk* (15.82 nm), *Sk* (6.51 nm) and *Svk* (41.15 nm) are observed at 901 rpm of the tool, 0.60 mm working gap and 4 hrs. 45 min of finishing time.
- Tool rpm, working gap and finishing time should be in the range of 700–1100 rpm, 0.8–1.2 mm and 4–5 hrs., respectively for better area surface roughness (*Sa*), to reduce debris generation during in vivo implant performance of femoral knee implant and for better wear properties of the implant
- Tool rpm, working gap and finishing time should be in the range of 1100–1200 rpm, 0.6–0.8 mm, and 5 hrs. 30 min–6 hrs., respectively for better fluid retention capability of the implant.
- From experimental study, it is concluded that CIP chains break at a high rpm due to the shear thinning nature of MR fluid. Also, at high working gap the finishing capability of abrasive particles reduces due to the insufficient magnetic field in the finishing zone. Furthermore, after 6 hrs. of finishing time the surface roughness of workpiece increases again due to the plowing of abrasive particles on already finished workpiece surface.

8.1.2.2 Finishing of Freeform Surface

Nano-finishing of femoral knee implant made of Ti alloy of grade 5 is carried out using MFAF tool. Surface roughness and surface topography obtained at each position of femoral knee implant are analyzed and discussed to explore MFAF tool capability to finish freeform surface at nanometer level. Following conclusions are obtained from the experimental study.

- MFAF tool has the ability to finish freeform surface of femoral knee implant almost uniformly along the surface curvature with necessary requirement of surface properties.
- The optimum process parameter values to achieve minimum final *Sa* of 23.21 nm are 1062 tool rpm, 15 mm/min feed rate and 45% CIP volume concentration in MR fluid.
- To achieve a surface finish below 50 nm on Ti alloy femoral knee implant the range of tool rpm, CIP volume concentration and feed rate should be in the range of 900–1100 rpm, 40 –45 Vol.% and 12–18 mm/min, respectively.

8.1.3 Force Analysis

The analysis of finishing forces involved in the present MFAF process is carried out for better understanding and precise control of the process. Simulation study of MFAF process concerning finishing forces is carried out in two FEA based software. Validation experiments are conducted to substantiate the simulation study. A material removal model for a single abrasive particle is also simulated. A statistical DOE analysis is also conducted to evaluate the significance of each process parameter. Following conclusions are drawn from the present study.

- Normal force (F_n) is responsible for the indentation of abrasive particles on workpiece surface. Magnetic force is considered as the main component of normal force.
- Tangential force (F_{tan}) is responsible for shearing of the indented materials from workpiece surface. A combination of centrifugal force and shear force acting on abrasive particle is considered as the tangential force in MFAF process.
- The validation experimental investigation shows minor variation between experimental measured and simulated forces.
- Significant process parameters in case of F_n are abrasive concentration (37.89% contribution), working gap (29.73% contribution) and CIP concentration (24.65% contribution).
- The significant factors in case of F_{tan} are tool rpm (51.29% contribution), square of tool rpm (11.57% contribution), working gap (10.24% contribution), square of CIP concentration (6.47% contribution) and square of working gap (6.45% contribution).
- F_n acting on the abrasive particles increases with increase in CIP concentration and decrease in abrasive particle concentration, working gap & tool rpm.

- F_{tan} increases continuously with the rise in the tool rpm, CIP concentration and decrease in working gap. Initially, an increase in abrasive concentration increases F_{tan} little bit however it decreases with additional abrasive concentration.

8.1.4 Tribological Study

Tribological studies are carried out to analyze the performance of MFAF polished surface with respect to manually polished surface on UHMWPE disc used in prosthetic implants. Conclusions drawn from the present study are as follows:

- From volume loss analysis, it is concluded that the femoral knee implant polished using MFAF process will have fewer problems related to wear debris
- It can be speculated from the wear analysis that the wear of UHMWPE bearing surface will be less with MFAF polished femoral component.
- From surface roughness analysis, it can be presumed that the wear of UHMWPE bearing surface will be less with MFAF polished femoral component.
- The wear track analysis shows that more deep scratch marks are generated in the wear track while using hand/manually polished pins than MFAF pins for same wear test duration.

8.2 Scope for Future Work

- It is observed from the preliminary experimental study that the finishing efficiency of the MFAF process can be increased with optimum MR fluid composition for biomedical application. Base medium of MR fluids can be further synthesized and optimized for a broad spectrum of prosthetic implants fabricated with different materials.
- The MFAF tool can be further modified to reduce its width so to increase the reach of MFAF tool over the entire implant.
- The MFAF tool can be attached to the 5-axis or higher order CNC machine to increase the process efficiency. Also, it will increase the uniformity of the achieved surface roughness over the implant surface roughness.
- The MR fluid delivery system can be automated to make the fluid delivery precise and controllable at the finishing zone with in situ MR fluid conditioning system.

- The MR fluid behavior during the finishing under MFAF tool can be further modelled using different simulation techniques to get a better grasp of the process mechanism.
- An in depth tribology study can be conducted to analyze the performance of polished femoral knee implant by MFAF process.

References

[1] Mizugaki Y, Sakamoto M, Kamijo K, Taniguchi N. Development of metal-mold polishing robot system with contact pressure control using CAD/CAM data. CIRP Ann - Manuf Technol 1990;39:523–6.

[2] Weule H, Timmermann S. Automation of the surface finishing in the manufacturing of dies and molds. CIRP Ann Technol 1990;39:299–303.

[3] Huang H, Gong Z., Chen X., Zhou L. Robotic grinding and polishing for turbine-vane overhaul. J Mater Process Technol 2002;127:140–5.

[4] Shiou F-J, Chen C-CA, Li W-T. Automated surface finishing of plastic injection mold steel with spherical grinding and ball burnishing processes. Int J Adv Manuf Technol 2006;28:61–6.

[5] Wu X, Kita Y, Ikoku K. New polishing technology of free form surface by GC. J Mater Process Technol 2007;187–188:81–4.

[6] Beaucamp AT, Namba Y, Charlton P, Jain S, Graziano AA. Finishing of additively manufactured titanium alloy by shape adaptive grinding (SAG). Surf Topogr Metrol Prop 2015;3:24001.

[7] Nowicki B, Szafarczyk M. The new method of free form surface honing. CIRP Ann - Manuf Technol 1993;42:425–8.

[8] Dynarowski R, Nowicki B. Investigation on non-conventional honing of sculptured surfaces for parts made of alloy steel. J Mater Process Technol 2001;109:270–6.

[9] Tam H, Lui OC, Mok ACK. Robotic polishing of free-form surfaces using scanning paths. J Mater Process Technol 1999;95:191–200.

[10] Cho S-S, Ryu Y-K, Lee S-Y. Curved surface finishing with flexible abrasive tool. Int J Mach Tools Manuf 2002;42:229–36.

[11] Walker D, Beaucamp A, Dunn C, Freeman R, Marek A, McCavana G, et al. First results on free-form polishing using the Precessions process. Proc. ASPE Winter Conf. Free. Opt. Des. Fabr. Metrol. Assem., 2004.

[12] Brinksmeier E, Riemer O, Gessenharter A. Finishing of structured surfaces by abrasive polishing. Precis Eng 2006;30:325–36.

[13] Pa PS. Magnetic-assistance finishing processes in freeform surfaces. J Mater Eng Perform 2009;18:399–405.

[14] Pa PS. Design of a magnetic-assistance superfinish module for freeform machining. J Vac Sci Technol B Microelectron Nanom Struct 2009;27:1221.

[15] Shiou F-J, Chen C-H. Freeform surface finish of plastic injection mold by using ball-burnishing process. J Mater Process Technol 2003;140:248–54.

[16] Pa PS. Design of freeform surface finish using burnishing assistance following electrochemical finishing. J Mech Sci Technol 2007;21:1630–6.

[17] Shinmura T, Takazawa K, Hatano E, Matsunaga M, Matsuo T. Study on magnetic abrasive finishing. CIRP Ann Technol 1990;39:325–8.

[18] Kim J-D, Kang Y-H, Bae Y-H, Lee S-W. Development of a magnetic abrasive jet machining system for precision internal polishing of circular tubes. J Mater Process Technol 1997;71:384–93.

[19] Yamaguchi H, Shinmura T. Study of an internal magnetic abrasive finishing using a pole rotation system: Discussion of the characteristic abrasive behavior. Precis Eng 2000;24:237–44.

[20] Jain VK, Kumar P, Behera PK, Jayswal SC. Effect of working gap and circumferential speed on the performance of magnetic abrasive finishing process. Wear 2001;250:384–90.

[21] Chang G-W, Yan B-H, Hsu R-T. Study on cylindrical magnetic abrasive finishing using unbonded magnetic abrasives. Int J Mach Tools Manuf 2002;42:575–83.

[22] Mori T, Hirota K, Kawashima Y. Clarification of magnetic abrasive finishing mechanism. J Mater Process Technol 2003;143:682–6.

[23] Yamaguchi H, Shinmura T. Internal finishing process for alumina ceramic components by a magnetic field assisted finishing process. Precis Eng 2004;28:135–42.

[24] Yin S, Shinmura T. Vertical vibration-assisted magnetic abrasive finishing and deburring for magnesium alloy. Int J Mach Tools Manuf 2004;44:1297–303.

[25] Yamaguchi H, Shinmura T, Sekine M. Uniform internal finishing of SUS304 stainless steel bent tube using a magnetic abrasive finishing process. J Manuf Sci Eng 2005;127:605–11.

[26] Yamaguchi H, Shinmura T, Ikeda R. Study of internal finishing of austenitic stainless steel capillary tubes by magnetic abrasive finishing. J Manuf Sci Eng 2007;129:885–92.

[27] Yamaguchi H, Hanada K. Development of spherical magnetic abrasive made by plasma spray. J Manuf Sci Eng 2008;130:31107.

[28] Kang J, George A, Yamaguchi H. High-speed internal finishing of capillary tubes by magnetic abrasive finishing. Procedia CIRP 2012;1:414–8.

[29] Lee Y-H, Wu K-L, Jhou J-H, Tsai Y-H, Yan B-H. Two-dimensional vibration-assisted magnetic abrasive finishing of stainless steel SUS304. Int J Adv Manuf Technol 2013;69:2723–33.

[30] Golini D, Kordonski WI, Dumas P, Hogan SJ. Magnetorheological finishing (MRF) in commercial precision optics manufacturing. In: Stahl HP, editor. Proc. SPIE 3782, Opt. Manuf. Test. III, 1999, p. 80–91.

[31] Shorey AB, Jacobs SD, Kordonski WI, Gans RF. Experiments and observations regarding the mechanisms of glass removal in magnetorheological finishing. Appl Opt 2001;40:20–33.

[32] Cheng HB, Yam Y, Wang YT. Experimentation on MR fluid using a 2-axis wheel tool. J Mater Process Technol 2009;209:5254–61.

[33] Cheng HB, Feng YP, Ren LQ, To S, Wang YT. Material removal and micro-roughness in

fluid-assisted smoothing of reaction-bonded silicon carbide surfaces. J Mater Process Technol 2009;209:4563–7.

[34] Sidpara A, Jain VK. Nano-level finishing of single crystal silicon blank using magnetorheological finishing process. Tribol Int 2012;47:159–66.

[35] Tricard M, Dumas P, Golini D, Mooney J. SOI wafer polishing with magnetorheological finishing (MRF). Proc. SOI Conf. 2003, IEEE Int., vol. 9, 2003, p. 127–9.

[36] Lee S-N, Park S-J, Lee J-I, Yook J-G, Kim Y-J, Lee S-J. Application of MRF scheme for low-loss transmission lines on CMOS-grade silicon. Electron. Components Technol. Conf. 2005. Proceedings. 55th, IEEE; 2005, p. 1514–8.

[37] Kordonski WI, Shorey AB, Tricard M. Magnetorheological jet (MR Jet^{TM}) finishing technology. J Fluids Eng 2006;128:20–6.

[38] Tricard M, Kordonski WI, Shorey AB, Evans C. Magnetorheological jet finishing of conformal, freeform and steep concave optics. CIRP Ann - Manuf Technol 2006;55:309–12.

[39] Jha S, Jain VK. Design and development of the magnetorheological abrasive flow finishing (MRAFF) process. Int J Mach Tools Manuf 2004;44:1019–29.

[40] Jha S, Jain VK. Nanofinishing of silicon nitride workpieces using magnetorheological abrasive flow finishing. Int J Nanomanuf 2006;1:17–25.

[41] Jha S, Jain VK, Komanduri R. Effect of extrusion pressure and number of finishing cycles on surface roughness in magnetorheological abrasive flow finishing (MRAFF) process. Int J Adv Manuf Technol 2007;33:725–9.

[42] Das M, Jain VK, Ghoshdastidar PS. Nanofinishing of flat workpieces using rotational–magnetorheological abrasive flow finishing (R-MRAFF) process. Int J Adv Manuf Technol 2012;62:405–20.

[43] Das M, Jain VK, Ghoshdastidar PS. Nano-finishing of stainless-steel tubes using rotational magnetorheological abrasive flow finishing process. Mach Sci Technol 2010;14:365–89.

[44] Singh AK, Jha S, Pandey PM. Design and development of nanofinishing process for 3D surfaces using ball end MR finishing tool. Int J Mach Tools Manuf 2011;51:142–51.

[45] Rabinow J. The magnetic fluid clutch. Trans Am Inst Electr Eng 1948;67:1308–15.

[46] Sidpara A, Das M, Jain VK. Rheological characterization of magnetorheological finishing fluid. Mater Manuf Process 2009;24:1467–78.

[47] Bossis G, Volkova O, Lacis S, Meunier A. Magnetorheology: fluids, structures and rheology. Lect notes physics-new york then berlin- 2002:202–32.

[48] De Vicente J, López-López MT, González-Caballero F, Durán JDG. Rheological study of the stabilization of magnetizable colloidal suspensions by addition of silica nanoparticles. J Rheol 2003;47:1093–109.

[49] Phulé PP, Ginder JM. Synthesis and properties of novel magnetorheological fluids having improved stability and redispersibility. Int J Mod Phys B 1999;13:2019–27.

[50] Rankin PJ, Horvath AT, Klingenberg DJ. Magnetorheology in viscoplastic media. Rheol Acta 1999;38:471–7.

[51] Park JH, Chin BD, Park OO. Rheological properties and stabilization of magnetorheological fluids in a water-in-oil emulsion. J Colloid Interface Sci 2001;240:349–54.

[52] Chin BD, Park JH, Kwon MH, Park OO. Rheological properties and dispersion stability of magnetorheological (MR) suspensions. Rheol Acta 2001;40:211–9.

[53] López-López MT, De Vicente J, González-Caballero F, Durán JDG. Stability of magnetizable colloidal suspensions by addition of oleic acid and silica nanoparticles. Colloids Surfaces A Physicochem Eng Asp 2005;264:75–81.

[54] Ginder JM, Davis LC, Elie LD. Rheology of magnetorheological fluids: models and measurements. Int J Mod Phys B 1996;10:3293–303.

[55] Jolly MR, Carlson JD, Munoz BC. A model of the behaviour of magnetorheological materials. Smart Mater Struct 1996;5:607.

[56] Jha S, Jain VK. Rheological characterization of magnetorheological polishing fluid for MRAFF. Int J Adv Manuf Technol 2009;42:656–68.

[57] Hryniewicz T, Rokicki R, Rokosz K. Magnetoelectropolished titanium biomaterial. Biomater Sci Eng 2011:227–47.

[58] Wong JY, Bronzino JD, Peterson DR. Biomaterials: principles and Practices. CRC Press; 2012.

[59] Luckey H. Titanium for Surgical Implants. Metall Soc Titan Energy Ind Appl 1981:293–312.

[60] Long M, Rack HJ. Titanium alloys in total joint replacement—a materials science perspective. Biomaterials 1998;19:1621–39.

[61] Niinomi M. Mechanical properties of biomedical titanium alloys. Mater Sci Eng A 1998;243:231–6.

[62] Basim GB, Ozdemir Z, Mutlu O. Biomaterials applications of chemical mechanical polishing. Planarization/CMP Technol. (ICPT 2012), Int. Conf., VDE; 2012, p. 1–5.

[63] Tamaki Y, Miyazaki T, Suzuki E, Miyaji T. Polishing of titanium prosthetics (Part 6). The chemical polishing baths containing hydrofluoric acid and nitric acid. Shika Zair Kikai 1989;8:103–9.

[64] Hayes JS, Seidenglanz U, Pearce AI, Pearce SG, Archer CW, Richards RG. Surface polishing positively influences ease of plate and screw removal. Eur Cell Mater 2010;19:117–26.

[65] Ban S, Iwaya Y, Kono H, Sato H. Surface modification of titanium by etching in concentrated sulfuric acid. Dent Mater 2006;22:1115–20.

[66] Khanlou HM, Ang BC, Barzani MM, Silakhori M, Talebian S. Prediction and characterization of surface roughness using sandblasting and acid etching process on new non-toxic titanium biomaterial: adaptive-network-based fuzzy inference System. Neural

Comput Appl 2015;26:1751–61.

[67] Finke B, Testrich H, Rebl H, Walschus U, Schlosser M, Zietz C, et al. Plasma-deposited fluorocarbon polymer films on titanium for preventing cell adhesion: a surface finishing for temporarily used orthopaedic implants. J Phys D Appl Phys 2016;49:234002.

[68] Okada A, Uno Y, Yabushita N, Uemura K, Raharjo P. High efficient surface finishing of bio-titanium alloy by large-area electron beam irradiation. J Mater Process Technol 2004;149:506–11.

[69] Okawa S, Watanabe K. Chemical mechanical polishing of titanium with colloidal silica containing hydrogen peroxide--mirror polishing and surface properties. Dent Mater J 2009;28:68–74.

[70] Keller JC, Stanford CM, Wightman JP, Draughn RA, Zaharias R. Characterizations of titanium implant surfaces. III. J Biomed Mater Res Part A 1994;28:939–46.

[71] Bowers KT, Keller JC, Randolph BA, Wick DG, Michaels CM. Optimization of surface micromorphology for enhanced osteoblast responses in vitro. Int J Oral Maxillofac Implants 1992;7.

[72] Buser D, Schenk RK, Steinemann S, Fiorellini JP, Fox CH, Stich H. Influence of surface characteristics on bone integration of titanium implants. A histomorphometric study in miniature pigs. J Biomed Mater Res Part A 1991;25:889–902.

[73] Breen DJ, Stoker DJ. Titanium lines: a manifestation of metallosis and tissue response to titanium alloy megaprostheses at the knee. Clin Radiol 1993;47:274–7.

[74] Wang A, Yue S, Bobyn J., Chan F., Medley J. Surface characterization of metal-on-metal hip implants tested in a hip simulator. Wear 1999;225:708–15.

[75] McGee MA, Howie DW, Costi K, Haynes DR, Wildenauer CI, Pearcy MJ, et al. Implant retrieval studies of the wear and loosening of prosthetic joints: a review. Wear 2000;241:158–65.

[76] Suzuki H, Kodera S, Hara S, Matsunaga H, Kurobe T. Magnetic field-assisted polishing—application to a curved surface. Precis Eng 1989;11:197–202.

[77] Kim J-D, Choi M-S. Study on magnetic polishing of free-form surfaces. Int J Mach Tools Manuf 1997;37:1179–87.

[78] Kim J, Noh I. Magnetic polishing of three dimensional die and mold surfaces. Int J Adv Manuf Technol 2007;33:18–23.

[79] Kim W-B, Lee S-H, Min B-K. Surface finishing and evaluation of three-dimensional silicon microchannel using magnetorheological fluid. J Manuf Sci Eng 2005;126:772–8.

[80] Seok J, Kim Y-J, Jang K-I, Min B-K, Lee SJ. A study on the fabrication of curved surfaces using magnetorheological fluid finishing. Int J Mach Tools Manuf 2007;47:2077–90.

[81] Lin C-T, Yang L-D, Chow H-M. Study of magnetic abrasive finishing in free-form surface operations using the Taguchi method. Int J Adv Manuf Technol 2007;34:122–30.

[82] Singh AK, Jha S, Pandey PM. Nanofinishing of a typical 3D ferromagnetic workpiece using

ball end magnetorheological finishing process. Int J Mach Tools Manuf 2012;63:21–31.

[83] Singh AK, Jha S, Pandey PM. Performance evaluation of improved ball end magnetorheological finishing process. World Acad Sci Technol 2012;6:1193–7.

[84] Sidpara A, Jain V. Nanofinishing of freeform surfaces of prosthetic knee joint implant. Proc Inst Mech Eng Part B J Eng Manuf 2012;226:1833–46.

[85] Yamaguchi H, Graziano AA. Surface finishing of cobalt chromium alloy femoral knee components. CIRP Ann Technol 2014;63:309–12.

[86] Preston FW. The theory and design of plate glass polishing machines Part II. J Soc Glas Technol 1929;13:111–23.

[87] Degroote JE, Marino AE, Wilson JP, Bishop AL, Lambropoulos JC, Jacobs SD. Removal rate model for magnetorheological finishing of glass. Appl Opt 2007;46:7927–41.

[88] Jung B, Jang K-I, Min B-K, Lee SJ, Seok J. Magnetorheological finishing process for hard materials using sintered iron-CNT compound abrasives. Int J Mach Tools Manuf 2009;49:407–18.

[89] Miao C, Shafrir SN, Lambropoulos JC, Mici J, Jacobs SD. Shear stress in magnetorheological finishing for glasses. Appl Opt 2009;48:2585–94.

[90] Miao C, Lambropoulos JC, Jacobs SD. Process parameter effects on material removal in magnetorheological finishing of borosilicate glass. Appl Opt 2010;49:1951–63.

[91] Singh AK, Jha S, Pandey PM. Mechanism of material removal in ball end magnetorheological finishing process. Wear 2013;302:1180–91.

[92] Schinhaerl M, Vogt C, Geiss A, Stamp R, Sperber P, Smith L, et al. Forces acting between polishing tool and workpiece surface in magnetorheological finishing. Proc. SPIE 7060, Curr. Dev. Lens Des. Opt. Eng. IX, 2008, p. 706006.

[93] Sidpara A, Jain VK. Experimental investigations into forces during magnetorheological fluid based finishing process. Int J Mach Tools Manuf 2011;51:358–62.

[94] Sidpara A, Jain VK. Theoretical analysis of forces in magnetorheological fluid based finishing process. Int J Mech Sci 2012;56:50–9.

[95] Singh AK, Jha S, Pandey PM. Magnetorheological ball end finishing process. Mater Manuf Process 2012;27:389–94.

[96] Sidpara A, Jain VK. Analysis of forces on the freeform surface in magnetorheological fluid based finishing process. Int J Mach Tools Manuf 2013;69:1–10.

[97] Geels K. Metallographic and materialographic specimen preparation, light microscopy, image analysis, and hardness testing. 15th ed. ASTM international; 2007.

[98] Ozdemir Z, Ozdemir A, Basim GB. Application of chemical mechanical polishing process on titanium based implants. Mater Sci Eng C 2016;68:383–96.

[99] Stunkard AJ. A review on the wettability of dental implant surfaces II: biological and clinical aspects. Psychiatry Interpers Biol Process 2009;162:214–20.

[100] Yuan Yuehua TRL. Contact angle and wetting properties. In: Bracco G, Holst B, editors. Springer Ser. Surf. Sci., vol. 51, 2013, p. 3–34.

[101] Ostrovska L, Vistejnova L, Dzugan J, Slama P, Kubina T, Ukraintsev E, et al. Biological evaluation of ultra-fine titanium with improved mechanical strength for dental implant engineering. J Mater Sci 2016;51:3097–110.

[102] ISO 7207-2:2011 - Implants for surgery -- Components for partial and total knee joint prostheses -- Part 2: Articulating surfaces made of metal, ceramic and plastics materials n.d.

[103] ISO B. 7206–2: Implants for Surgery—Partial and Total Hip Joint Prostheses. Part 2: Articulating Surfaces Made of Metallic, Ceramic and Plastics Materials. Br Stand Inst London, UK 2011.

[104] Le Guéhennec L, Soueidan A, Layrolle P, Amouriq Y. Surface treatments of titanium dental implants for rapid osseointegration. Dent Mater 2007;23:844–54.

[105] Rupp F, Scheideler L, Eichler M, Geis-Gerstorfer J. Wetting behavior of dental implants. Int J Oral Maxillofac Implants n.d.;26:1256–66.

[106] ISO 25178-605:2014 - Geometrical product specifications (GPS) -- Surface texture: Areal -- Part 605: Nominal characteristics of non-contact (point autofocus probe) instruments n.d.

[107] Deltombe R, Kubiak KJ, Bigerelle M. How to select the most relevant 3D roughness parameters of a surface. Scanning 2014;36:150–60.

[108] Montgomery DC. Design and analysis of experiments. 8th ed. Wiley; 1976.

[109] Derringer G, Suich R. Simultaneous optimization of several response variables. J Qual Technol 1980;12:214–9.

[110] Gregory RD. Classical mechanics. Cambridge: Cambridge University Press; 2006.

[111] Barman A, Das M. Design and fabrication of a novel polishing tool for finishing freeform surfaces in magnetic field assisted finishing (MFAF) process. Precis Eng 2017;49:61–8.

[112] Barman A, Das M. Nano-finishing of bio-titanium alloy to generate different surface morphologies by changing magnetorheological polishing fluid compositions. Precis Eng 2017. doi:10.1016/J.PRECISIONENG.2017.08.003.

[113] Barman A, Das M. Toolpath generation and finishing of bio-titanium alloy using novel polishing tool in MFAF process. Int J Adv Manuf Technol 2017:1–13.

[114] Cheung CF. Design, ultra-precision polishing and measurement of superfinished orthopaedic implants for bio-medical applications: an integrated approach. Int J Nanomanuf 2011;7:393.

[115] Silva M, Snow K. Biotribology considerations of total knee replacement. Mech Ind Eng Boston, USA 2009.

[116] Hilerio I, Barrón MA, Vite M. 3D characterization of surface state in a knee prosthesis. ASME World Tribol Congr World Tribol Congr III 2005;2:679–80.

[117] Rooks B. Robots score at grinding and polishing. Ind Robot An Int J 1998;25:251–5.

[118] Hilerio I, Mathia T, Alepee C. 3D measurements of the knee prosthesis surfaces applied in optimizing of manufacturing process. Wear 2004;257:1230–4.

[119] Charlton P, Blunt L. Surface and form metrology of polished "freeform" biological surfaces. Wear 2008;264:394–9.

[120] Kumar S, Jain VK, Sidpara A. Nanofinishing of freeform surfaces (knee joint implant) by rotational-magnetorheological abrasive flow finishing (R-MRAFF) process. Precis Eng 2015;42:165–78.

[121] Barman A, Das M. Simulation of magnetic field assisted finishing (MFAF) process Uutilizing smart MR polishing tool. J Inst Eng Ser C 2017;98:75–82.

[122] ASTM F648-14 Standard specification for ultra-high-molecular-weight polyethylene powder and fabricated form for surgical implants 2014.

[123] Kennedy FE, Van Citters DW, Wongseedakaew K, Mongkolwongrojn M. Lubrication and wear of artificial knee joint materials in a rolling/sliding tribotester. J Tribol 2007;129:326.

[124] Knee replacement implants-orthoInfo - AAOS. Am Acad Orthop Surg OrthoInfo 2016. http://orthoinfo.aaos.org/topic.cfm?topic=a00221.

[125] Malik A, Pickles C. Tribology and testing of orthopaedic implants. 2014.

[126] Malikian R, Maruthainar K, Stammers J, Cannon SR, Carrington R, Skinner JA, et al. In vivo roughening of retrieved total knee arthroplasty femoral components. Knee 2014;21:278–82.

[127] Howie DW, Haynes DR, Rogers SD, McGee MA, Pearcy MJ. The response to particulate debris. Orthop Clin North Am 1993;24:571–81.

[128] Sharkey PF, Lichstein PM, Shen C, Tokarski AT, Parvizi J. Why are total knee arthroplasties failing today—has anything changed after 10 years? J Arthroplasty 2014;29:1774–8.

[129] Klimek L, Wołowiec E, Majkowska B. Types of wear and tear of biomaterials used in orthopaedic surgery. J Achiev Mater Manuf Eng 2013;56:83–9.

[130] Dowson D, Taheri S, Wallbridge NC. The role of counterface imperfections in the wear of polyethylene. Wear 1987;119:277–93.

[131] Bowsher JG, Shelton JC. A hip simulator study of the influence of patient activity level on the wear of crosslinked polyethylene under smooth and roughened femoral conditions. Wear 2001;250:167–79.

[132] DesJardins JD, Burnikel B, LaBerge M. UHMWPE wear against roughened oxidized zirconium and CoCr femoral knee components during force-controlled simulation. Wear 2008;264:245–56.

[133] Paling IH, Schmalzried TP, Callaghan JJ. Wear in total hip and knee replacements. J Bone Jt Surg 2000;82:1804.

[134] Cooper JR, Dowson D, Fisher J. The effect of transfer film and surface roughness on the wear of lubricated ultra-high molecular weight polyethylene. Clin Mater 1993;14:295–302.

[135] Fisher J, Dowson D, Hamdzah H, Lee HL. The effect of sliding velocity on the friction and wear of UHMWPE for use in total artificial joints. Wear 1994;175:219–25.

[136] Hailey JL, Ingham E, Stone M, Wroblewski BM, Fisher J. Ultra-high molecular weight polyethylene wear debris generated in vivo and in laboratory tests; the influence of counterface roughness. Proc Inst Mech Eng Part H J Eng Med 1996;210:3–10.

[137] Lancaster JG, Dowson D, Isaac GH, Fisher J. The wear of ultra-high molecular weight polyethylene sliding on metallic and ceramic counterfaces representative of current femoral surfaces in joint replacement. Proc Inst Mech Eng Part H J Eng Med 1997;211:17–24.

[138] Walker PS, Blunn GW, Lilley PA. Wear testing of materials and surfaces for total knee replacement. J Biomed Mater Res 1996;33:159–75.

[139] ASTM G99-17 Standard Test Method for Wear Testing with a Pin-on-Disk Apparatus 17AD.

[140] Huang W, Zalnezhad E, Musharavati F, Jahanshahi P. Investigation of the tribological and biomechanical properties of CrAlTiN and CrN/NbN coatings on SST 304. Ceram Int 2017;43:7992–8003.

List of Publications

Papers published in Journals:

1. A. Barman and M. Das, “Simulation of magnetic field assisted finishing (MFAF) process utilizing smart MR polishing tool,” *J. Inst. Eng. Ser. C*, vol. 98, no. 1, pp. 75–82, 2017.
2. A. Barman and M. Das, “Design and fabrication of a novel polishing tool for finishing freeform surfaces in magnetic field assisted finishing (MFAF) process,” *Precis. Eng.*, vol. 49, pp. 61–68, 2017.
3. A. Barman and M. Das, “Toolpath generation and finishing of bio-titanium alloy using novel polishing tool in MFAF process,” *Int. J. Adv. Manuf. Technol.*, 2017, https://doi.org/10.1007/s00170-017-1050-2.
4. A. Barman and M. Das, “Soft computing techniques to model and optimize magnetic field-assisted finishing process and characterization of the finished surface,” *Proc. Inst. Mech. Eng. Part C J. Mech. Eng. Sci.*, 2017, https://doi.org/10.1177/0954406217731116.
5. A. Barman and M. Das, “Nano-finishing of bio-titanium alloy to generate different surface morphologies by changing magnetorheological polishing fluid compositions,” *Precis. Eng.*, vol. 51, pp. 145-152, 2018.
6. A. Barman and M. Das, “Simulation and experimental investigation of finishing forces in magnetic field assisted finishing process,” *Mater. Manuf. Processes*, vol. 33(11), pp. 1223–1232, 2018.

Papers communicated to Journals:

1. Anwesa Barman, Manas Das, Characterization of superfinished Ti alloy using 3D surface parameters in Magnetic Field Assisted Finishing Process**.**
2. Anwesa Barman, Manas Das, Finishing of freeform surface of femoral part of prosthetic knee joint**.**
3. Anwesa Barman, Manas Das, Performance analysis of Ti alloy finished by magnetic field assisted finishing process using pin-on-disc tribometer for femoral knee implant application**.**

Papers published in Conference Proceedings:

1. Anwesa Barman, Chandan Kumar, Manas Das, Analysis of Finishing Magnetic Field assisted Finishing (MFAF) process parameters for finishing brass workpiece using Soft-Computing Technique, Proc. of the 5th International & 26th All India Manufacturing Technology, Design and Research Conference (AIMTDR 2014) IIT Guwahati, December 12–14, 2014, pp. 45 (1-6).
2. Anwesa Barman, Manas Das, Ankur Singh, Modeling and Simulation of Magnetic Field assisted Finishing Process, Proc. of the 5th International & 26th All India Manufacturing Technology, Design and Research Conference (AIMTDR 2014) IIT Guwahati, December 12–14, 2014, pp. 48 (1-6).

3. Pritam Akhuly, Anwesa Barman, Manas Das, Heat transfer analysis of Magnetorheological fluid in Magnetic Field assisted Finishing process, International Conference on Precision, Meso, Micro and Nano-Engineering (COPEN-9), IIT Bombay, December 10-12, 2015, Paper ID 68.
4. Anwesa Barman, Manas Das, Design and Development of Novel Polishing Tool for Finishing of Freeform Surfaces in Magnetic Field assisted Finishing Process, International Conference on Precision, Meso, Micro and Nano-Engineering (COPEN-9), IIT Bombay, December 10-12, 2015, Paper ID 70.
5. Anwesa Barman, Pritam Akhuly, Manas Das, Analysis of heat generation in magnetorheological polishing medium during finishing in magnetic field assisted finishing process, 68th Annual Session of Indian Institute of Chemical Engineers (CHEMCON-2015), 27-30 December, 2015, Guwahati, India, Paper ID FM-095.
6. Anwesa Barman, Manas Das, Optimizing Toolpath Generation in Magnetic Field assisted Finishing Process during Nanofinishing of Biomaterials with a Novel Tool, Proc. of the 6th International & 27th All India Manufacturing Technology, Design and Research Conference (AIMTDR 2016) College of Engineering Pune, December 16–18, 2016.
7. Anwesa Barman, Manas Das, Analysis of forces during spot finishing of titanium alloy using novel tool in magnetic field assisted finishing process, Proc. of the 10th International Conference on Precision, Meso, Micro and Nano-Engineering (COPEN 10), IIT Madras, December 07-09, 2017.

Published book chapter:

1. Anwesa Barman, Manas Das, Hybrid finishing processes and related area, Proceedings of one day national workshop on hybrid manufacturing technology (HMT-2017), 8th March, 2017, Production engineering department, Jadavpur University, Kolkata.